Forschungszentrum Karlsruhe
Technik und Umwelt

Wissenschaftliche Berichte
FZKA 6698

Nukleare Entsorgung FuE-Aktivitäten 2001

Sammlung der Vorträge anläßlich des internen INE Mitarbeiterseminars am 12. und 19. Juli 2001

A. Loida (Hrsg.)

Institut für Nukleare Entsorgung

Februar 2002

Forschungszentrum Karlsruhe

Technik und Umwelt

Wissenschaftliche Berichte

FZKA 6698

Nukleare Entsorgung
F&E – Aktivitäten 2001

Sammlung der Vorträge anläßlich des internen
INE Mitarbeiterseminars am
12. und 19. Juli 2001

zusammengestellt von
A.Loida

Institut für Nukleare Entsorgung

Forschungszentrum Karlsruhe GmbH, Karlsruhe

2002

Forschungszentrum Karlsruhe GmbH
Postfach 3640, 76021 Karlsruhe

Mitglied der Hermann von Helmholtz-Gemeinschaft
Deutscher Forschungszentren (HGF)

ISSN 0947-8620

Vorbemerkung

Im Rahmen der internen Seminarreihe wird der jeweils aktuelle Stand der am INE durchgeführten F&E-Arbeiten vorgestellt und diskutiert. Der vorliegende Bericht beinhaltet die Ausarbeitungen der dort gehaltenen Vorträge.

Die Beiträge geben den Stand der jeweiligen F&E-Arbeiten von Juli 2001 wieder. Nicht in jedem Fall können die Beiträge als abgeschlossen und vollständig ausgewertet angesehen werden.

Note

In the frame of the internal seminar of the INE the actual state of the running R&D projects of the institute is being presented and discussed. This report contains summaries of the presentations, which were given on this occasion, and the intention is to make it available for the public.

Each contribution reflects the state of the related R&D project from July 2001 and does not represent necessarily a completed work.

Inhaltsverzeichnis

Numerical Analysis of Long–Term Thermomechanical Behavior of Repository Structures

Alexandra Pudewills

ABSTRACT

This paper summarizes the current state of knowledge concerning the numerical simulation of the thermomechanical effects in the near field of a conceptual repository for disposal of highly radioactive burnt-out spent fuel. The work includes, in particular, the modeling of the temperature fields, thermally induced closure of the underground openings followed by the consolidation of the backfill, and the resulting stresses in the surrounding salt formation. To perform this task, finite element codes containing a set of time- and temperature-dependent constitutive models are used. In a first step the validation of the numerical models and the constitutive equations available for rock salt and backfill material were demonstrated by comparison of calculated results and measured data of a large-scale in situ test. On the basis of these results, the predictive calculations for an emplacement drift in the planned waste repository were performed. The results of the analyses show that under expected repository conditions the volume closure and, hence, the compaction of the backfill are mainly determined by the temperature increase and the lithostatic pressure. Finally, the implications for the post-closure safety evolution are discussed.

INTRODUCTION

Repository concepts for disposal of high-level radioactive waste from reprocessing and spent-fuel assemblies are based on multiple barriers for protection of the environment against the radioactive nuclides. According to these concepts, the containers with heat generating radioactive waste will be placed in vertical boreholes or long parallel drifts at a depth of about 800 to 1000 m below the surface in a rock salt formation [1], [2]. The remaining void space between the containers and host rock will be filled with dry crushed salt. It is expected that in response to the thermally induced creep closure of the excavations the backfill material will compact sufficiently to serve as an efficient seal for the radioactive waste. The performance assessment of such nuclear waste repositories in rock salt requires laboratory tests, field experiments, and the use of adequate numerical models to predict the long-term thermomechanical effects in the near and far fields of the repository. The numerical reliability of the calculations and the predictive capabilities were demonstrated in international benchmark activities and also by comparison with results of the *in situ* heater tests [3].

The scope of this paper is to give an overview of the actual repository concepts focusing on long-term thermomechanical phenomena related to the emplacement of heat-generating waste. This includes numerical modeling of the temperature fields, thermally induced closure of the openings following by the consolidation of the backfill, and the resulting stresses in the surrounding salt. With regard to the behavior of backfill material, the reduction of the porosity and the increase of the pressure on the waste containers were estimated.

The FAST-BEST code, based on the coarse mesh method [4], [5] and specifically developed for studying the drift disposal, was used to predict the temperatures. This program includes temperature-dependent material models for rock salt and crushed salt. The material model for crushed salt takes into account a compaction-dependent thermal conductivity. For

the thermomechanical analyses, two finite element codes have been used. One is the general-purpose code ADINA [6] which was extended to investigate the creep compaction of a loose backfill material [7], and the other one is the special-purpose code MAUS [8] which also includes suitable material models for rock salt and crushed salt.

As an illustration of the capability of these codes of solving such complex problems and as a validation of the assumed material models, the numerical simulation of the large-scale *in situ* test TSDE, (**T**hermal **S**imulation of **D**rift **E**mplacement) performed in the Asse salt mine [9], [10] will be used as an example.

Based on the experience gained from the evaluation of this *in situ* test, predictive calculations were carried out for an emplacement drift in the planned repository. The results of the analyses show that under expected repository conditions the volume closure and the compaction of the backfill are mainly determined by the temperature increase and the lithostatic pressure. The porosity of the backfill material will be reduced considerably after few years. With time, the compaction pressure in the backfill increases and therefore supports substantially the rock salt around the drift, and a relevant relaxation and redistribution of stresses in the pillar takes place.

THERMOMECHANICAL ANALYSIS OF A LARGE SCALE IN SITU TEST

The in situ experiment TSDE was performed in the Asse salt mine in Germany in order to demonstrate the emplacement technology and to study the thermal and thermomechanical consequences of the direct disposal of spent nuclear fuel in drifts on the rock mass and technical barriers. A further aim was to evaluate the capability of the available codes to simulate the thermomechanical behavior of the backfill and rock salt under representative repository conditions [4]. The test field is located in a rock salt formation at 800 m depth below the surface. Two parallel drifts were excavated with a length of about 75 m. In each test drift three electrically heated casks with a thermal power of about 6.5 kW were emplaced horizontally on the floor (Figure 1). After installation of the heaters and measuring equipment, the test drifts were filled with dry crushed salt. Heating was started in September 1990 and ended in February 1999.

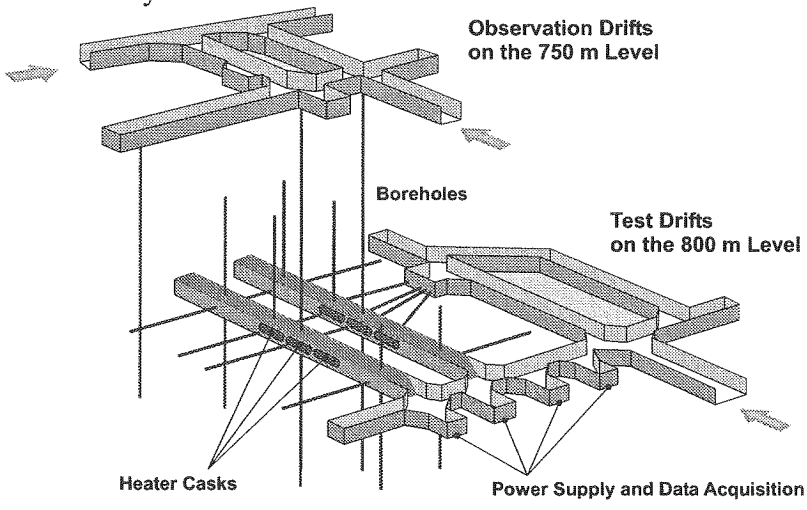

Fig. 1: General view of the TSDE test field [4]

Within the framework of the European project "**BA**ckfill and **M**aterial **B**ehaviour in **U**nderground **S**alt Repositories" (BAMBUS) [3], the development of the temperature in the test field, the thermally induced closure of the drifts followed by the compaction of the

backfill, and the resulting stresses in the surrounding salt were studied numerically. Sensitivity studies served to investigate how the assumed material models of crushed salt and rock salt affected the numerical results. The predictive calculations and the comparison with in situ data are raportated in detail in References [11],[12]. Representative results from the numerical simulations only are shown in this paper.

According to the real geometry of the experiment, a three-dimensional finite element model for temperature calculations wes used. A detailed description of this numerical model with the assumed boundary and initial conditions is given in also in Ref. [11] The temperature histories measured and modeled at three characteristic positions through the central cross-section of the test field are shown in Figure 2. The data nearly agree with the calculated temperatures, thus providing confidence in the three-dimensional model used.

To perform the thermomechanical analyses with a reasonable numerical effort, a two-dimensional finite element model was used, assuming generalized plane strain conditions. The model represents a vertical cross-section perpendicular to the drifts at three measuring cross-sections; Two sections located in the zone of maximum temperatures and a section situated in the cooler region. The development of horizontal and vertical drift closure rates measured and calculated for the two cross-sections considered is illustrated in Figure 3.

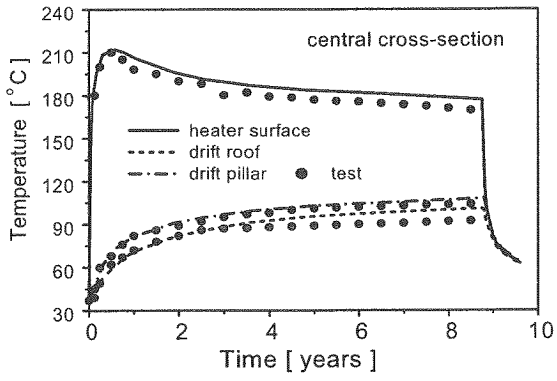

Fig. 2: Comparison of calculated and measured temperatures in the hot cross-section

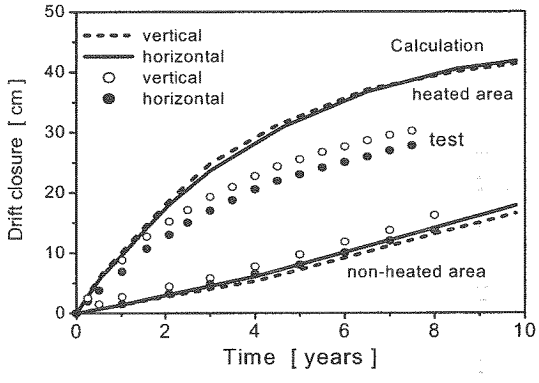

Fig. 3: Drift closure, experimental data and calculation results of two cross-sections

In the heated region the calculation results show an overestimation of the test data. A typical deformed configuration of the backfilled drift is shown in Figure 4. The development of the backfill porosity was not directly measured in the experiment. Generally, the same tendency as for the drift closure presented above can be expected i.e. the porosity reduction will be overestimated by the models used. Due to the temperature-dependent compaction of the backfill and large temperature gradients in the drift, a non-uniform distribution of the backfill porosity over the drift cross- section is expected. Contour plots of calculated porosity distribution in the drift should support this presumption. Figure 5 shows the spatial distribution of the porosity in the drift after 8 years of heating. In the planned post-test project an extensive sampling program with laboratory investigations will be performed to elucidate this presumption.

Finally, the thermomechanical results based on the constitutive equations described in Ref. [13] lead to some differences between the calculated results and the measurements. The discrepancy could be attributed to uncertainties in the material model of the backfill. Therefore, material parameters obtained from laboratory tests have been adjusted in a parametric study, where the measured and calculated drift closure rates and backfill compaction pressure are matched. Further numerical results of thermomechanical sensitivity

analyses [13], [14] suggest that the present deviatoric constitutive model of crushed salt behaves more softly than the crushed salt used in the TSDE experiment. The possible reason for this effect could be a separation of loose salt grains with different sizes during the backfilling process, causing an inhomogeneous distribution over the drift cross-section.

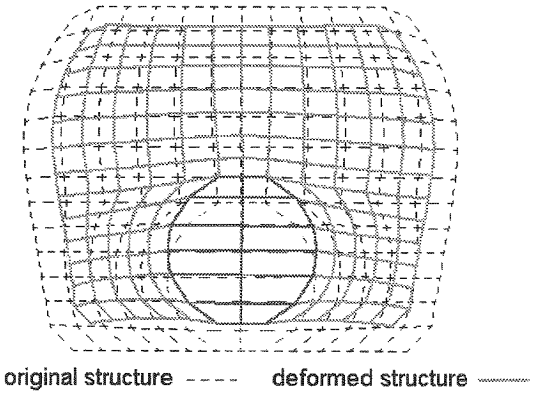

Fig. 5: Deformation of the drift after 8 years of heating in the central cross-section

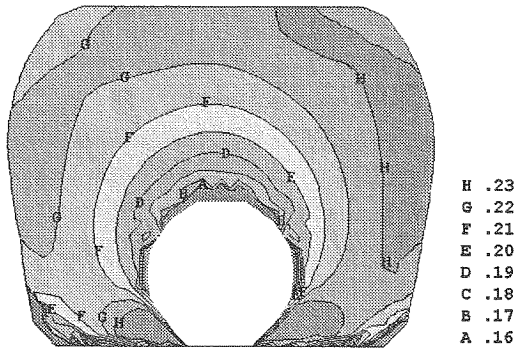

Fig. 6: Distribution of the porosity after 8 years of heating in the central cross-section

THERMOMECHANICAL CALCULATIONS FOR A DISPOSAL DRIFT

Taking into account the periodic pattern and symmetry of the disposal field, it was also assumed that all disposal drifts in the emplacement panel were excavated and filled with POLLUX casks and crushed salt instantaneously at time zero. A three-dimensional model of a representative portion of the disposal drift were defined for the thermal analysis. In further two-dimensional thermomechanical calculations the temperatures are interpolated from a vertical section passing through the center of the model geometry. A plane strain finite element model was chosen for this thermomechanical investigation. The vertical section right through the center of a POLLUX cask represents only one half of the disposal drift and of the pillar between adjacent drifts.

The numerical simulation started with the calculation of the isothermal convergence and the stress distribution around the disposal drift prior to the emplacement of the POLLUX casks. After about 0.7 years, the temperature development and the of backfill material in the drift were taken into account. The thermomechanical analyses were continued over a period of 50 years. After emplacement of the casks and backfill of the disposal drift, the volume closure and, hence, the compaction of the backfill material are mainly determined by the temperature development and the thermomechanical behavior of the crushed salt.

For a reference case with a pillar width of 12.5 m the histories of the calculated temperatures at three characteristic points are shown in Figure 6. The development of stresses in the backfill material and the decrease of the backfill porosity at two positions in the drift are shown in Figures 7 and 8. Over time, the compaction pressure in the crushed salt increases and becomes large enough to support substantially the rock salt around the drift. These results show that in a repository at a depth of about 870 m the creep rates of rock salt and closure rates will be significantly higher than in the TSDE situ test drifts and that the backfill will be compacted to a porosity of about 1% after ten years of heating.

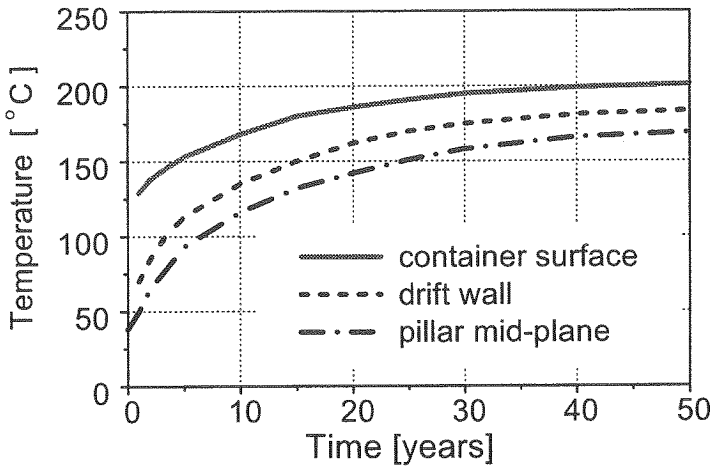

Fig. 6: Calculated temperature histories at different positions

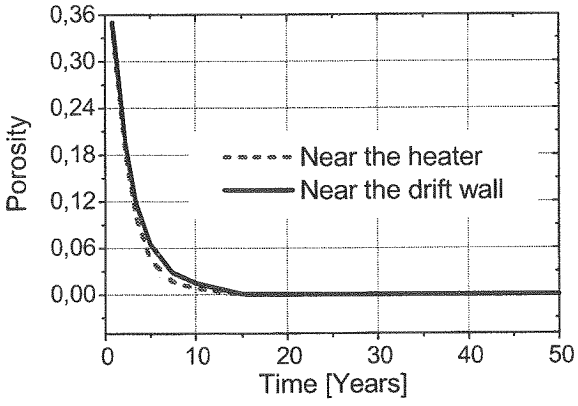

Fig. 7: Development of the backfill porosity

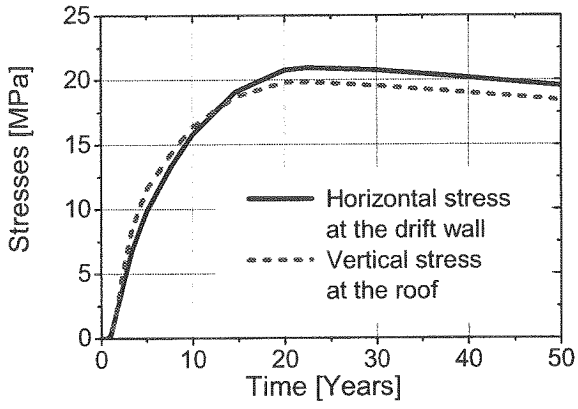

Fig. 8: Development of stresses into the backfill

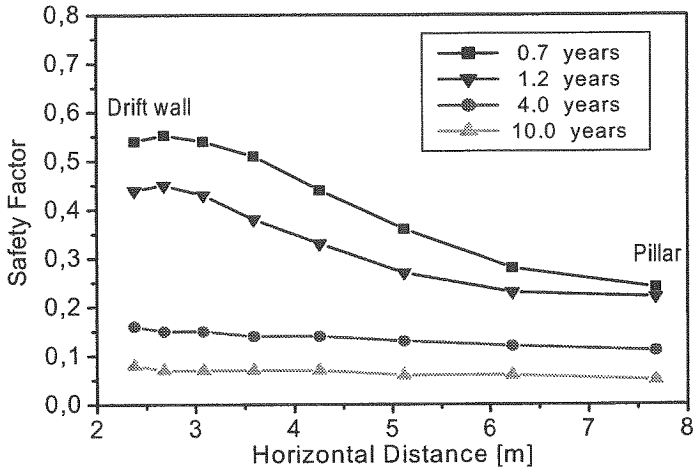

Fig. 9: Distribution of Safety Factor in the pillar at different times

The region in the pillar next to the drift shows highest shear stress during the operational phase. With time, the compaction pressure in the backfill increases and therefore supports the rock salt around the drift, and a relaxation and redistribution of the stresses in the pillar takes place during the first 10 years after the emplacement of the casks. Figure 9 shows the distribution of the Safety Factor (ratio between the calculated shear stress and the assumed fracture criterion) in the pillar for different times.

CONCLUSIONS

The agreement between the results of the calculations and the in situ measured values shown that a relatively good prediction can be made of the thermomechanical effects in the near field of the TSDE test with the numerical methods and the material laws used.

Based on these results, the numerical simulation of an emplacement drift in the planned waste repository were performed. Due to thermally induced drift closure, the crushed salt in the drift compacts sufficiently to support the surrounding rock salt and will serve as a seal for the waste casks. Furthermore, the calculations show that in a repository planned at a depth between 870 and 1170 m the rates of rock-salt creep and room closure will be much higher than in the TSDE test drifts and that the backfill will be compacted to a porosity of about 1% after ten years of heating.

High shear stresses result in the vicinity of the drift during the mining phase. However, the ratio of actual shear stress to the assumed failure criterion remains less than unity (i.e. no cracks are expected). The results related to the long-term behavior of the disposal drift show that after a few years already, the compaction pressure in the backfill increase rapidly and tends to become hydrostatic, i.e. the effective stress declines and tends slowly towards zero, which means that the surrounding rock salt is relieved.

REFERENCES

1. Bechthold, W., Braun, W., Brückner, C., Closs, D., Knapp, U., Papp, R., "Systemanalyse Mischkonzept", Hauptband, KWA-2190 A1, Kernforschungszentrum Karlsruhe GmbH, 1989.
2. Bechthold, W., Closs, K.D., Knapp, U., Papp, R., "System analysis for a dual-purpose repository", Final Report, EUR 14595 EN,Brussels, 1993.
3. Bechthold, W., Rothfuchs, T., Poley, A., Ghoreychi, M., Heusermann, S., Gens, A., Olivella, S., "Backfill and Material Behaviour in Underground Repositories for Radioactive Waste in Salt (BAMBUS Project)", Final Report, EUR-19124 EN, Brussels, 1999.
4. Ploumen, P., Strickmann, G., Winske, P., "Untersuchungen zur Temperaturentwicklung bei der Endlagerung hochradioaktiver Abfälle", Teil I: Berechnung der zeit- und ortsabhängigen Temperaturfelder, ATW, No.2, pp. 85-91, Feb.1979.
5. Korthaus, E., "Abschließende Verbesserung der vorliegenden Rechenprogramme zur Bestimmung der Temperaturentwicklung", Abschlußbericht 1980-1982, Vertrag Nr.266-80-7-WASD, EUR 8667 DE, 1983.
6. ADINA, Automatic Dynamic Incremental Nonlinear Analysis, Watertown, MA, ADINA R&D, 1999.
7. Pudewills, A., Krauss, M., "Implementation of a viscoplastic model for crushed salt in the ADINA program", Computers and Structures, vol. 72, pp. 293-99, 1999.

8. Albers, G., (1983), "MAUS - A Computer Code for Modelling Thermomechanical Stresses in Rock Salt," Computer Modelling of Stresses in Rock, Proc. Tech. Session, EUR9355 EN, Brussels.
9. Bechthold, W., Heusermann, S., Schrimpf, C., Gommlich, G., "Large scale test on in-situ backfill properties and behavior under reference repository conditions", NEA/CEC Workshop on Sealing of Radioactive Waste Repositories, Braunschweig, Germany, May 22-25, 1989.
10. Droste, J., Feddersen, K. H., Rothfuchs, T., Zimmer, U., "The TSS-Project: Simulation of Drift Emplacement", Final Report Phase 2, 1993-1995, GRS-127, Gesellschaft für Anlagen- und Reaktorsicherheit mbH, Braunschweig, 1996.
11. Pudewills, A., "Thermal Simulation of Drift Emplacement: Temperature Analyses", Topical Report, FZKA 5955, Forschungszentrum Karlsruhe, 1997.
12. Pudewills, A., "Thermomechanical analysis of the TSS experiment", Proc. Inter. Congr. Underground Construction in Modern Infrastructure', Stockholm, S, June 7-9, 1998, Rotterdam: Balkema, pp.317-323, 1998.
13. Korthaus, E., "Consolidation behaviour of dry crushed salt: Triaxial tests, benchmark exercise and in situ validation", Proc. of 5th Conf. on the Mech. Behavior of Salt, Bucharest, Ro., August 9-14, 1999, (in print).
14. Pudewills, A., Rothfuchs, T.," Thermomechanical Analyses for the TSS-Experiment and Comparison with In Situ Measurements". The Mech. Behavior of Salt : Proc. of the 5th Conf., Bucharest, Ro., August 9-14, 1999, (in print).

Modellrechnungen zu Umlösevorgängen im Endlagernahbereich

E. Korthaus

Einleitung

Bei Laugenbewegungen durch Einlagerungsörter, Verschlüsse und andere Wegsamkeiten im Nahbereich eines Endlagers im Salz treten Salzumlösungen aufgrund von Temperaturgradienten und unterschiedlicher Zusammensetzung des anstehenden Salzes auf. Dies kann zu signifikanten Änderungen der Durchlässigkeit der durchströmten Wegsamkeiten führen sowie zu Veränderungen der lokalen Laugenzusammensetzungen, die für geochemische Reaktionen und Gleichgewichte von Bedeutung sind. Dies gilt auch für die unmittelbare Umgebung von Endlagergebinden im Zusammenhang mit der Behälterkorrosion. Hier können diese Effekte massgebend für die erreichbaren Behälterstandzeiten sein.

Im Rahmen der Entwicklung und Bewertung von Störfallszenarien müssen Modellrechnungen zu diesen Vorgängen durchgeführt werden, die eine Extrapolation der Ergebnisse von Labormessungen oder in-situ Experimenten auf Endlagerbedingungen und lange Zeiträume ermöglichen. Zu diesem Zweck wird ein Rechenprogramm entwickelt, das die in diesem Zusammenhang relevanten gekoppelten Effekte in geeigneter Näherung beschreiben soll. Bisher verfügbare gekoppelte Programme erfassen nur Teilaspekte dieser Problematik und/oder sind nicht für die Behandlung hochkonzentrierter Salzlaugen geeignet.

Entwicklung des Programms TRANSAL

Das 1-dimensionale Programm TRANSAL (Transport im Salz) basiert auf der Kopplung eines Codes für den advektiven und dispersiven Stofftransport, eines thermodynamischen Speziations-Codes (basierend auf Teilen des gekoppelten Codes THCC /1/) mit Pitzer-Formalismus zur Berücksichtigung hoher Salzkonzentrationen, sowie einem Strömungs-Code für die Berechnung der Strömung durch poröse Wegsamkeiten unter Berücksichtigung von thermomechanischen Konvergenzeffekten. Letztere stehen in enger Wechselwirkung mit den hydraulischen Verhältnissen, da einerseits die Konvergenz die Porosität und andererseits der Fluiddruck die Konvergenzrate massgeblich beeinflussen.

TRANSAL ist ein iterativ gekoppelter Code. Die Iteration zwischen Stofftransport und thermodynamischer Gleichgewichtsberechnung wird dabei auch für eine Erweiterung zur Berücksichtigung kinetischer Effekte herangezogen (s.u.).

Speziell im Hinblick auf hohe Salzkonzentrationen und die mögliche Ausfällung oder Auflösung von Hydratsalzen wurde die Berücksichtigung der Wasserbilanz ermöglicht. Gewisse Konvergenzprobleme der thermodynamischen Gleichgewichtsrechnung bei hohen Ionenstärken werden durch eine implizite Berücksichtigung der Konzentrationsabhängigkeit der Aktivitätskoeffizienten innerhalb der Newton-Iteration zur Lösung des nichtlinearen Gleichungssystems überwunden.

Eine erste Version des Programms wurde bereits anhand von Beispielrechnungen zu hypothetischen Laugenströmungen bei der Bohrlochlagerung von hochaktiven Abfällen getestet. Da z.Zt. noch keine realistischen, auf einen Endlagerstandort bezogenen Randbedingungen für derartige Rechnungen verfügbar sind, wurden diese Untersuchungen zunächst nicht weitergeführt. Stattdessen wurde die Weiterentwicklung des Programms für die

Modellierung der Verhältnisse bei der Korrosion von Behältern aus unlegiertem Stahl in einer Umgebung von laugengetränktem Versatzmaterial in Angriff genommen.

Zunächst wurde das Programm für die Berücksichtigung aquatischer Komplexe ausgebaut, um auch Hydrolyse- und Redoxreaktionen sowie gelöste Gase berücksichtigen zu können. Als aquatische Spezies sind inzwischen Na^+, K^+, Mg^{++}, Ca^{++}, Fe^{++}, Fe^{3+}, H^+, Cl^-, SO_4^{--}, OH^-, $MgOH^+$, $MgSO_4(aq)$, $Fe(OH)_2^+$, $Fe(OH)_2(aq)$, $Fe(OH)_3(aq)$, $FeSO_4(aq)$, $O_2(aq)$ und H_2O in der Datenbasis für Testrechnungen enthalten.

Da Redoxreaktionen relativ langsam ablaufen und daher bei den grossen Konzentrationsgradienten in der Umgebung von Korrosionsflächen die Annahme eines thermodynamischen Gleichgewichts nicht gerechtfertigt ist, wurde die zusätzliche Berücksichtigung kinetischer Hemmungen erforderlich. Hierzu wurde ein Konzept gewählt, bei dem die Gleichgewichtskonstante K* der betreffenden Reaktion während eines jeden Rechenzeitschritts so bestimmt wird, dass sich die Reaktionsrate entsprechend der vorgegebenen Reaktionskinetik ergibt. Dies erfolgt durch ein Prädiktor-Korrektorverfahren im Rahmen der iterativen Kopplung des Programms.

Für den hier interessierenden Fall der Oxidation von Fe^{++} durch Sauerstoff zu Fe^{3+} wurde dies zunächst (in Analogie zu den für schwach alkalische Grundwässer in /2/ angegebenen Verhältnissen) folgendermassen angesetzt:

Vorgegebene Oxidationsrate $$d/dt[Fe^{++}] = - k\,[O_2(aq)] / [H^+]^2\,([Fe^{++}] - c_0) \qquad (1)$$

mit der Gleichgewichtskonzentration c_0 von Fe^{++}, die sich aus den Redoxgleichgewichten des Wassers und des Eisens ergibt:

$$c_0 = K/\gamma_{Fe++}\,\{H_2O\}^{0.5}\,\{Fe^{3+}\} / \{H^+\} / \{O_2(aq)\}^{0.25} \qquad (2)$$

Hierbei bedeuten die eckigen und geschweiften Klammern Konzentrationen und Aktivitäten, k eine Geschwindigkeits- und K eine Gleichgewichtskonstante, und γ_{Fe++} der Aktivitätskoeffizient von Fe^{++}.

In der thermodynamischen Gleichgewichtsrechnung wird der Sauerstoff als aquatischer Komplex behandelt, der über die (der Glg.(2) entsprechende) Beziehung

$$\{O_2(aq)\} = K\,\{H_2O\}^2\,\{Fe^{3+}\}^4 / \{H^+\}^4 / \{Fe^{++}\}^4 \qquad (3)$$

mit dem Redoxverhältnis des Eisens verknüpft ist. Indem nun K durch die variable Grösse K* ersetzt wird, so lässt sich die gewünschte Oxidationsrate zeitschrittweise einstellen. Für die iterative Anpassung von K*, d.h. für die Bestimmung eines Korrektors δK^* zu einem Schätzwert von K*, wird die Beziehung

$$\delta K^* = K^*\,(\,\delta[O_2(aq)] / [O_2(aq)] + 4\,\delta[Fe^{++}] / [Fe^{++}] + 4\,\delta[H^+] / [H^+] - 4\,\delta[Fe^{3+}] / [Fe^{3+}] - 2\,\delta[H_2O] / [H_2O]\,) \qquad (4)$$

herangezogen, die man durch Differentiation von Glg. (3) erhält. Die verschiedenen Terme der rechten Seite werden entsprechend der gewünschten Änderung der Oxidationsrate bestimmt. Sie hängen teilweise vom pH und der Anwesenheit fester Phasen des Eisens ab.

Die Tatsache, dass die vorgegebene Oxidationsrate nach Glg.(1) von den Konzentrationen von O_2 und H^+ abhängt (Kinetik höherer Ordnung) und sich daher ebenfalls bei jedem Zeitschritt ändert, wirkt sich erschwerend auf die Konvergenz der Iteration aus. Durch die Wahl einer relativ langsamen iterativen Korrektur von R wurde jedoch ein stabiles Verfahren erreicht, das auch die kritischen Situationen bei beginnender Ausfällung oder Auflösung fester Phasen gut beherrscht.

Die automatische Zeitschrittsteuerung erfolgt im wesentlichen über vorgegebene maximale Änderungen der Konzentrationen der gelösten Komponenten pro Zeitschritt. Zusätzlich wird die Änderung der Gleichgewichtskostanten K* begrenzt. Die Iterationsgenauigkeit wird über die Variation der Konzentrationen der Komponenten kontrolliert sowie über die Abweichung der Oxidationsrate von Fe^{++} gegenüber der Vorgabe nach Glg.(1).

Ein Problem im Falle von Rechnungen zur Eisenoxidation unter Sauerstoffverbrauch besteht darin, dass im Laufe der Zeit lokal extrem geringe Sauerstoffkonzentrationen auftreten, deren weitere Beschreibung mit einem unerträglichen Rechenzeitaufwand verbunden ist. Eine praktikable Lösung zu diesem Problem besteht darin, die Sauerstoffkonzentration bei Erreichen eines Wertes, der so niedrig ist, dass das weitere Absinken keinen nennenswerten Einfluss auf die Ergebnisse hat, festzuhalten. Dies ist bei derartigen gekoppelten Rechnungen nicht trivial. Es wurde hier durch die Einführung einer verschieblichen Randbedingung für O_2(aq) im Rahmen der Transportrechnung unter Berücksichtigung des über den Rand tretenden Diffusionsstromes bei der chemischen Bilanzierung gelöst. Ein anderes Verfahren über die geregelte Reduktion der Oxidationsrate erwies sich als nicht praktikabel, da hier Oszillationen auftraten, die kleine Zeitschritte erzwangen und damit den Rechenfortschritt behinderten.

Testbeispiel

In Testrechnungen wurde bisher der Fall einer Flüssigkeitssäule (Länge 0.5 m, gesättigte NaCl-Lösung, 25°C) betrachtet mit einer Fe^{++} und OH^- Einspeisung konstanter Rate (10^{-8} bzw. $2 \cdot 10^{-8}$ mol/m^2/s) an einem Rand zur Simulation einer korrodierenden Oberfläche aus unlegiertem Stahl.

Als Anfangsbedingung wurden pH7 sowie oxidierende Verhältnisse mit 3.10^{-5} mol/l an gelöstem Sauerstoff angenommen (Eh = 0.8 V).

Bei Anwesenheit von gelöstem Sauerstoff wird der bei der Korrosion entstehende Wasserstoff sofort zu Wasser oxidiert. Der dadurch verursachte Sauerstoffverbrauch wurde durch eine entsprechende O_2-Senke berücksichtigt, die bei verschwindender Sauerstoffkonzentration abgeschaltet wurde.

Als Transportmechanismus wurde Diffusion vorausgesetzt. Als Diffusionskonstante wurde für alle gelösten Spezies einheitlich $2 \cdot 10^{-10}$ m^2/s verwendet.

Für die Geschwindigkeitskonstante k der Oxidation des Fe^{++} durch O_2 wurde nach /2/ der Wert $5. 10^{-14}$ mol/s gewählt.

Für diesen Fall wurden die in den Abb. 1 – 4 für 3 Zeitpunkte gezeigten Ortsverteilungen der wesentlichsten gelösten Eisenspezies sowie des Sauerstoffs und des pH-Wertes berechnet. Das dem Verhältnis Fe^{3+}/ Fe^{++} entsprechende Redoxpotential Eh ist in Abb.5 gezeigt.

Die Verteilung von ausgefallenem Magnetit Fe_3O_4 und Hämatit Fe_2O_3 in der Umgebung der 'Korrosionsfläche' zeigen die Abb. 6 - 7 . Direkt vor der 'Korrosionsfläche', d.h. im ersten Intervall von 0.01 mm Breite, fällt $Fe(OH)_2$ aus, und zwar in wesentlich grösserer Menge (Faktor 40 nach 100 d). Dazu ist anzumerken, dass in der Realität anstelle von Fe_3O_4 und Fe_2O_3 zunächst meist andere Festphasen wie $Fe(OH)_2$, FeOOH (z.B. als Goethit, α-FeOOH), und $FeHO_8(H_2O)_4$ (Ferrihydrit) ausfallen, die zwar thermodynamisch weniger stabil sind als die Oxide, deren Bildung jedoch kinetisch weniger gehemmt ist. Für eine realistischere Beschreibung dieser Abläufe sind wesentliche Erweiterungen der Modellierung hinsichtlich der Kinetik der Festphasenbildung erforderlich. Die hier angesprochenen Vorgänge sind zu unterscheiden von der Bildung von festen (elektrisch leitenden) Deckschichten direkt auf der Korrosionsfläche aufgrund der dort ablaufenden elektrochemischen Reaktionen .

Die gezeigten Ergebnisse sind aus den genannten Gründen und wegen anderer Mängel der verwendeten Datenbasis quantitativ nicht belastbar. Sie zeigen jedoch exemplarisch die bei der Eisenkorrosion unter gewissen Bedingungen zu erwartenden Orts- und Zeitabhängigkeiten der relevanten gelösten Spezies und von festen Korrosionsprodukten im Korrosionsmedium bzw. im Porenraum des anliegenden Versatzmaterials. Insbesondere wird deutlich, dass sich das chemische Milieu hinsichtlich pH-Wert und Redoxeigenschaften in unmittelbarer Nähe der Korrosionsfläche durch die ablaufenden Prozesse stark verändern kann.

Die Ergebnisse zeigen ausserdem, dass sich mit dem Programm TRANSAL die bei derartigen Fällen auftretenden schwierigen numerischen Verhältnisse prinzipiell beherrschen lassen. Diese zeichnen sich durch grosse zeitlich veränderliche Konzentrationsgradienten aus sowie durch Konzentrationen der einzelnen Spezies, die sich teilweise um viele Grössenordnungen unterscheiden.

Als nächster Schritt der Programmentwicklung sollen nun elektrochemische Formeln zur Modellierung des eigentlichen Korrosionsvorgangs in Abhängigkeit vom lokalen chemischen Milieu implementiert werden. Damit wird u.a. auch der Einfluss der Porosität des an der Korrosionsfläche anliegenden Versatzmaterials untersucht werden können.

Literatur

/1/ Carnahan, C.L., 1987. Simulation of Uranium Transport with Variable Temperature and Oxidation Potential: The Computer Program THCC. Mat. Res. Soc. Symp. Proc., 84 : 713-721.

/2/ L. Sigg, W. Stumm. Aquatische Chemie, ISBN 3-7281-1766-8, Verlag der Fachvereine, Zürich, ISBN 3-519-1365-1, B.G. Teubner Verlag, Stuttgart, 1991.

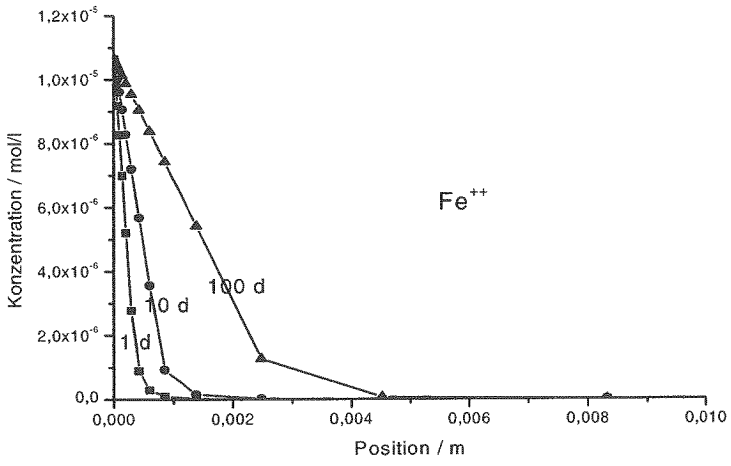

Abb. 1 Zeitliche Entwicklung der Ortsverteilung der Fe^{++}-Konzentration (Abszisse: Abstand von der "Korrosionsfläche").

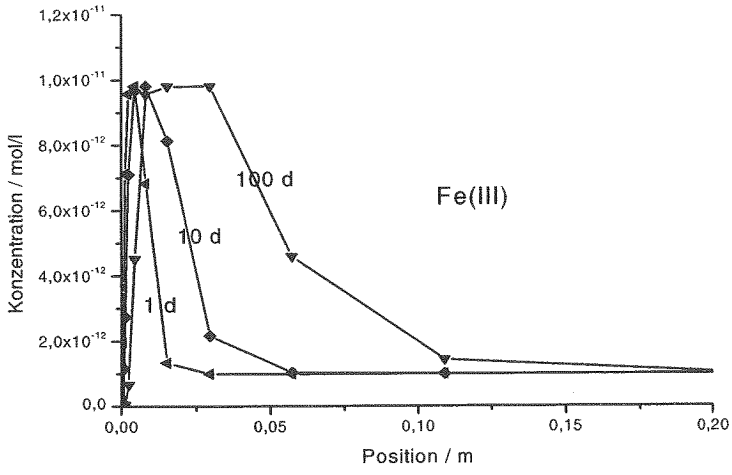

Abb. 2 Zeitliche Entwicklung der Ortsverteilung der Fe(III)-Konzentration ($Fe(OH)_2^+$, $Fe(OH)_3(aq)$)

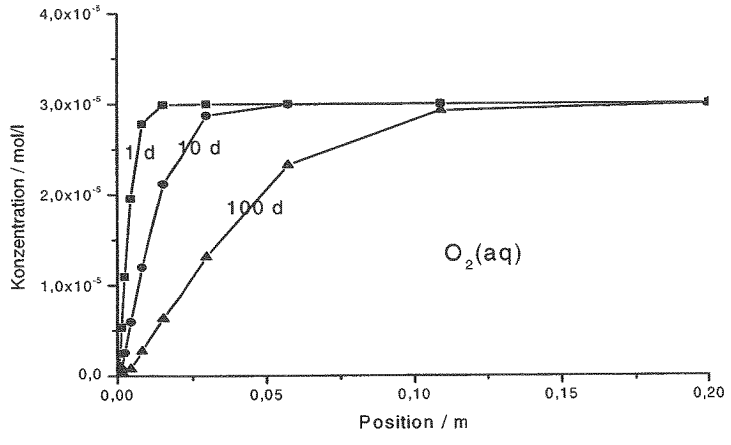

Abb. 3 Zeitliche Entwicklung der Ortsverteilung des gelösten Sauerstoffs

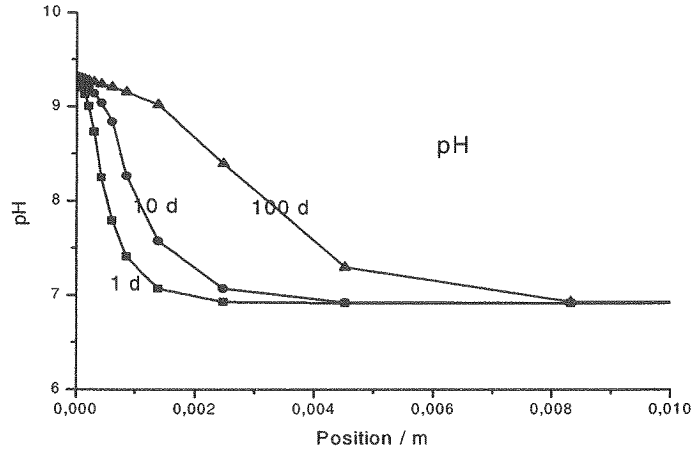

Abb. 4 Zeitliche Entwicklung der Ortsabhängigkeit des pH-Werts

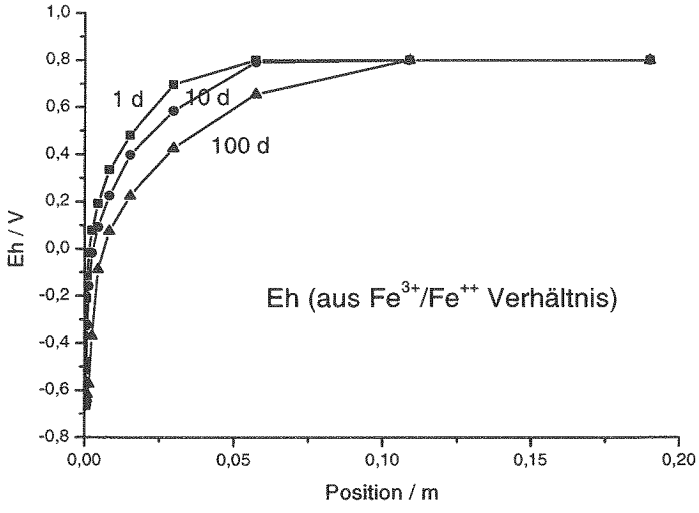

Abb. 5 Zeitliche Entwicklung der Ortsabhängigkeit des Redoxpotentials

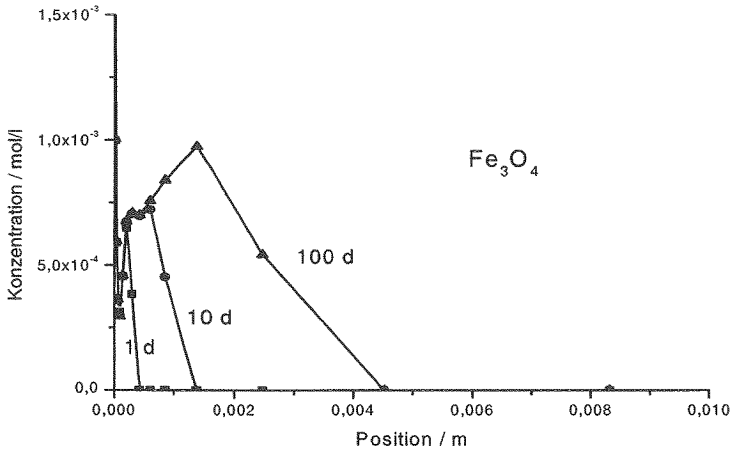

Abb. 6 Zeitliche Entwicklung der Ortsverteilung des ausgefallenen Fe_3O_4

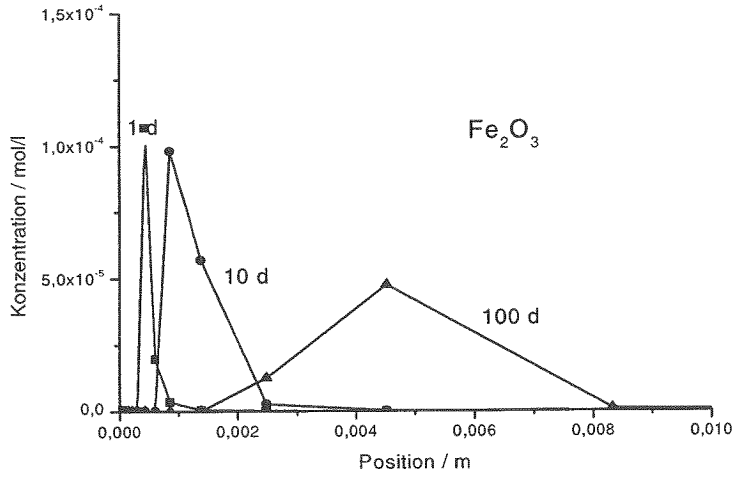

Abb. 7 Zeitliche Entwicklung der Ortsverteilung des ausgefallenen Fe_2O_3

EFFECT OF CANISTER FILLING BY MULTIPLE POURING BATCHES ON QUALITY PROPERTIES OF HLW GLASS PRODUCT

*G. Roth, S. Weisenburger, W. Grünewald, Y. Gauthier**
Forschungszentrum Karlsruhe, Institut für Nukleare Entsorgung
*Bereich Stilllegung Nuklearer Anlagen
Postfach 3640, 76021 Karlsruhe, Germany

ABSTRACT

About 70 m^3 of highly active liquid waste generated by the former German WAK (Wiederaufarbeitungsanlage Karlsruhe) reprocessing plant will be conditioned in a new vitrification facility of Forschungszentrum Karlsruhe (FZK). The use of s small-scale liquid-fed ceramic melter necessitates the filling of the glass canisters by four separate pourings. The effect of the multiple batches on relevant properties of the glass product was investigated within the operation of an inactive prototype test facility. The paper describes results from the investigation of glass samples taken from the interfaces between the batches from a cut canister and from non-destructive canister examination using computer tomography.

INTRODUCTION

One major project within the decommissioning program of the former German pilot reprocessing plant WAK (Wiederaufarbeitungsanlage Karlsruhe) deals with the vitrification of about 70 m^3 of highly active liquid waste (HLW) stored on site. The waste solution with a gross activity of 7.7E17 Bq (24 Mio. Ci) had been generated during twenty years of reprocessing operation terminated in 1990.

The conditioning of this HLW will be carried out in a new vitrification facility designated VEK (Verglasungseinrichtung Karlsruhe) being under construction since 1999 by Forschungszentrum Karlsruhe (FZK) [1]. Due to the limited use to only condition the stored HLW, VEK has been designed as a compact-size vitrification plant with an HLW design throughput capacity of 10-12 l/h. The technology to be applied in that plant is based on a liquid-fed refractory-lined glass melter, provided by the Institut für Nukleare Entsorgung (INE) of FZK.

Licensing of VEK comprehends two independent procedures: licensing of the plant and of the waste glass product. Licensing of the waste glass includes the prove that the process is suitable to generate a waste glass that meets specified ranges of a set of defined parameters relevant for final disposal. Among others there are the waste glass loading, the leach resistance and the control of surface enlargement mainly generated by thermal stresses while cooling.

PROBLEM DESCRIPTION

Fig. 1 contains a perspective cut view of the small-sized melter with a corresponding small melt tank capacity. It is a noble metals-compatible melter design equipped with a bottom pouring system. The outside diameter of the cylindrical-shaped melter is 1.5 m and its height is 1.7 m. The melt tank capacity is about 420 kg of glass melt, which is nearly equal to the content of the used canister type (European standard). One of the essential advantages of this limited inventory is the possibility to empty the melter completely into one canister in case of need. In turn, the small capacity allows maximum glass pouring batches of 100 kg. As a consequence, the complete filling of a canister requires four pouring batches. Pouring frequency depending on the feed rate is approximately every 15-20 hours. As the concept does not include additional heating of the canister while being in the pouring position the question arises whether and to what extent the multiple pouring procedure does influence glass properties. To form a monolithic glass product the heat transfer from the following batch must be high enough to remelt the cooled near-surface part of the foregoing one. Deterioration of the glass quality might be anticipated in the range of the interfaces between the respective batches. There the glass first cools down slowly and is heated up again fast by the subsequently poured melt. Due to the uncontrolled cooling as well as to the reheating, generation of additional surface area could

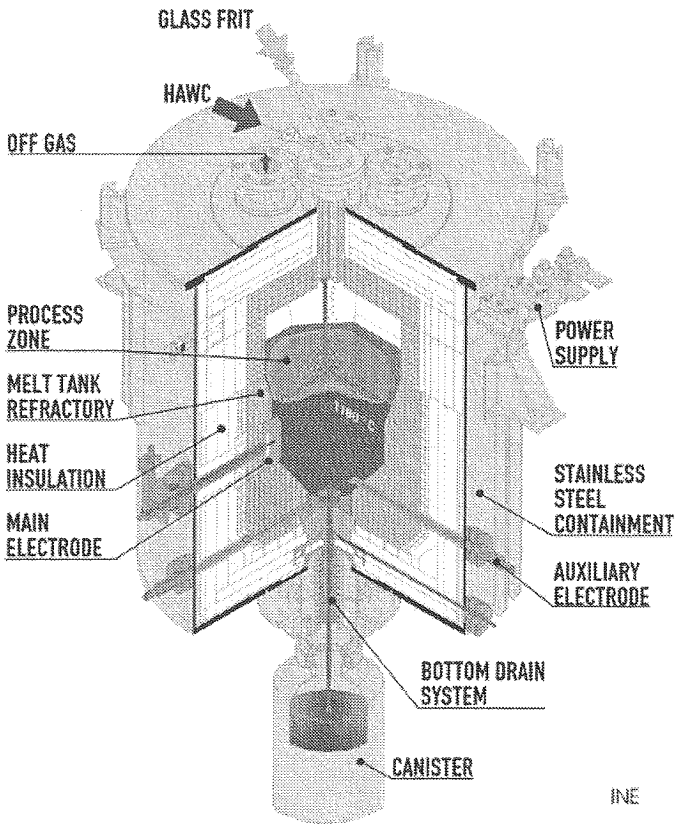

Fig: 1: Perspective cut view of the noble metals-compatible waste glass melter

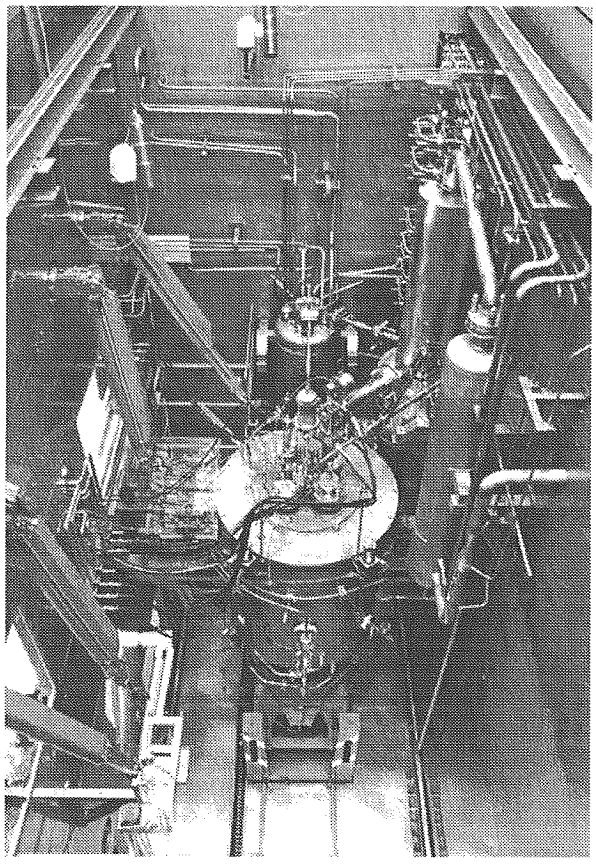

Fig.2: View into the melter cell of INE's prototype test facility

be expected. Moreover, during cooling and reheating the affected part of the glass could be exposed to temperatures which promote crystallization. This thermally induced crystal growth can also lead to an increase of surface and cause a minor leach resistance of the glass.

EXPERIMENTAL PROCEDURE

In support of planning and licensing and later operation of VEK a full-scale nonradioactive prototype test facility (PVA) was constructed at INE and operated from 1998 until 2000 within an extensive experimental program including several long-term test runs [2]. Fig. 2 gives a view into the PVA melter cell.

Within the scope of the PVA test program, product investigations were performed to clarify the uncertainties related to the multiple glass pouring. The boundary conditions of the prototype testing like melt properties, pouring procedure and canister handling were close to that of the envisaged hot operation of VEK. The similarity of the glass melt properties was ensured by a HLW simulation close to the chemical composition of the active waste, and by use of a glass frit composition that will also be applied in hot operation.

A typical glass pouring diagram is shown in Fig. 3. It contains the glass pouring rate, the glass mass poured into canister and the power input of the mean frequency heating used to heat up the glass pouring channel. The glass pouring lasts about 1,5 hours with a glass pouring rate maintained at about 100-130 kg/h.

The identification of the texture of the glass in the interfaces was achieved on the basis of samples that were taken from a filled canister that was centrally cut through. To be able to assign the results to the thermal history of the samples, temperature measurements were performed during pouring by thermocouples placed inside the canisters in the position of the interfaces. The samples were analyzed with respect to chemical composition and extent of crystallization. As the integrity of the glass block inside the canister may suffer from cutting, also a non-destructive method was applied to determine the inner surface caused by fissures or voids. One canister was completely examined by computer tomography generating transmission images.

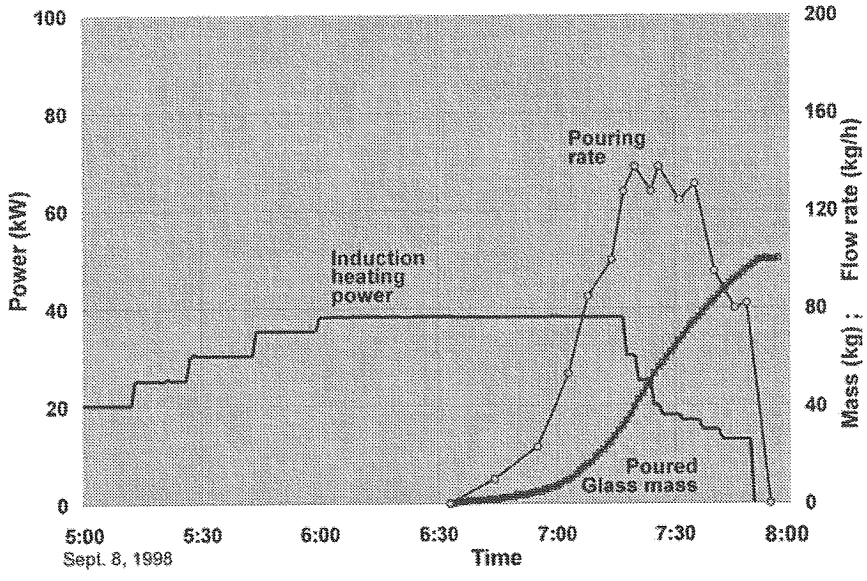

Fig. 3: Typical bottom drain pouring diagram. Power of the induction heating, glass pouring rate and accumulated poured glass mass as function of time

RESULTS

Temperature history

The results of the temperature measurement inside the glass canister are shown in Fig. 4 . It contains the temperature vs. time curves registered by 4 thermocouples placed in the interfaces

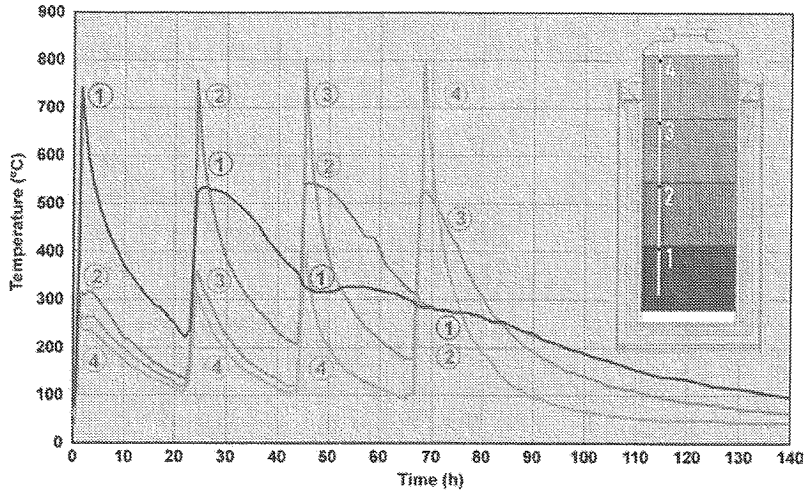

Fig. 4: Temperature vs. time curves from in-can measurement. Position of the thermocouples placed in the surfaces of the poured batches

between the respective pouring batches and in the surface area of the last batch. The positions of the thermocouples are also indicated in this figure.
At the end of the first pouring, when dipping into the glass melt, thermocouple No. 1 experienced a maximum temperature of 740°C. Within the following 20 hours up to the second pouring, the surface cooled down to about 225°C. When the hot glass melt of the second pouring contacted the cool surface, it was reheated and the temperature at position 1 raised up to 530°C. This temperature cycle of cooling and reheating was repeated by the following batches with similar variations (curves No. 2, 3, 4). The surface temperature of each new batch was in the range of 740-800°C, the temperature in the surface of the respective foregoing batch due to cooling and reheating varied between about 200°C and 530°C. Hence, the heat capacity of each actual batch was high enough to increase the temperature of the interface area to temperatures above the softening temperature of about 530°C which at least is necessary to make fusion of the batches possible. The softening temperature along with some other characteristic temperatures are given in Table I. A good agreement of the values of the samples from the interfaces and from the pouring stream can be stated.

Table I: Characteristic temperatures of glass samples

Temperature	Interface samples	Pouring samples
Transformation temperature	492-498 °C	498-506 °C
Softening temperature	531-534 °C	533-544 °C
Temperature of maximum crystal growth	-	740-760°C

Crystallization behavior

Due to the temperature history according to Fig. 4 no significant crystallization tendency had to be expected. Samples taken from the interface areas of a cut canister were analyzed by X-ray diffraction method. An exemplary result is given in Fig.5. It contains the intensity in counts/s plotted against the 2Θ diffraction angle. A few minor peaks can be observed. They are caused by RuO_2-crystals. Due to its low solubility in borosilicate glass melt rutheniumdioxide exists as a separate phase in the glass melt. By the special noble metals design of the melter (see Fig. 1) the concentration of RuO_2 is increased in the interface zone compared to the bulk of the glass. Apart from the presence of RuO_2, no further crystallization could be detected. Obviously, the temperature history associated with the multiple pouring does not influence the glass properties in that way. This issue is confirmed by investigations of the leach resistance in prine, which indicated no deviation between the glass samples taken from the pouring stream and the one taken from the pouring interfaces of a cut canister.

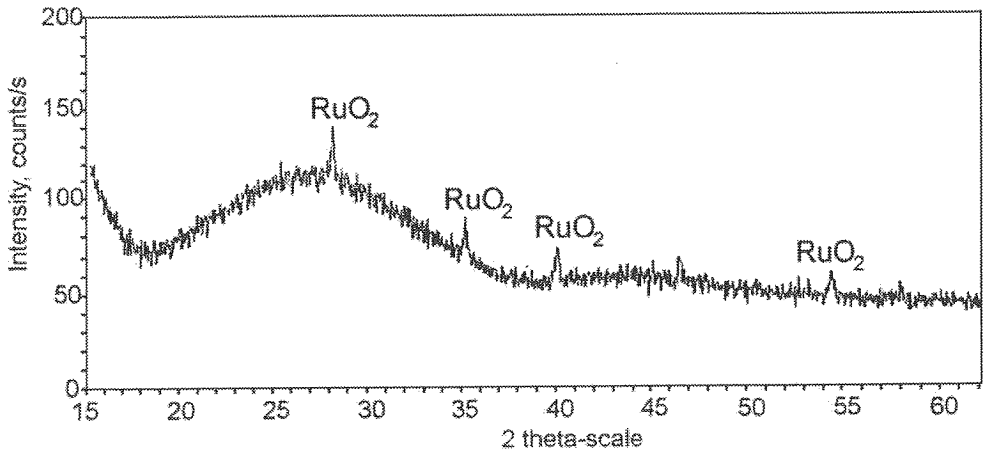

Fig. 5: X-ray diffraction diagram from interfaces samples of a cut canister

Non-destructive examination of the canisterized glass

The nondestructive examination of a canister by radiometric transmission allows the access to information about the internal macroscopic structure of the canisterized glass without mechanical manipulation. Two radiometric methods were applied: Digital Radiography (DR) and Computerized Tomography (CT). Both methods are well established for investigation and characterization of waste form packages [3]. The investigations were performed by Bundesanstalt für Materialprüfung (BAM)/Berlin.

DR was used to get a transmission image of the complete canister. This was achieved by scanning the canister by moving a system of collimated beam of an external source and a detector in a meandering path. A DR image can help to identify and locate larger inhomogeneities and differences in the structure. Such irregularities can then be quantified referring to their nature, shape and size in a selected cross-section by application of CT. The principle of CT is illustrated in Fig. 6. For this investigation a selected cross-section of the canister is scanned by moving the object in a translation/rotation mode through the beam. The statistical correlation of the various beam attenuation results provides images with detailed two-dimensional information about the presence and distribution of fissures etc.. The CT experiments were performed by using an electron linear accelerator with a maximum energy of 11 MeV. The diameter of the cathode spot which influences the resolution of the image, was about 1.5 mm.

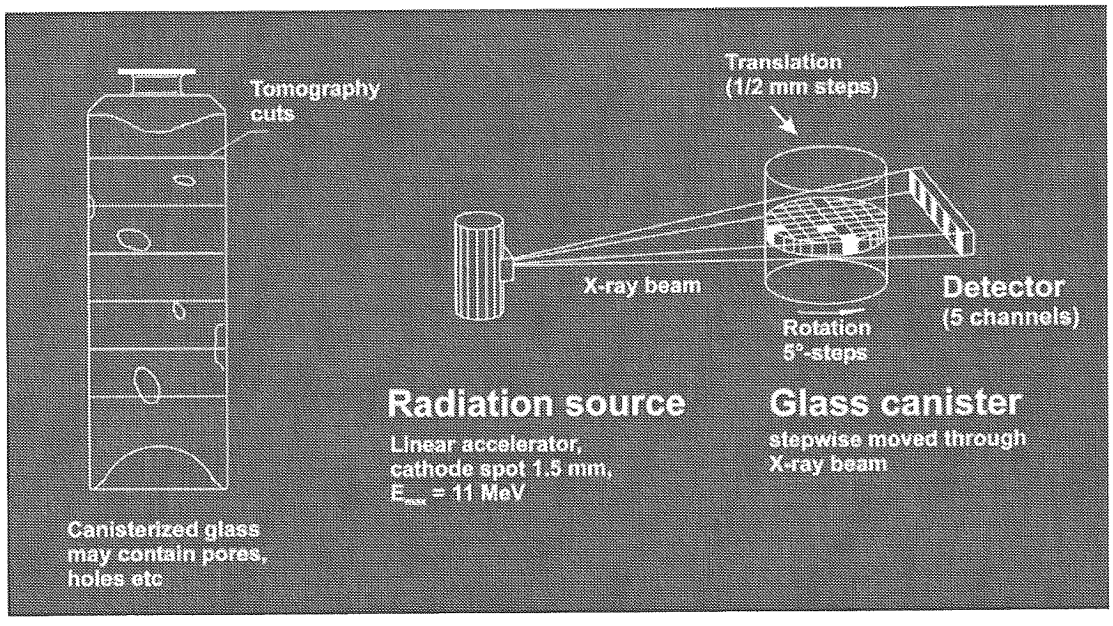

Fig. 6: Principle of the tomography for nondestructive glass canister examination

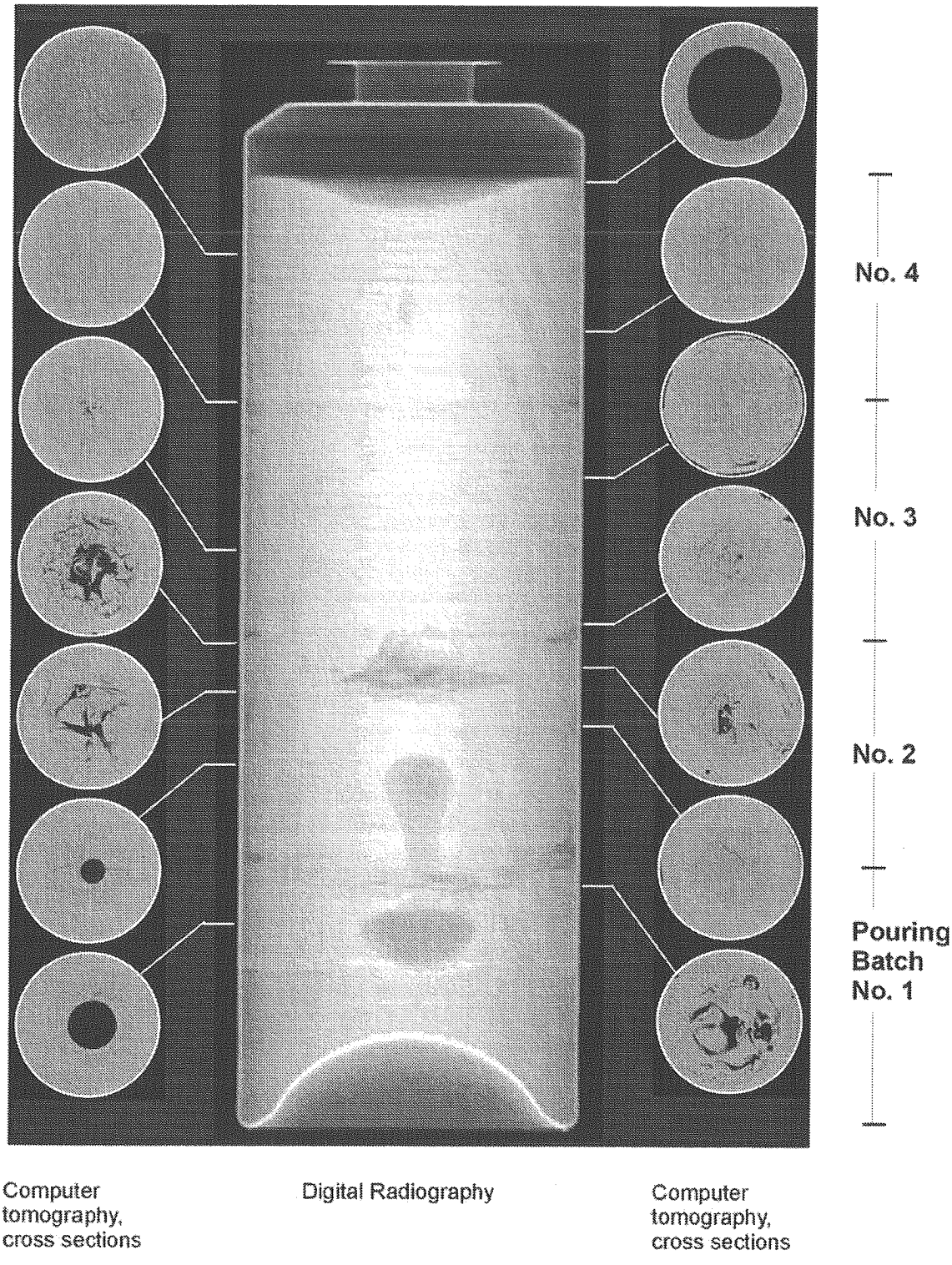

Fig. 7: Results of investigation of the canisterized glass by digital radiography and computer tomography. Glass canister filled by four pouring batches each being 100 kg. Time intervals between pourings approximately 20 h.

The results of the investigations are shown in Fig. 7. It contains an image of the whole canister obtained from digital radiography along with selected cross-sectional images from computerized tomography. The appearance of the canned glass is close to that of a monolithic block. This is especially valid for its upper half. The lower interface layers are well perceptible, whereas the third one

is very weak. Inhomogeneities can be observed in the area of the interface between first and second batch and in a limited spot somewhere below the interface between second and third batch. Moreover, in the lower central part of the glass block a kind of void is visible with a vertical extent of about 250 mm.

A detailed interpretation of the macroscopic structure inhomogeneities can be made on the basis of the tomography results. The structure disorders already identified by the DR image are distinctly visible in the cut views of the respective vertical positions. Fissures can be recognized, which are mainly concentrated in the inner part of the cross-section. The void also already detected by DR turns out to be of a sharp-edged circular shape, which is nearly concentric to the canister side. It possibly arose from accumulation of gases.

From the 2D results of the CT measurements, spatial information about size and distribution of fissures and voids can be deduced by using suitable statistical tools. The resulting inner surface is of importance with respect to the potential chemical leaching of a waste glass product inside a final disposal site. The criterion used is formed by the ratio of the inner surface, generated by fissures etc. and of the outer geometrical surface of the glass, defined by the cylindrical shape including bottom and top surface. The calculations derived from the above results yielded a surface ratio between total surface and the geometrical one of 6.4. This is far below the conservative number assumed as a kind of limit in respect to final disposal.

SUMMARY AND CONCLUSIONS

By operation of the future FZK vitrification plant European standard glass canisters will be produced which will be filled by four pouring batches. As the canisters will remain unheated the maintenance of waste form quality properties like homogeneity, portion of crystallization and inner surface have been questionable. Temperature measurements inside glass canisters produced by a prototype test facility showed that the cooled surface of the glass is reheated by the following batch up to the softening temperature. Investigation of glass samples from a cut canister revealed no evidence for an enhanced crystallization in the interface of the poured batches. The non-destructive examination of a canister by radiometric methods yielded a nearly monolithic appearance of the canisterized glass. Only a few limited regions of fissures and one considerable void contributed to a low surface ratio of 6.4, which is distinctly below the limit of 20. From all that it can be concluded, that the multiple pouring has no negative effect on the glass product to be expected.

REFERENCES

[1] G. Roth, S. Weisenburger, "Vitrification of high-level liquid waste: process chemistry, glass chemistry and process technology," Nuclear Engineering and Design 202 (2000) 197-207

[2] W. Grünewald, G. Roth, W. Tobie, K. Weiß, "Cold demonstration of the VEK vitrification technology in a full-scale mock-up facility, WM2K-Conferene, Febr 27-March 2, 2000, Tucson, Arizona, USA

[3] J. Goebbels et al., "Non-destructive examination of nuclear waste packages by advanced radiometric methods", European Comission report EUR 18040

Sorption behaviour of Am on precorroded HLW glass in water and brines

B. Luckscheiter and M. Nesovic

Introduction

Contact of glass by an aqueous solution results in the diffusion of water into the glass surface and ion exchange of the alkali metal ions against H_3O^+. The dissolution of the glass occurs by hydrolyses of the silicate network. The network hydrolyses reaction can be written as

$$\equiv Si\text{-}O\text{-}Si\equiv + H_2O = \equiv SiOH + HO\text{-}Si\equiv$$

or

$$\equiv Si\text{-}O\text{-}Si\equiv + OH^- = \equiv SiO^- + HO\text{-}Si\equiv$$

The reverse reactions are referred to as condensation reactions. The hydrated silicate network subsequently dissolves and in a closed system the solution becomes saturated with repect to $Si(OH)_4$ within a few days. When silica approches its solubility limits, condensation reactions of the silanol groups take place forming a largely amorphous alteration layer (gel layer). The initial high dissolution rate (forward rate) of the glass decreases by several orders of magnitude.

As described in literature, e.g.[1,2,3,4], during the initial stage of corrosion, when the solution concentrations of glass components are too low to significantly affect the corrosion rate, the glass dissolves stoichiometrically. This may be valid in dynamic leaching tests. However, static corrosion tests with the HLW glass GP WAK1 (this glass was developed for the vitrification of the HLLW of the reprocessing plant in Karlsruhe, WAK) in water at 80°C have shown, that even during the initial 50 hours of corrosion at pH values between 4 and 9 the glass dissolution is not stoichiometric. From the beginning the release of less soluble elements, e.g. Al, Fe, REE, is even lower by about a factor of 10 and more than that calculated based on the release of B or Li. Obviously, the less soluble elements are retained in

the alteration layer of the glass by sorption or, with increasing reaction time, by formation of secondary alteration products controlling the solution concentrations.

Sorption behaviour of Am on precorroded glass

In order to quantify the sorption effect on the retention of metal ions, sorption tests were performed using precorroded, simulated HLW glass GP WAK1 as substrate. In previous tests, the retention of Eu (homologue element for trivalent actinides), Th (homologue for Pu(IV), U(IV) and Np(IV) and U(VI) was investigated in water and brines as a function of pH [5]. In water, the sorption behaviour of these elements show a strong dependence on pH and the sorption coefficients (R_s, see below) reflect the different charge of the three ions. As shown in Fig. 1, the R_s values are highest for Th, followed by the R_s values of Eu, which are lower by about a factor 10 and finally the R_s values of U(VI) which are the lowest. The results of these sorption tests show clearly that the alteration layer on the glass surface has a strong effect on the retention of the three elements.

To demonstrate that the sorption behaviour of Eu is really representative for homologue trivalent actinides, additional sorption tests were performed with Am^{241} in water as well as in brines. In the presented paper, the determined sorption coefficients for Am between pH 2 and 10 are compared to the respective coefficients of Eu.

Experimental

Sorption studies were performed in deionized water and NaCl-rich and $MgCl_2$-rich solution at 80°C as a function of pH under atmospheric conditions. For preparing precorroded glass samples, several samples of 2.5 g glass powder (grain size 200-280 µm) were exposed to 50 ml solution (S/V = 1000 m^{-1}) for 40 days as in the previous tests with Eu [5]. After 40 days aliquotes were taken from the leachates and analysed for various elements (Li, B, Si, Nd, Ce). From the concentrations of B and Si, the amount of the alteraton layer formed was calculated. After sampling, the pH of the solutions was adjusted to different fixed values between pH 2 and 10 by addition of HNO_3. Due to the reaction with the glass, the pH of the solutions increases permanently, especially at pH 4 to 6. Therefore, the pH was daily measured and readjusted to the fixed values. After several days of pH adjustments, the change

of pH in the solutions slows down. For the sorption studies, Am concentrations of 10^{-9} up to about 10^{-7} mol/L were used. The concentrations of Am in the leachates were determined by γ-spectrometry 10 days after adding stock solutions of Am^{241} to the leachates. In some experiments also the Am concentration after 30 days were used to check the effect of reaction time. For solution analyses, aliquots were taken and filtered through 0.45 μm filters. The filtrates were also passed through an ultrafiltration membrane (pore size 1.8 μm).

For the sorption tests in salt solutions, the glass powder was precorroded in the same way as described above, in water at 80°C. After 40 days, salt was added to the solution to install solution concentrations of 5.5 mol/L NaCl and 5 mol/L $MgCl_2$ and the pH of the solutions was adjusted to various fixed values. Some days later, stock solutions of Am^{241} were added.

Results and Discussion

Results of the sorption experiments are given in the figures in terms of R_s (L/kg) values as a function of pH ($R_s = Am_{sorb}/Am_{sol} \times V/m$; Am_{sorb} = amount of Am sorbed, Am_{sol} = Am concentration in the solution, V= solution volume, m = mass of alteration layer). R_s values were calculated for filtered and ultrafiltered solution samples to check for colloid formation.

Sorption behaviour in water

Sorption coefficients (R_s) of Am at 80°C for three starting concentration of 10^{-9}, 10^{-8} and 7×10^{-8} mol/L as a function of the pH after 10 days contacting time are shown in Fig. 2. The three sorption tests were performed with the same water solutions and glass powders. Starting with the lowest Am concentration and, after increasing twice the Am concentration, finally with the highest concentration. The sorption edges are shifted slightly to higher pH values with increasing starting concentration. This is an effect of the non-constant pH in the solutions, especially during the first sorption test at the lowest starting concentration. In the last test with the highest Am concentration, the changes in pH (about one unit per day at pH 3 to 5) were much lower than in the previous tests. Therefore, the R_s values determined at the highest starting concentration are more reliable. Above pH 7, the R_s values determined at the highest starting concentration decrease again. This effect may be related to the formation of anionic carbonate complexes, because the solutions are in contact with air.

At pH values above 5, Am-bearing colloidal particles were detected in all sorption tests in water. The Am concentrations in the 450 nm filtered solution samples and above all in the unfiltered samples were much higher than in the ultrafiltered solutions (1.8 nm). The respective R_s values are included in Fig. 2 to illustrate the colloidal effect. The Am concentrations in the ultrafiltered solutions of 10^{-10} to 10^{-11} mol/L are far below the stability region of $AmOHCO_3$ (cr) or $Am(OH)_3$ (am), the stable solid phases under these conditions. Compositional EDS analyses of the filter residues revealed that the Am-bearing colloids mainly contain silica. Therefore, the colloids may consist of detached fine gel-layer particles containing sorbed Am.

Fig. 3 shows a comparison of the R_s values of Am with those of Eu, determined in previous tests, at various starting concentrations. Despite the relatively large scattering of the data points, it is quite evident that the sorption behaviour of Am is nearly identical with the behaviour of Eu. As shown by the previous sorption tests with Eu, at constant pH the sorbed concentration is about proportional to the solution concentration. Therefore, the sorption behaviour of Eu and Am can be described by a Nernst/Langmuir isotherm [5].

The strong dependence of the R_s values on the pH can be explained by a surface complexation reaction of Me(III) ions with the alteration layer. For the modelling calculations described by Luckscheiter and Kienzler [5] only the SiOH surface complex was regarded, as about 80% of the gel layer consists of SiO_2, two sites/nm^2 and only one sorption site species were assumed. As shown by the modelling results, the sorption data obtained from Eu and Am can best be described by the formation of a bidentate surface complex:

$$2 \equiv SiOH + Me^{3+} \longleftrightarrow (\equiv SiO)_2Me^{+} + 2H^{+}$$

Sorption behaviuor of Am in brines

For the sorption studies in brines, the glass powder was precorroded in the same way as dercribed above, in water at 80°C over 40 days. After precorrosion salt was added to the solutions to install concentration of 5.5 mol/L NaCl and 5 mol/L $MgCl_2$ and the pH was adjusted to various fixed values. The Am starting concentrations were between 10^{-8} and 10^{-7} mol/L.

The sorption edges of Am in the NaCl brine at 80°C in comparison with the sorption edge of Eu at the starting concentration of 10^{-4} shows Fig. 4. Again, the sorption coefficients of Am agree quite well with the R_s values of Eu. Like the sorption coefficients of Eu, the R_s values of Am are considerably lower than in water (see also Fig. 5) and appear to be independent of the starting concentrations. Am-containing colloidal particles could not be detected over the entire range of pH. During precorrosion of the glass and the sorption tests, Nd and Ce (as well as other REE) are leached out from the glass. From the Nd and Ce concentrations in the solution „desorption" ceofficients can be calculated. These R_d data of Nd and Ce included in Fig. 4 correspond quite well with the R_s data of Am and Eu. Consequently, the retention of REE found in corrosion experiments in NaCl brine can be explained by sorption onto the alteration layer of the glass. (A corresponding agreement between the R_s values of Am/Eu and the R_d values of Ce /Nd was found in the sorption tests in water as well as in $MgCl_2$ brine).

The sorption behaviour of Am and Eu in the $MgCl_2$ brine between pH 2 and 6.5 is shown in Fig. 5. The pH values are corrected for liquid junction potential. Compared to the behaviour in water and NaCl brine, also shown in the figure, the R_s values of Am and Eu in the $MgCl_2$ brine are much lower. After an initial sharp rise at low pH, the R_s values rise slowly up to pH 6.5. Like in water and NaCl brine, the sorption coefficients of Am and Eu are rather similar. The low retention of Eu and Am in $MgCl_2$ brine can be explained by

competition of Mg^{2+} ions which occupy the sorption sites in the gel layer because of their high excess. A further, reasonable explanation for the lower sorption could result from the formation of clay-like Mg silicates, a common alteration product to form in the gel layer [6]. Due to the formation of, e.g., smectite-type clays a decrease in pH is typical for glass corrosion experiments in Mg-rich solutions. The sorption tests with smectite clays revealed a rather low sorption of Am and REE onto the clay below pH 6 [7].

From the presented results of the sorption studies with Am and Eu in water and brines, it is in evidence that the sorption behaviour of trivalent REE onto the gel layer of HLW glasses is also representative for the behaviour of homologue trivalent actinides.

Summary and conclusions

In the surface layer of corroded glasses less soluble elements are retained by sorption or by formation of secondary alteration products. To study the sorption effect, sorption tests were performed with Am(III) using precorroded, simulated HLW glass as substrate in water and NaCl and $MgCl_2$ brine at 80°C. Am sorption was studied as a function of the pH at starting concentration between 10^{-9} and 10^{-7} mol/L Am^{241}. The objectives of the sorption tests were: quantification of the sorption effect on the retention of Am during long-term glass corrosion, comparison of the sorption behaviour of Am with the behaviour of Eu and identification of the sorption mechanism.

The results of the sorption studies with Eu and Am in water and brines using precorroded glass as substrate show clearly that the sorption behaviour of Eu is really representative for trivalent actinides. In water, the sorption coefficients of Am show a strong increase up to pH 6. Above pH 7 the sorption coefficients decrease again due to the formation of anionic carbonate complexes. As shown previously by the sorption tests with Eu, the sorption

behaviour of Am at constant pH can be described by a Langmuir isotherm. Am-bearing colloidal particles could be detected above pH 5. Presumably, the colloidal particles consist of fine gel-layer particles detached from the glass surface. The strong sorption of Eu and Am on the gel layer at low pH in water indicate the formation of a bidentate surface complex and a high number of active sites in the gel.

In 5.5 M NaCl brine, the sorption coefficients of Am are considerably lower by about a factor 10 and in 5 M $MgCl_2$ brine significant lower by about factor of 100 than in water. Am-containing colloidal particles could not be detected in both brines. The low sorption of Eu and Am observed in $MgCl_2$ brine can be explained by competition of the Mg^{2+} ions which occupy the active sites in the gel layer because of their high excess. A reasonable explanation for the lower sorption could also result from the formation of clay-like Mg silicates, a common alteration product to form in the gel layer of the corroded glass.

References

1. Ebert, L.: The Effects of the Glass Surface Area/Solution Volume Ratio on Glass Corrosion: A Critical Review.ArgonneNational Laboratory Report ANL-94/34 (1995).
2. Grambow, B.: Nuclear Waste Glass Dissolution: Mechanism, Model and Application, Technical Report, JSS Project Phase IV 87-02, edited by SKB, Stockholm, Sweden (1987)
3. Vernaz, E.Y., Dussossoy, J. L.: Current state of knowledge od nuclear waste glass corrosion mechanisms: the case of R7T7 glass. Appl. Geochem. 1, 13 (1992).
4. Vernaz, E., Grambow, B., Lutze, W., Lemmens, K. and Van Iseghem, P.: Assessment of the Long-Term Durability of Radioactive Waste Glass. 4. Conference of the European Commision on the Management and Disposal of Radioactive Waste, Luxembourg 25-29 Mars (1996).
5. Luckscheiter, B., Kienzler, B.: Determination of sorption isotherms for EU, Th, U and Am on the gel layer of corroded HLW glass. J. Nucl. Mater. 298, 155 (2001).
6. Abdelouas, A., Crovisier, J.L., Lutze, W.,Grambow, B., Dran, J. C., Müller, R.: Surface layers on a borosilicate nuclear waste glass corroded in $MgCl_2$ solution. J. Nucl. Mater. 240, 100 (1997).
7. Coppin, F., Berger, G., Bauer, A., Castet, S., Loubet, M.: Sorption of lanthanides onto smectite and kaolinite. Chemical Geology, in press 2001.

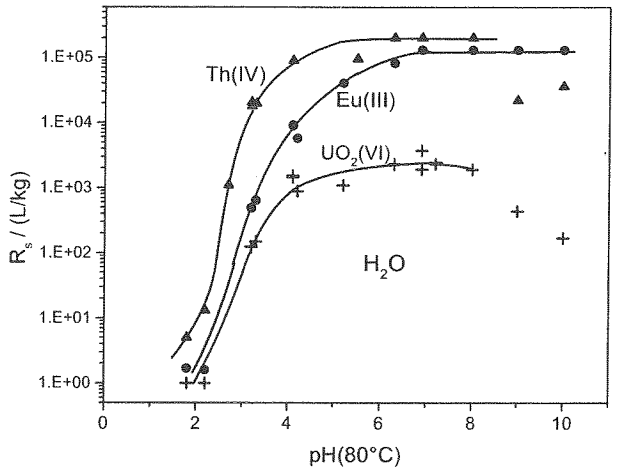

Fig. 1: Sorption coefficients R_s of Eu, Th and U on precorroded HLW glass in water

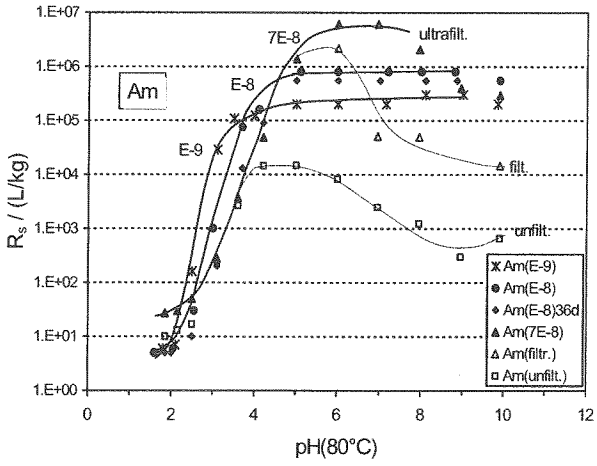

Fig. 2: Sorption coefficients R_s of Am on precorroded HLW glass in water

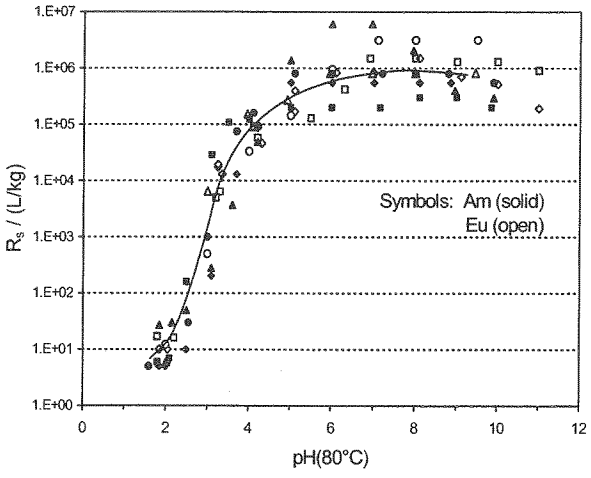

Fig. 3: Comparison of the sorption coefficients R_s of Eu and Am in water

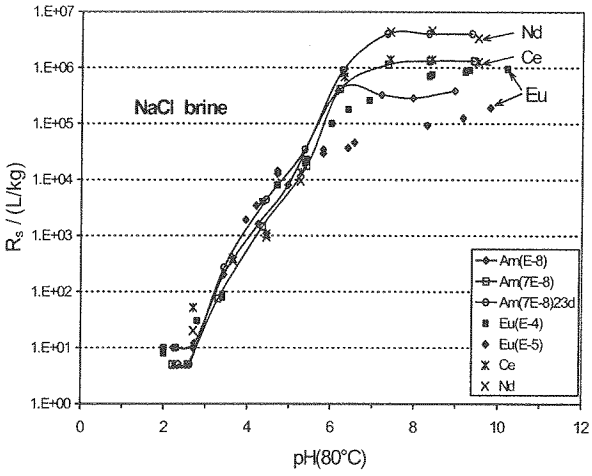

Fig. 4: Sorption coefficients R_s of Am (curves) and Eu (solid symbols) in NaCl brine and „desorption" coefficients of Ce and Nd (x)

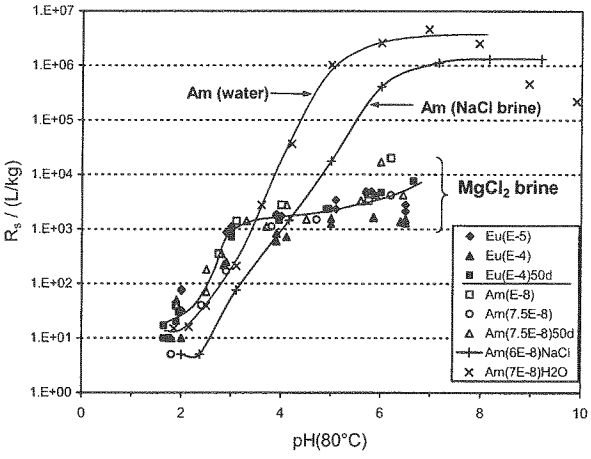

Fig. 5: Sorption coefficients Rs of Am and Eu in $MgCl_2$ brine as well as the sorption edges of Am in water and NaCl brine

IMPACT OF HYDROGEN OVERPRESSURE ON SPENT FUEL CORROSION BEHAVIOR IN SALT SOLUTION

A.Loida, B. Grambow., H. Geckeis, N. Müller*
*FZK(INE), * Ecole de Mines de Nantes, F- 44307 Nantes*

Introduction

In the German disposal concept spent nuclear fuel has to be canistered in heavy weight steel packages and to be disposed off in a deep geological repository, located in the salt dome of Gorleben (Additionally, due to a decision of the German government other host rock formations than rock salt are under consideration, too). The long-term safety of a repository containing long-lived high radioactive waste is to be guaranteed by a system of barriers, the "multibarrier system". The barriers are the engineered or technical barrier (waste form and container = waste package), the geotechnical barrier (backfill materials, underground dams, borehole sealings) and the geologic barrier (the host rock formation itself and its overburden). All barriers contribute to isolate the radionuclides from the biosphere by (i) retardation of groundwater access and by (ii) their retention on solid surfaces present in the repository. Assuming that saline solutions in the vicinity of the waste package would find access to these packages, they will corrode, and after breaching of the container and the cladding the brine will interact with the spent fuel matrix.

To assess the ability of this waste form to retain radionuclides in the case of water access, and to understand the corrosion controlling processes, it is required to perform experiments, which simulate the overall system consisting of real spent fuel, canister material, salt brine and gas phase. Both, the dissolution rate of the spent fuel itself, and the release/retention of radionuclides are expected to be governed more by geochemical constraints encountered in the near field of the waste package, rather than by inherent material properties of the fuel. Conditions such as the redox potential and the pH of the solution as well as the availability of oxidative radiolysis products are key parameters controlling the overall alteration behavior of spent fuel. The gas phase composition depends strongly on the corrosion process of the metallic canister material, but also on the α-, β- and γ- radiolysis of the solution. In the case of container corrosion hydrogen is the dominant constituent of the gas phase and under these conditions overall reducing near field conditions are assured. However, close to the spent fuel surface (some μm) the persistence of oxidizing radiolytic species cannot be ruled out. The built up of hydrogen overpressure in a repository is considered to produce problems with respect to the overall safety [1]. In the frame of our experimental work special attention is directed towards the evolution of hydrogen and its effect on the overall corrosion behavior of high burnup spent fuel.

Various experiments are performed to quantify to what extent the hydrogen overpressure may counteract oxidizing effects of radiolysis products in a carbonate free environment in 5 m NaCl solution. This comprises corrosion studies of high burnup spent fuel pellets in the presence/absence of iron and its corrosion products. In these studies, the evolution of hydrogen is monitored continuously. Additional experiments are conducted under an external H_2 overpressure of ca. 3.3 bar in the absence of iron. This hydrogen partial pressure is similar as analyzed in a previous long-term spent fuel corrosion test in the presence of Fe powder [2].

Experimental

Pellet sized segments each ca. 6.6 g fuel, and ca. 10 mm in length, samples K8 and K14 (addition of 9 g magnetite powder), of high burnup spent fuel (50 MWd/kg U, linear power 260W/m, from PWR Gösgen, CH) were corroded under anoxic carbonate free conditions in 200 ml 5m

NaCl solution. Several wash cycles in quartz glass vessels of ca. 280 ml volume with complete renewal of the solution were carried out (1) to ensure that the main part of the instant release fraction was removed, and (2) to dissolve oxidized layers possibly formed on the cut pellet surface during storage. The vessels are equipped with fittings on the top to allow the introduction of Ar gas atmosphere, the connection with the gas sampling device and solution sampling under streaming Ar gas. Prior to start each test run the system (leachate and vessel) was flushed with Ar and then remained undisturbed. The leachate was replaced entirely by fresh Ar flushed solution for the sample K8 six times at intervals between 1 day and 213 days, where seven times sampling of gases and solution was performed (two samplings during the 213 days interval). In the test with sample K14 + magnetite the solution was replaced five times at intervals between 3 and 78 days, again associated with gas and solution sampling. In Table I data of the used samples and test conditions are compiled, additionally data from spent fuel pellet samples K3, K4, K9, K10 of an earlier study [2,3] are displayed for comparison.

Table I. Experimental Data Related to Anoxic Corrosion Tests of High Burnup Spent Fuel Pellet (m_{fuel} ca. 6.6 g) in 5 m NaCl Solution in the Absence of Carbonate.

Sample	Addition of	Kind of test	Individual Sampling Intervals (days)	Sum *** (days)	Total Test Duration (days)	Ref.
K 8*	-	5 x repl. of solution	1,2,18,21,38	80	80	this work
K 8*	-	Static phase	77,136	213	292	this work
K 8	-	**Static test, 3.3 bar ext. H2 overpr.**	**53, 64, 96**	**213**	507	this work
K 14*	9 g Magnetite	5x repl. of solution	3,20,20,22,78	143	143	this work
K 9**	-	static	1183	1183	1624	[2,3]
K 10**	-	static	236	236	678	[3]
K 3**	7 g Fe-powder	static	236	236	674	[3]
K 4**	7 g Fe-powder	static	1181	1181	1619	[2,3]

*wash cycles **data from the last sampling interval of the test ***of individual sampling intervals

Sample "K8" was used for the test under H_2 overpressure. To apply the desired H_2 overpressure a Ti/Pd-lined stainless steel autoclave with a total volume of 500 ml, equipped with an external pressure gauge and two ball valves, enabling to take gas samples and solution samples under streaming Ar was used. The Ti/Pd liner material is known to be very corrosion resistant and to maintain inert conditions during the experiment. The starting volume for this test was 200 ml. By inserting of 40 bar of a gas mixture of Ar/8% H_2 a hydrogen overpressure of ca. 3.3 bar was achieved. The pressure remained constant at 40 bars during each leaching interval, until sampling of gases and solutions were performed. The total static test duration under external hydrogen overpressure was 213 days so far. Fig. 1 shows the glass reaction vessel and the high pressure autoclave when prepared to take a gas sample, and the surface of spent fuel pellet K8 seven years after cutting, prior to insert into the test.

Samples from the gas atmosphere were taken at intervals as indicated in Table I. The reaction vessel was connected with an evacuated (10^{-6} bar) 50 cm^3 gas collection cylinder. Prior to sampling the connecting tube system was several times flushed with Ar and evacuated afterwards to remove effectively the remaining amount of air. The gas composition was analyzed quantitatively by a quadrupole mass spectrometer (GAM 445, Balzers Liechtenstein). The calibration was performed, using a gas mixture with known amounts of H_2, N_2, O_2, Kr and Xe in Ne.

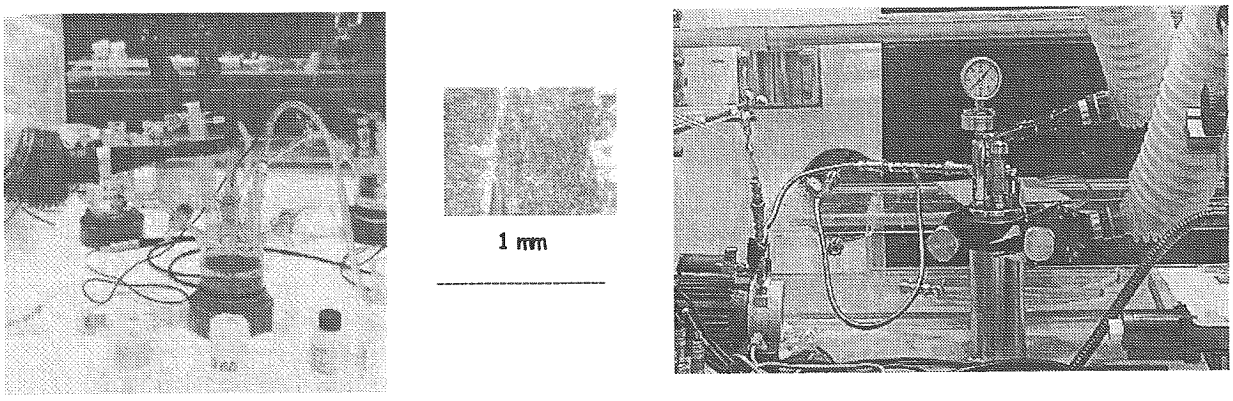

Figure 1. Reaction Vessels Used for Corrosion Tests of Spent Fuel. Glass Vessel (left): Wash Cycles. High Pressure Autoclave: Test Runs Under External H_2 Overspressure (right). Cut Surface of Spent Fuel Pellet "K8" after 7 Years Storage (middle).

Solution samples were taken immediately after the gas sampling. All solution samples were filtered through a 0.45μm filter to avoid the uptake of fuel particles. Aliquots were additionally filtered by 1.8 nm ultrafilters to identify by comparison to the 0.45μm filtrates upper limits for colloid formation. Solutions were analyzed by α- spectrometry (^{238}Pu, $^{239/40}$Pu), γ -spectrometry (^{125}Sb, $^{134/137}$Cs, ^{144}Ce, ^{241}Am, $^{154/155}$Eu), LSC (^{90}Sr, ^{241}Pu) and ICP-MS (^{99}Tc, ^{237}Np ^{238}U). Radiochemical and gas analyses procedures are described in detail in [3]. Measured pH – data were corrected for liquid junction potential. Liquid junction potentials were obtained by measuring the pH value of the leachants with known activity a_{H^+} [4]. Reported pH values are consistent with Pitzer's pH convention (ionic splitting convention).

Results and discussion

There are first indications in the literature that radiolytically enhanced fuel oxidation/fuel dissolution may be suppressed effectively by high pressures of hydrogen gas, generated by canister corrosion [2,5]. Significant amounts of hydrogen gas were found when pellet sized high burnup (50 MWd/kgU) spent fuel samples were corroded under static conditions over 4.5 years in the presence of initially metallic Fe powder in 5 m NaCl solution in the absence of carbonate. A hydrogen overpressure of 2.75 bar was built up during the last two sampling intervals, which lasted ca. 3 years, when the system remained undisturbed. Simultaneously, the progress of matrix dissolution appeared to stop, as indicated from the rate of released fractions of the Sr (or Cs) inventory of the fuel into solution (dissolution rate < $1x10^{-9}$/d). The concentrations of important radioelements such as Am, Pu, Tc, U in solution were significantly lower than anticipated from the total amount of dissolved fuel. They were found to be < 10^{-11} (Am), $4.1x10^{-11}$ (Pu), $5.4x10^{-9}$ (Tc) and $2.8x10^{-8}$ (U) mol/l, the pH was determined to be 9.5. During a parallel test performed under similar conditions, but in the absence of Fe a radiogenic hydrogen overpressure of 0.2 bar was measured, with a corrosion rate being ca. 2 orders of magnitude higher ($4.6x10^{-7}$/d, as deduced from Sr-release). The Am, Pu, Tc, U concentrations were as well higher (Am $4.3x10^{-11}$, Pu $5.1x10^{-10}$, Tc $6.4x10^{-7}$ and U $1.5x10^{-6}$ mol/l. In Fig. 2 the release rates of Sr, Cs, Pu and U are plotted in units of FIAP/d (FIAP: Fraction of the inventory in the aqueous phase) as a function of H_2 final overpressure in the range between $5.23x10^{-4}$ and 2.75 bar as observed in various spent fuel corrosion tests. Data were compiled from tests in the absence/presence of metallic Fe, or Magnetite, performed in 5m NaCl brine under anoxic carbonat free conditions. The time intervals for sampling of solution and gases were ranging

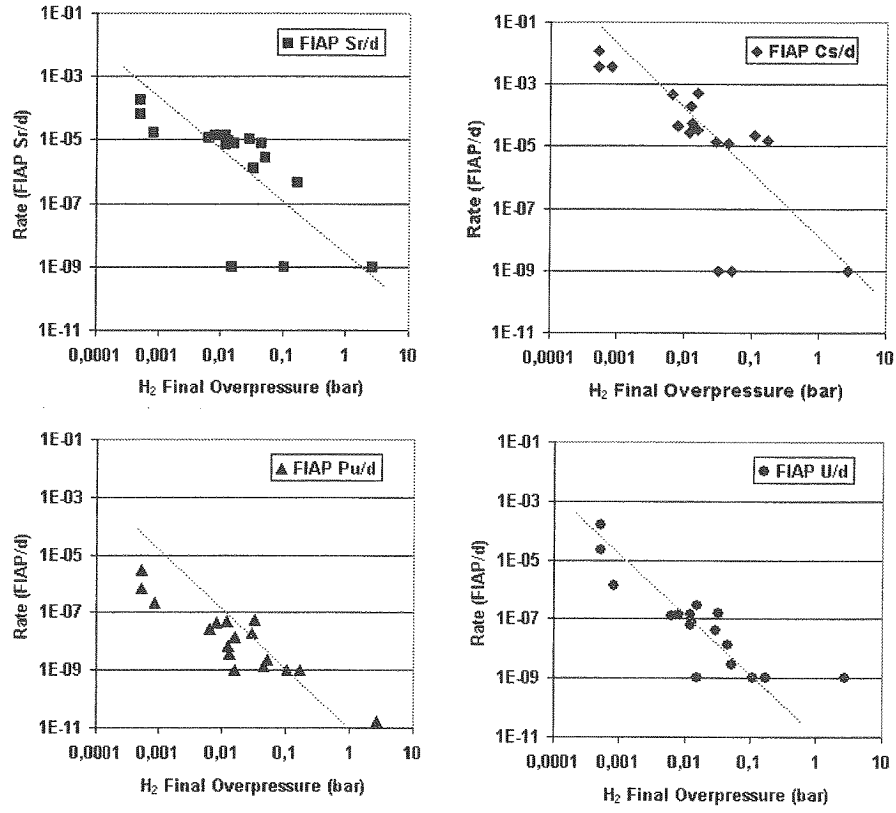

Figure 2. Released Fractions of the Fuel Inventory in the Aqueous Phase of Sr, Cs, U, Pu per Day as a Function of Hydrogen Final Overpressure from Various Spent Fuel Corrosion Tests.

between 1 day and 1085 days (details see "Experimental, Table I"). The diagrams in Fig.2 reveal that the release rates of radionuclides decrease, if the H_2 overpressure increases.
There is no clear evidence which oxidative reaction could be affected by the H_2 overpressure [6]. H_2 could either react with the fuel surface to reduce initially oxidized species, or it could interact with oxidizing radiolytic species. The only known reaction of molecular H_2 with an oxidizing radiolysis product is that with the OH-radical resulting in the formation of a H_2O molecule and a H-radical. The produced H-radical could react with other oxidative species, for example with radiogenic H_2O_2 (to produce again the OH radical) or with dissolved oxygen. An overview on possible reactions, reaction products and rate constants is given in Table II according to Sunder & Christensen [7].

The results of the static test obtained under 3.3 bar H_2 overpressure up to 117 days are presented together with the data of the preceding wash cycles. The release of important radioelements into solution is shown in Fig. 3 in units of FIAP. The associated released fractions of fission gas (FG: Kr, Xe) are plotted as well.
The greatest part (>84%) of the instant release fraction (IRF: labile radionuclide fraction, encountered upon the fuel sheath gap, fracture surfaces, grain boundaries to be released instantaneously upon water contact to the fuel) was released into solution, as indicated by the Cs release within the first 80 days, when the solution was replaced 5 times. During this time the released fraction of Cs ($FIAP_{Cs}$) decreased from initially ca. 10^{-2} to 10^{-3}. Thereafter it was found to be in the same range as the release fraction of Sr, indicating that Cs data may be used as well to describe matrix dissolution. By using the data of Sr and later Cs releases into solution as indicators for the progress of matrix degradation, the dissolution of the UO_2-matrix, was found to be between ca.10^{-5}/d (initial stage) and ca.10^{-6}/d (after 292 days). This is ca. 1-2 orders of

Table II: Possible Reactions and Rate Constants, Relevant for the Chloride System According to Sunder and Christensen [7]

Reaction	Rate constant (l/mol*s)
$H_2 + OH = H + H_2O$	K = 3,4 E 7
Water	
$H + H = H_2$	K = 7,4 E 9
$H + O_2^- = HO_2^-$	K = 7,4 E 9
$H + HO_2 = H_2O_2$	K = 2,0 E 10
$H + H_2O_2 = H_2O + OH$	K = 9,0 E 7
$H + O_2 = HO_2$	K = 2,1 E 10
$H + OH^- = E^- + H_2O$	K = 2,2 E 7
Salt brine	
$H + Cl = Cl^- + H^+$	K = 1,0 E 10
$H + Cl_2^- = Cl^- + Cl^- + H^+$	K = 8,0 E 9
$H + ClOH^- = Cl^- + H_2O$	K = 1,0 E 10
$H + Cl_2 = Cl_2^- + H^+$	K = 7,0 E 9
$H + HClO = ClOH^- + H^+$	K = 1,0 E 9
$H + Cl_3^- = Cl_2^- + Cl^- + H^+$	K = 1,0 E 10

magnitude higher than found in an earlier test, carried out under similar experimental conditions [3]. The reason might be the formation of an oxidized surface layer on the pellet due to potential air intrusion into the supposed air-tight storage capsule, where it was kept over > 7 years after cutting. The released fractions of the fission gas inventories (Kr, Xe) increased at first strongly up to ca.10^{-1} and could not be associated with the release behavior of Cs. Matrix bound radioelements as Tc, Np, Pu, U, Eu and Am were retained as shown by their FIAP values found ca. two orders of magnitude below the fractions of Sr in solution. During the static phase of the wash cycle (still in the absence of external H_2 overpressures) up to 292 days since start of the test a significant increase of Eu and Am fractions (ca. 2 orders of magnitude) and less pronounced for Np, Pu, U, Tc (max. 1 order of magnitude) was found as compared to the initial wash cycles under replenishment conditions. During this stage the matrix dissolution rate remained on the same level, as indicated by the releases of Sr and Cs.
The pH was found to be around 7.9 during the initial stage of the test up to 80 days followed by a decrease to 7.4 and 6.8 respectively.

Under the **impact of 3,3 bar H_2 overpressure** (40 bar Ar/ 8% H_2) applied after initial 292 days of corrosion (wash cycles) in the absence of Fe, the pH dropped to 4.9 during the first 53 days, for which no explanation was found so far. Then it increased again to 7,7 within the next 160 days of the static test. The radioelement Sr was found to be released in solution at relatively high levels during the first 53 days indicating that matrix degradation continued relatively fast. This was probably due to the low pH. In the following time intervals of 64 and 96 days its fraction in solution remained constant at ca. $5x10^{-5}$ ($FIAP_{Sr}$). The release fraction of Sr was more than one order of magnitude lower than found during the static test in the preceded wash cycles. A similar release behavior was observed for Cs, the released fractions of Cs were reduced at a factor of ca. 5, but they were encountered again higher than the released Sr fractions. The released fractions of fission gases (Kr, Xe) were now close to the ones of Cs. The again higher release rates of Cs and fission gases may be explained by reduced matrix dissolution rate (Sr data) making grain boundary contributions to become "visible" again: If grain boundary release rates after 300 days are about 10^{-5}/d this contribution could not be detected for Cs in the wash cycle because matrix bound Cs release (as indicated by Sr data) was in the same order. Now, in

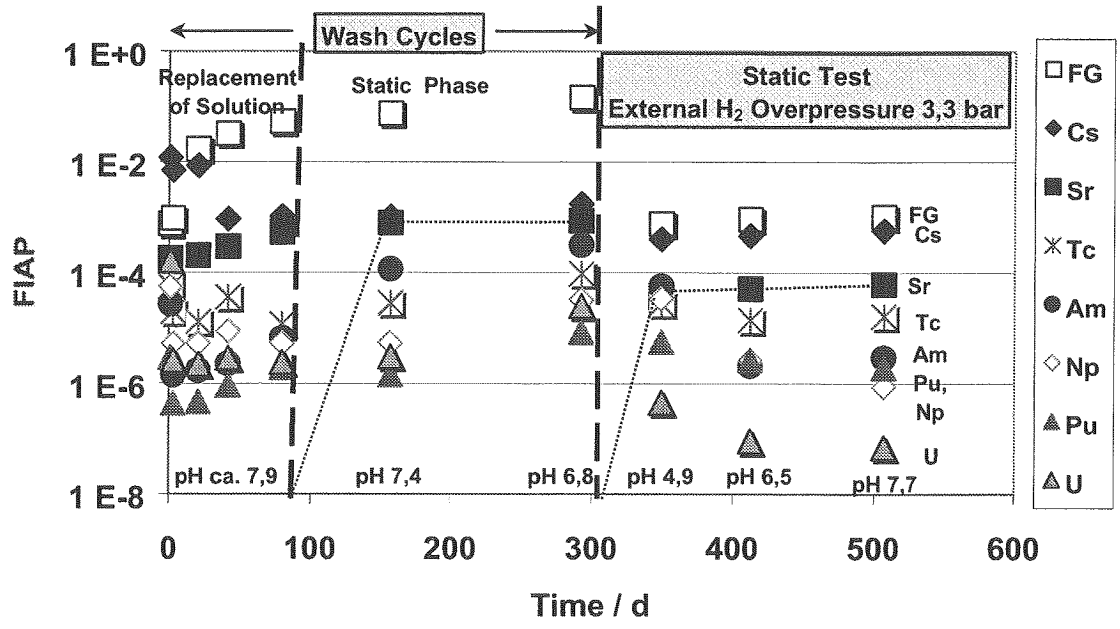

Figure 3. Effect of H_2 Overpressure on the Released Fractions of Radioelements and Fission Gas During the Corrosion of High Burnup Spent Fuel Pellet K8 in 5m NaCl solution.

the presence of H_2, matrix dissolution rates decrease and grain boundary contributions become more clearly measurable. The released fractions of other matrix bound radioelements as Tc, Np, Pu, U, Eu and Am were generally decreasing with time, hence release rates cannot be given for these elements. Their fractions in solution were still found on the same level as during the early wash cycles. The most pronounced decrease was observed for U, associated with FIAP values at least factor 10 less than found during the wash cycles ($FIAP_U$ $8{,}3x10^{-8}$, 117 days after start of the static test under H_2 overpressure).

The effect by an external H_2 overpressure on the solution concentrations of radioelements can be assessed from Fig. 4, where the concentrations of Cs, Sr, Eu, Am, Tc, Np, Pu and U are plotted as a function of pH. Included are data from the running test, using spent fuel pellet "K8" obtained during the static phase of the wash cycles (total contact time with solution 77 days) and solution data from somewhat less (53 days), and longer (117 days) contact times under H_2 overpressure. The concentrations of Cs were affected only to a small extent and the ones of Sr to a somewhat larger extent, when the H_2-overpressure was applied. They dropped from $9x10^{-7}$ to $4x10^{-7}$ M (Cs) and $3{,}5x10^{-7}$ to $2x10^{-8}$ M (Sr). These relatively high concentrations may be associated with the low pH value of 4.9, encountered during the first sampling interval 53 days after applying the H_2 overpressure to the system. When the pH climbed to 6.5 during the following 64 days both Cs and Sr concentrations remained at a constant level indicating corrosion rates close to zero. The concentrations of Tc and Pu were almost not affected, they were found to be around 10^{-8} M (Tc), or between $8x10^{-9}$ M and $2x10^{-9}$ M respectively (Pu). However, the concentrations of Eu, Am and U were found to be 1.7 or 1.3 orders of magnitude lower under H_2 overpressure. They were measured to be $1.3x10^{-10}$ M (Eu, Am) or $1x10^{-8}$ M (U).

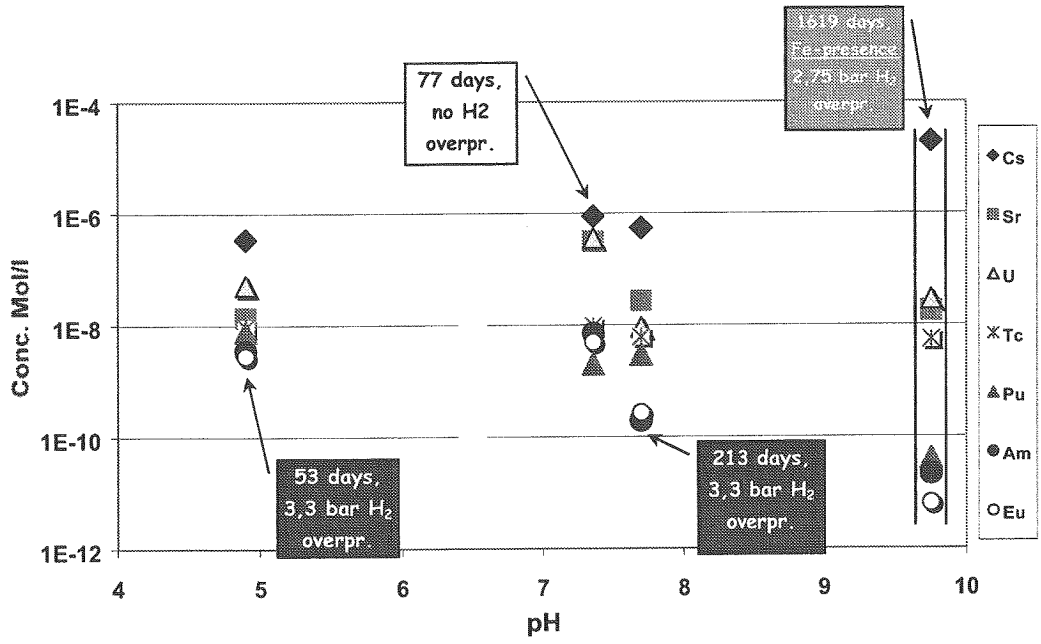

Figure 4. Effect of H_2 Overpressure on the Solution Concentrations During the Corrosion of High Burnup Spent Fuel Pellet K8 in 5m NaCl Solution

For comparison the solution concentrations from the co-dissolution test of spent fuel pellet ("K4" [2]) and metallic Fe powder, obtained after 1619 days are included in Fig. 4, where an internal H_2 overpressure of 2,75 bar due to the corrosion of the Fe powder was built up over the last sampling interval of 1049 days. Possibly its effect might be not exactly the same as an initially applied H2 overpressure of this magnitude. Similar solution concentrations as in the test with sample K8 were determined for U, Tc, and Np (generally very close to the detection limit). In contrast, solution concentrations of Eu, Am and Pu were found to be reduced at a factor of 16 or 100, respectively. This might be due to retention of these elements on the iron powder or its corrosion products, respectively. Cs concentration were found to be $2x10^{-5}$ M which might indicate that the release of Cs is still kinetically controlled by release mechanism from grain boundaries, once matrix dissolution rates become low, due to high H_2 pressures.
A decrease of several orders of magnitude of the matrix dissolution rate and solution concentrations of radioelements under the impact of an external H_2 overpressure was recently reported from a study related to the Swedish repository concept [5]. In contrast to our study a carbonated solution was used, Fe was present (stainless steel liner), and the H_2 overpressure was 50 bar, which does not allow a direct comparison of the results.

Conclusions

In the presence of a hydrogen overpressure of 3.3 bar, but in the absence of Fe, the extent of UO_2 matrix dissolution of pellet sized spent fuel in 5m NaCl solution in a carbonate free environment appears to be reduced at least roughly one order of magnitude during the first 117 days of the test. Due to constant or decreasing concentrations of Sr and other matrix bound radionuclides, corrosion rates were not measurable, indicating a stop of matrix dissolution or very low long-term rates. Grain boundary release of Cs and fission gases was found to continue under hydrogen pressure. Fractions released in solution were found to be reduced significantly for U, Eu and Am, whereas fractions of Tc, Pu, Np were less affected so far. In comparison to results from co-dissolution tests with spent fuel and Fe-powder, when a H_2 overpressure of 2.75 bar was built up solution concentrations were found to be similar for U, Tc, Np, but to be reduced strongly for Pu, Eu, Am, due to (co)precipitation, secondary phase formation, sorption on the solid surfaces in the system. Open questions remain on the long-term evolution of the system under study, with

respect to pH, Eh, the matrix dissolution rate and the associated release/retention of radionuclides, formation of secondary solid phases which makes it necessary to continue this experimental work aiming to take credit from the formation of a H_2 overpressure in repository safety considerations.

Acknowledgement

The authors like to express their thanks to the colleagues from FZK/INE, in particular Mrs. E. Bohnert and Dr. M. Kelm for analyzing the gas samples, Mrs. A. Görtzen, Mrs. C. Walschburger, Mr. F. Geyer and Mr.A.Seither for analysis of various leach solutions.

References

1. B.BONIN, A.COLIN, A.DUTFOY, "Pressure building during early stages of gas production in a radioactive waste repository", Journal of Nuclear Materials 281 (2000) 1-14
2. B.GRAMBOW, A. LOIDA, A. MARTINEZ-ESPARZA, P. DIAZ-AROCAS, J. DE PABLO, J.-L. PAUL,G.MARX, J.-P. GLATZ, K.LEMMENS, K. OLLILA, H. CHRISTENSEN, "Source term for performance assessment of spent fuel as a waste form", European Commission, Nuclear Science and Technology, EUR 19140 EN (2000)
3. B.GRAMBOW, A. LOIDA, P. DRESSLER, H. GECKEIS, J.GAGO, I. CASAS, I., J.DE PABLO, J. GIMENEZ, J., M.E..TORRERO, "Long-term safety of radioactive waste disposal: Chemical reaction of fabricated and high burnup spent fuel with saline brines", Forschungszentrum Karlsruhe, Wissenschaftliche Berichte FZKA 5702 (1996)
4. B. GRAMBOW, R.MÜLLER, Mater. Res. Soc. Symp.Proc. 176 (1990) 229
5. K.SPAHIU, L.WERME, U.EKLUND, "The influence of near field hydrogen on actinide solubilities and spent fuel leaching, Radiochim Acta, 88, 507-511 (2000)
6. M.KELM, personal communication (2000)
7. S.SUNDER, H.CHRISTENSEN, "Gamma Radiolysis of water solutions relevant to the nuclear fuel waste management program", Nucl. Technol., 104, 403, (1993)

Radiolyse und Korrosion von simulierten Brennstoffpellets in Chloridlauge

M.Kelm, E.Bohnert

Zusammenfassung
5 M NaCl Lösung wurde in Gegenwart von UO_2 Pellets mit α-Strahlen aus ^{238}Pu unter Luftausschluss bestrahlt. Dabei wurden zum einen ^{238}Pu dotierte Pellets verwendet, zum anderen wurde ^{238}Pu in der Lauge gelöst. Die gebildeten Radiolyseprodukte sowie die durch oxidative Auflösung des UO_2 mobilisierten Mengen U und Pu wurden bestimmt. Es zeigte sich, dass es bei gleicher Dosis sowohl für die Radiolyseprodukte als auch für die Oxidation/Auflösung der Pellets unerheblich ist, ob der α-Strahler praktisch homogen in der Lösung verteilt ist, oder ob die strahlenchemischen Prozesse nur in einer wenige 10 µm dicken Flüssigkeitsschicht nahe der Pellets ablaufen. Die Ausbeute an Radiolyseprodukten war mit der in früheren Arbeiten gefundenen vergleichbar. Die Ausbeute an oxidativ mobilisiertem U aus den Pellets betrug nur <1 % der insgesamt gebildeten oxidierenden Spezies. Der G-Wert für mobilisiertes 6-wertiges Uran betrug dementsprechend nur < 0,01 Moleküle / 100 eV.

Einführung
Im Hinblick auf eine Endlagerung von abgebranntem Kernbrennstoff in Salzformationen ist in der Vergangenheit die α- und γ-Radiolyse von konzentrierten Chloridlaugen untersucht worden (1, 2, 3 ,4). Die strahlenchemischen Prozesse in der Lösung konnten mit Hilfe eines reaktionskinetischen Rechenmodells (5, 2, 4) hinreichend simuliert werden.
Da die Mobilisierung von Radionukliden aus dem Brennstoff über die oxidative Auflösung der Matrix verläuft (6, 7, 8) und oxidierende Spezies in einem geologischen Endlager nur durch Radiolyse erzeugt werden, ist es von Interesse, welcher Anteil der oxidierenden Radiolyseprodukte zur Oxidation des Brennstoffs beiträgt. Durch dickwandige und/oder korrosionsfeste Behälter wird der abgebrannte Kernbrennstoff in einem Endlager für mindestens 500 Jahre vor Korrosion durch anstehende Wässer geschützt. Innerhalb dieses Zeitraums ist die Gammastrahlung so weit abgeklungen, dass nunmehr die Alphastrahlung der Aktinidenelemente überwiegt. Für Experimente zur Korrosion von 'altem' abgebrannten Kernbrennstoff eignen sich daher UO_2 Pellets, die mit einem kurzlebigen Alphastrahler dotiert sind. Bei der Verwendung von unbestrahltem UO_2 oder SIMFUEL (UO_2 mit Spaltprodukten in inaktiver Form) ist die Dosisleistung um Größenordnungen zu gering, bei echtem abgebranntem Brennstoff die β/γ- Dosisleistung zu hoch. In früheren Arbeiten ist schon vielfach mit $^{238}PuO_2$ dotiertem UO_2 experimentiert worden (9, 10, 11). Die untersuchten Systeme waren jedoch entweder verdünnte wässrige Lösungen (reines Wasser, Granitwasser u.ä.) oder aber luftgesättigt. Diese Arbeit beschreibt die experimentellen Ergebnisse der Korrosion von ^{238}Pu dotierten UO_2 Pellets in 5 M NaCl Lösung im Vergleich zur Korrosion von undotiertem UO_2 und von undotiertem UO_2 in ^{238}Pu-haltiger 5 M NaCl Lösung unter Luftausschluss. Zudem wird die strahlenchemische Ausbeute der verschiedenen Radiolyseprodukte verglichen. Durch die Dotierung der Pellets mit maximal 10% ^{238}Pu (Halbwertszeit 87,7 Jahre) ist deren α-Aktivitätskonzentration und damit auch deren Dosisleistung bis zu 250 mal höher als die von 500 Jahre altem abgebrannten Kernbrennstoff.

Experimente
Alle Experimente wurden in einer Inertgasbox durchgeführt. Die Pellets von ca. 6 mm Durchmesser bzw. Kantenlänge und 0,3 bis 0,8 g Masse wurden - nachdem sie geschnitten, poliert und gereinigt waren- unmittelbar vor Versuchsbeginn für mehrere Stunden in einem Ar/H_2 Strom bei 1400 °C geglüht, um auch an der Oberfläche eine stöchiometrische Zusammensetzung entsprechend UO_2 zu erzielen. Das Glühverfahren wurde durch ESCA

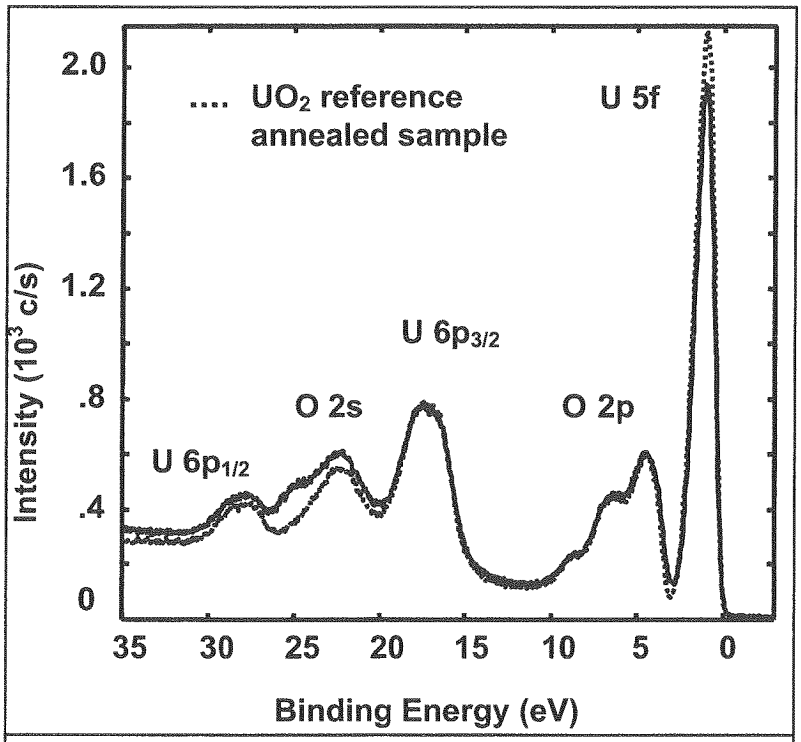

Abb.1: ESCA - Spektrum einer UO_2 Probe nach dem Glühen im Ar/H_2 Strom bei 1400°C im Vergleich zu einer im Ultrahochvakuum gebrochenen Probe.

Analyse an einem undotierten Pellet überprüft. Die Auswertung der U 5f Linie im ESCA Valenzbandspektrum zeigt (Abb.1), dass die Pelletoberfläche zu 92% der Zusammensetzung UO_2 entspricht (bzw. die mittlere Zusammensetzung $UO_{2,08}$ hat). Die nominale Pelletzusammensetzung und die Aktivitätskonzentrationen der Salzlösung zeigt Tab.1, die tatsächliche Zusammensetzung des für die Dotierung der Pellets und für die Herstellung der Lösung verwendeten Plutoniums die Tab. 2. Nach dem Erkalten wurden die Pellets in ein Glasgefäss mit Siebboden überführt und 20 ml mit Ar begaste Lösung nach Tab. 2 zugegeben. Auf das Gefäss wurde eine evakuierte Gasmaus gasdicht aufgeschraubt und das Ventil zur Gasmaus geöffnet. Dadurch wurde im Gefäss ein Unterdruck eingestellt. Der Probenahmezeitpunkt wurde so gewählt, dass trotz Radiolysegasentwicklung der Druck im Gefäß immer unterhalb des

No.	UO_2-pellet: $^{238}PuO_2$ nom. wt.%	5 M NaCl sol.: act. conc. GBq/L	pH at start
1	10	0	12
2	10	0	8
3	0.1	0	8
4	0	8.41	12
5	0	8.41	8
6	0	841	8
7	0	0	8

Tab.1 : Zusammensetzung der Pellets und der Lösungen. Die Matrix der Pellets 1, 2 und 3 ist abgereichertes Uran (0,32 % ^{235}U), die der übrigen Pellets natürliches Uran (0,72% ^{235}U)

Nuclide	Used for pellets %	Used for solution %
^{238}Pu	66.7	64.0
^{239}Pu	17.9	15.3
^{240}Pu	3.0	2.5
^{241}Pu	0.1	0.3
^{242}Pu	0.1	0.4
^{234}U	12.1	16.4
^{241}Am	0.1	0.9
^{238}U	0	0.2

Tab.2: Nuklidzusammensetzung des für die Dotierung der Pellets bzw. für die Lösung verwendeten PuO_2.

Atmosphärendrucks blieb. Die Lösung wurde bei Umgebungstemperatur gehalten und im Abstand von einigen Stunden jeweils für 10 Minuten gerührt. Zur Probenahme wurde die Gasmaus geschlossen und abgekoppelt; die Gaszusammensetzung wurde massenspektrometrisch untersucht, die Gesamtmenge Radiolysegas (H_2 und O_2) aus dem gemessenen Gasdruck bestimmt. Von der Lösung wurden einige ml entnommen und die Radiolyseprodukte HClO, ClO_2^- und ClO_3^- sowie pH und Eh bestimmt (siehe (1)). Der Gasraum über der Lösung wurde mit Inertgas aus der Boxenatmosphäre gespült, eine neue Gasmaus aufgesetzt und das Korrosionsexperiment fortgesetzt. Im ersten Versuchsabschnitt (ca. 8 Monate, max.3 Probenahmen) wurde jeweils ein Teil der Flüssigprobe durch ein 450nm

und ein 1,8 nm Filter filtriert. Im Filtrat wurde der U- und Pu Gehalt massenspektrometrisch (ICP-MS für Massenbereich 234 - 242) aus geeigneten Isotopen bestimmt. Für die Pu Messung wurde zusätzlich die α-Aktivitätsmessung herangezogen. Diese Art der Probenaufbereitung erlaubt eine Aussage über den Gehalt an echt gelöstem U und Pu sowie über die Partikelgrösse der aus den Pellets mobilisierten und in der Lösung verteilten Stoffe. Im zweiten Versuchsabschnitt wurde auf diese Differenzierung verzichtet; die Lösungsaliquote wurden sofort mit HNO_3 angesäuert, so dass die U- und Pu-Analysen die Gesamtmenge dieser Elemente in der Lösung ergeben. Für die Zukunft ist ein weiterer Wechsel des Probenahmeregimes geplant: Wenn durch die Probenahmen die Lösung praktisch verbraucht ist, wird dann jeweils die gesamte Lösung ausgetauscht. Dadurch werden möglicherweise Übersättigung und Abscheidung von Sekundärphasen unterdrückt.

Ergebnisse

Die meisten Ergebnisse werden als Lösungskonzentration (bei den Radiolysegasen die pro kg Lösungsmittel entwickelte Molzahl) in Abhängigkeit von der α-Dosis dargestellt. Dabei wird angenommen, dass bei den Pellets 1, 2 und 3 (Tab.1) nur 18,8 % des in einer oberflächennahen Schicht der Pellets von 11,8 µm Dicke vorhandenen ^{238}Pu strahlenchemisch wirksam ist, die Dosis sich aber auf das gesamte Flüssigkeitsvolumen verteilt. Dies berücksichtigt lediglich geometrische Überlegungen für den Austritt von α-Strahlen aus dem UO_2, nicht aber den energieabhängigen Energietransfer längs eines α-tracks. Bei einem konstanten Wert für den linearen Energietransfer sind Kugelabschnitte, integriert über den Kugelradius dividiert durch das Kugelvolumen ein Maß (M) für die aus einer ebenen Fläche eines Alphastrahlers austretende Strahlenenergie, wenn der betrachtete Radius der Reichweite r der Alphastrahlung im UO_2 entspricht:

$$M := \frac{\int_0^r \frac{1}{3}\cdot\pi\cdot(r-x)^2\cdot(2\cdot r+x)\,dx}{\frac{4}{3}\cdot\pi\cdot r^4} \qquad M = 0.188$$

Die Ableitung in (12) für CANDU Brennstoff ergibt einen noch etwas geringeren Wert für die austretende Strahlenenergie.

Für die Pellets 1 und 2 ergibt sich daraus eine Dosisleistung zwischen 10 und 35 Gy/h (wegen der durch Probenahme verringerten Lösungsmenge steigend), für Pellet 3 eine Dosisleistung von 0,1 bis 0,17 Gy/h. Die mittlere Dosisleistung in der der Pelletoberfläche benachbarten und von den α-Strahlen tatsächlich getroffenen Lösungsschicht von ca. 48 µm Dicke ist um weit mehr als 3 Größenordnungen höher. Bei den Pellets 4, 5 und 6 wird angenommen, dass das in der Lösung vorhandene Plutonium beim Zerfall alle Energie

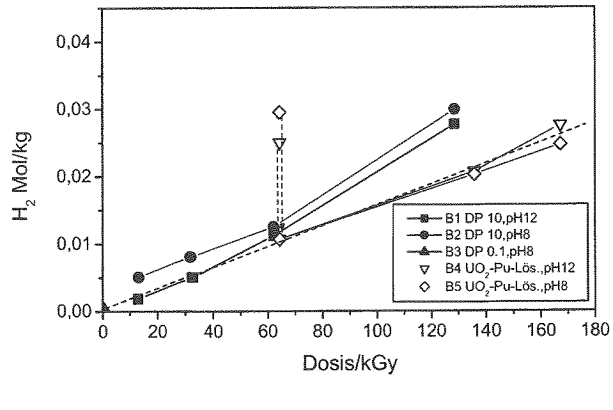

Abb.2: Wasserstoffbildung in 5 M Chloridlösung in Kontakt mit Pu-dotierten Pellets (B1, B2, B3) im Vergleich zur Bildung in Laugen mit gelöstem Pu in Gegenwart von UO_2 Pellets (B4, B5). Die gestrichelte Gerade entspricht der Bildungsrate in Pu-haltiger 5 M Chloridlösung (siehe (4)). Die ersten Messungen der Proben B4 und B5 bei ca. 65 kGy sind offenbar fehlerhaft; für die Berechnung der Gasbildung bei höherer Dosis wurden diese Meßwerte auf den Erwartungswert (gestrichelte Kurve) reduziert.

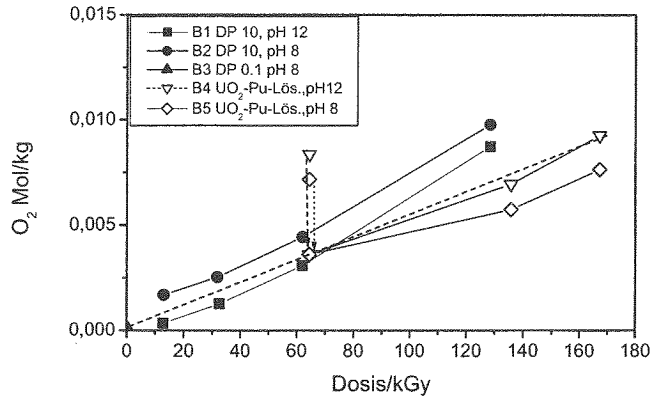

Abb.3: Sauerstoffbildung in 5 M Chloridlösung in Kontakt mit Pu-dotierten Pellets (B1, B2, B3) im Vergleich zur Bildung in Laugen mit gelöstem Pu in Gegenwart von UO_2 Pellets (B4, B5). Die gestrichelte Gerade entspricht der Bildungsrate in Pu-haltiger 5 M Chloridlösung (siehe (4)). Die ersten Messungen der Proben B4 und B5 bei ca. 65 kGy sind offenbar fehlerhaft; für die Berechnung der Gasbildung bei höherer Dosis wurden diese Meßwerte auf den Erwartungswert (gestrichelte Kurve) reduziert

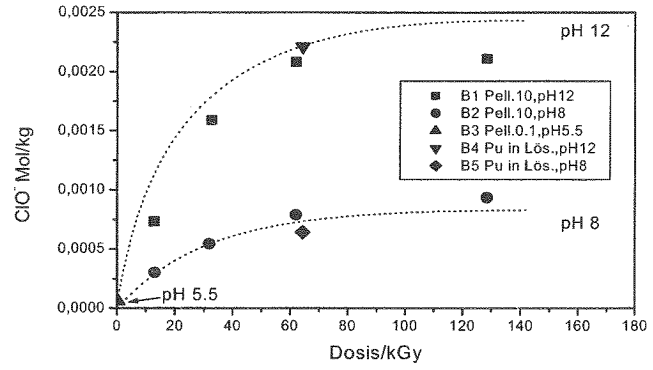

Abb.4: Hypochloritbildung in 5 M Chloridlösung in Kontakt mit Pu-dotierten Pellets (B1, B2, B3) im Vergleich zur Bildung in Laugen mit gelöstem Pu in Gegenwart von UO_2 Pellets (B4, B5).

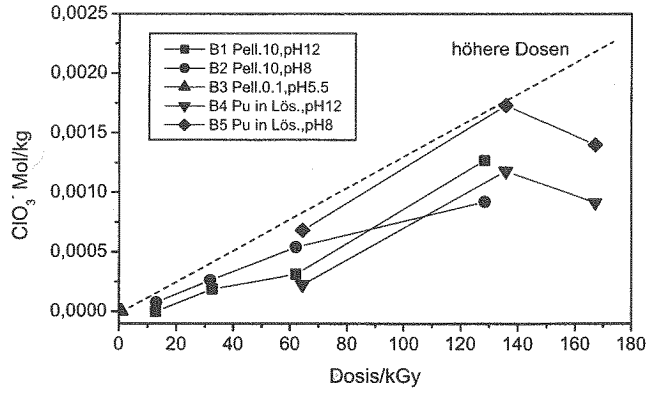

Abb.5: Chloratbildung in 5 M Chloridlösung in Kontakt mit Pu-dotierten Pellets (B1, B2, B3) im Vergleich zur Bildung in Laugen mit gelöstem Pu in Gegenwart von UO_2 Pellets (B4, B5). Die gestrichelte Gerade entspricht der Bildungsrate in Pu-haltiger 5 M Chloridlösung bei hoher Dosis (siehe (4)).

gleichmäßig auf die Lösung überträgt. Daraus ergeben sich für die Pellets 4 und 5 eine Dosisleitung von 22,5 Gy/h und für Pellet 6 eine Dosisleistung von 2250 Gy/h. Die Dosisleistung durch UO_2 in Pu-freier Lösung (Pellet 7) ist vernachlässigbar klein (ca. 4 Größenordnungen kleiner als bei Pellet 3).

Die Abb. 2 und 3 zeigen die Radiolysegasbildung. Aus ihnen geht hervor, dass sowohl Wasserstoff als auch Sauerstoff proportional zur Dosis gebildet werden und dass die Bildungsrate mit früheren Messungen (4) gut übereinstimmt. Die Radiolysegasbildung ist praktisch unabhängig vom pH und von der Verteilung des α-Strahlers in der Lösung und damit der lokalen Dosisleistung. Die Bestrahlung mit dotierten Pellets, bei der die strahlenchemischen Primärprodukte in einem Flüssigkeitsvolumen von ca. 4 mm^3 gebildet werden, führt bei gleicher Dosis zu einer vergleichbaren Gasbildung wie die Bestrahlung mit praktisch homogen in 20 ml Lösung verteiltem Plutonium. Außer den Gasen werden als weitere Radiolyseprodukte in Chloridlaugen Hypochlorit (Abb.4), Chlorit und Chlorat (Abb.5) gebildet. Bei allen Experimenten wurden Chloritkonzentrationen von maximal einigen 10^{-5} Mol/kg gemessen. Die Hypochloritbildung steigt mit steigendem pH und führt zu Gleichgewichtskonzentrationen, während Chlorat proportional zur Dosis gebildet wird. Die Chloratkonzentrationen bleiben aber alle unterhalb der auf Grund früherer Messungen (4) zu erwartenden Werte.

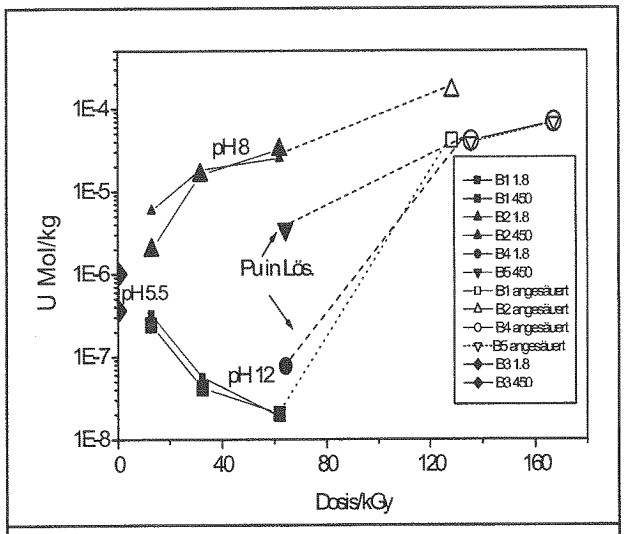

Abb.6: In 5 M NaCl Lösung aus UO_2 Pellets mobilisiertes U (B1, B2, B3: Pellets enthalten Pu; B4, B5: Lösung enthält gelöstes Pu). Geschlossene Symbole: U-Konzentration im Filtrat der Probe (1,8 bzw. 450 nm). Offene Symbole U-Konzentration in angesäuerter Probe.

Neben den Radiolyseprodukten wurden in den Auslauglösungen auch die Uran- und in den Lösungen mit dotierten Pellets auch die Plutoniumkonzentration bestimmt. Wie Abb. 6 und 7 zeigen, ergeben sich für die Versuchsphase, in der die Proben über ein 450 nm und ein 1,8 nm Filter filtriert wurden, bei den mit 10% ^{238}Pu dotierten Pellets und pH 12 gegenüber denen bei pH 8 viel geringere Konzentrationen. Mit zunehmender Versuchszeit werden die Unterschiede zwischen beiden Filtraten vernachlässigbar. Dies bedeutet, dass sowohl U als auch Pu grobe Niederschläge gebildet haben, die von beiden Filtern zurückgehalten werden. Bei den dotierten Pellets in alkalischem Medium liegt die U Konzentration drei, die Pu Konzentration etwa zwei Größenordnungen unter der bei pH 8. Die pH bedingten Unterschiede für die Löslichkeit des U aus UO_2 Pellets in Pu-haltiger Lösung (Lsg. 4 und 5 in Tab. 1) sind etwas geringer ausgeprägt (zwei Größenordnungen). Korrosionslösungen, die unmittelbar nach der Probenahme angesäuert wurden, zeigen bei einer Bestrahlungsdosis von etwa 150 kGy unabhängig vom pH, bei dem das Experiment durchgeführt wurde und unabhängig von der Verteilung des Alphastrahlers (dotierte Pellets oder homogene Verteilung des α-Strahlers in der Lösung) eine U-Konzentration von einigen 10^{-5} Mol/kg und eine Pu-Konzentration von wenigen 10^{-6} Mol/kg. Beim Experiment 7 (Tab.1) ohne Strahlenquelle wurden erwartungsgemäß keine Radiolyseprodukte gemessen. Die U-Konzentration in der Lösung betrug bei den Probenahmen innerhalb der ersten 9 Monate zwischen 10^{-9} und 10^{-8} Mol/kg.

Der pH der Lösungen 1, 2, 4, 5 und 6 (Tab.1) änderte sich während des Experiments kaum. In den alkalischen Lösungen 1 und 4 stellte sich ein Redoxpotential von ca. +650 mV ein. In den neutralen Lösungen 2 und 5 erreichte das Redoxpotential einen Wert von über 950 mV; in

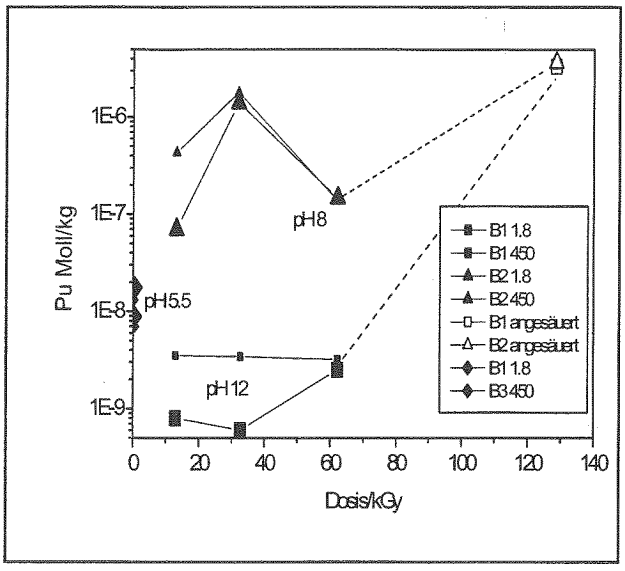

Abb.7: In 5 M NaCl Lösung aus Pu-haltigen UO_2 Pellets mobilisiertes Pu. Geschlossene Symbole: Pu-Konzentration im Filtrat der Probe (1,8 bzw. 450 nm). Offene Symbole Pu-Konzentration in angesäuerter Probe.

Lösung 6 mit einer sehr hohen Plutoniumkonzentration wurden über 1000 mV gemessen. Der pH der Lösungen 3 (Pellet mit 0,1 % ^{238}Pu) und 7 (UO_2 Pellet ohne Pu) verschob sich im Versuchszeitraum leicht in den sauren Bereich (pH 5,5 bzw. 6,5), das Redoxpotential erreichte Werte von 440 mV (Lösung 3, Tab.1) bzw. 530 mV (Lösung 4, Tab1).

Das Experiment 6 (UO_2 Pellet in Lösung mit 841 GBq/L ^{238}Pu) wurde nach 4800 h beendet. Die Bestrahlungsdosis betrug zu diesem Zeitpunkt etwa 10,8 MGy. Das Pellet wurde mit Wasser gespült, getrocknet und dann im Rasterelektronenmikroskop untersucht. Abb. 8 zeigt die Oberfläche im Vergleich zu einem unkorrodierten Pellet. Es ist noch unklar, ob nur die Rauigkeit zugenommen hat oder ob es sich um Abscheidungen von Sekundärphasen handelt.

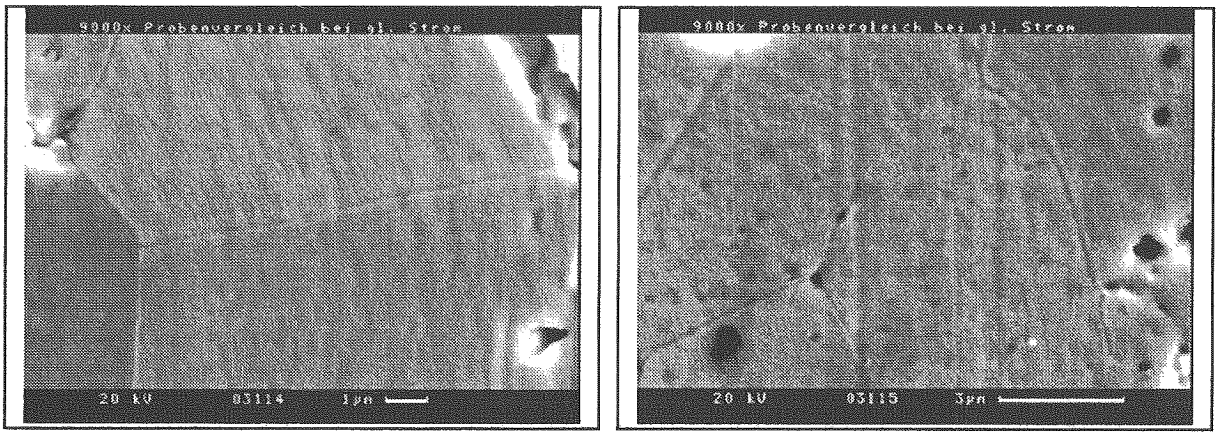

Abb.8: Oberfläche (SEM) eines UO_2 Pellets vor (links) und nach (rechts) der Korrosion in Pu-haltiger 5M NaCl Lösung (4800 h, 10,8 MGy)

Diskussion

Die Ergebnisse hinsichtlich der Bildung der Radiolyseprodukte H_2 und O_2 stimmen mit denen aus früheren Arbeiten zur α-Radiolyse von Chloridlaugen (4) gut überein. Die Gegenwart von UO_2 Pellets bzw. die Bestrahlung allein durch ^{238}Pu-dotierte Pellets hat keinen messbaren Einfluss auf die Ausbeute. Qualitativ lässt sich auch der Konzentrationsverlauf der drei Chlorspezies HClO, ClO_2^- und ClO_3^- an Hand des in (2) und (4) beschriebenen Reaktionsmodells verstehen. Danach wird Chlorat auf drei Wegen gebildet: Sehr schnell durch Abreaktion strahlenchemisch gebildeter kurzlebiger Zwischenprodukte und langsamer durch die Reaktion von Chlorit mit im Überschuss gebildetem Hypochlorit. Der Überschuss Hypochlorit reagiert im Laufe von Monaten zu Chlorat. Daraus erklärt sich die permanent niedrige Chloritkonzentration und die Begrenzung der Hypochloritkonzentration auf einen Plateauwert. Wegen des Hypochloritaufbaus werden bei niedrigen Bestrahlungsdosen

Chloratkonzentrationen gemessen, die unterhalb der für hohe Dosen erwarteten Werte liegen. Erst bei hohen Dosen (hoher Dosisleistung und/oder lange Zeit) ist der noch nicht zu Chlorat umgesetzte Anteil Hypochlorit zu vernachlässigen. Auch für die Ausbeute der wasserlöslichen Radiolyseprodukte ist es unerheblich, ob die Primärprodukte praktisch homogen in der Lösung oder nur in unmittelbarer Nähe der Pelletoberfläche gebildet werden. Bei den Experimenten mit niedriger Dosisleistung (3 und 7, Tab.1) war die absolute Ausbeute an Radiolyseprodukten so gering, dass die Konzentrationen für alle Radiolyseprodukte an der Nachweisgrenze lagen.

Durch oxidative Korrosion wird von den eingesetzten Pellets Pu und/oder U mobilisiert. Abb. 6 zeigt, dass in den filtrierten alkalischen Lösungen nur einige 10^{-8} Mol/kg Uran gelöst sind, während in den neutralen Lösungen um mehrere Größenordnungen höhere Urankonzentrationen gemessen wurden. Die Filtration durch 450 nm und 1,8 nm Filter ergab praktisch keine Unterschiede der Urankonzentration im Filtrat. Entsprechend den in (13) publizierten Löslichkeitsdaten für 6-wertiges Uran in 5 M NaCl Lösung wird bei pH 8 und bei Extrapolation der Daten auch bei pH 12 die Urankonzentration in den filtrierten Korrosionslösungen durch die Löslichkeit des orangenen Uranats kontrolliert. Das mobilisierte, aber nicht echt gelöste Uran wird vom 450 nm und vom 1,8 nm Filter gleichermaßen abgeschieden; die Partikelgröße muss entsprechend hoch sein. Werden die Korrosionslösungen unmittelbar nach der Probenahme angesäuert, beträgt die Urankonzentration in den Lösungen bei einer Dosis von ca.150 kGy im Mittel fast 10^{-4} Mol/kg, unabhängig ob mit dotierten Pellets oder in praktisch homogener Lösung bestrahlt wurde. Im Experiment mit Pellet 3 (Tab.1), dotiert mit 0,1 % PuO_2 wurde bei einer entsprechend niedrigeren Dosis von 1 kGy eine Urankonzentration von etwa 10^{-6} Mol/kg gemessen; diese Konzentration ist nicht löslichkeitskontrolliert.

Das zusammen mit Uran aus den dotierten Pellets mobilisierte Plutonium verhält sich ähnlich wie Uran. Nach längerer Versuchsdauer werden in den filtrierten Korrosionslösungen von Pellet 1 und 2 (Tab.1) unabhängig von der Filterweite Konzentrationen von einigen 10^{-9} Mol/kg (pH 12) bzw. einigen 10^{-7} Mol/kg (pH 8) gemessen. Im alkalischen Bereich entspricht dies einer Löslichkeitsbegrenzung für 6-wertiges Pu, wie sie Pashalidis (14) berechnet und gemessen hat. Bei pH 8 liegt die gemessene Pu-Konzentration zwischen der Pu-Löslichkeitskurve bei Hydrolyse und Chloridkomplexierung und der bei Hypochloritkomplexierung. Allerdings gelten die Daten für die Hypochloritkomplexierung in (14) für eine etwa 5-fach höhere Aktivitäts- und damit auch für eine höhere Hypochloritkonzentration und einen dementsprechend höheren Komplexierungsgrad. Wird die Korrosionslösung unmittelbar nach der Probenahme angesäuert, wird nach einer Dosis von etwa 150 kGy eine Pu-Konzentration von einigen 10^{-6} Mol/kg gemessen, unabhängig vom pH. Das Experiment 3 (Tab.1) mit einem Pellet mit 0,1% PuO_2 ergab nach gleich langer Versuchszeit und einer Dosis von 1 kGy eine Pu-Konzentration von etwa 10^{-8} Mol/kg, die offenbar nicht löslichkeitskontrolliert ist.

Geht man bei den Experimenten mit dotierten Pellets davon aus, dass die in den angesäuerten Lösungen gemessenen Konzentration von U und Pu die insgesamt mobilisierte Menge repräsentieren, also keine gravierende Abscheidung von U- und Pu- Verbindungen auf den Gefäßwänden u.ä. stattfindet und dass die Auflösung kongruent und proportional zur Dosis erfolgt, müssten sich die Konzentrationsverhältnisse von U und Pu zu einem beliebigen Zeitpunkt aus der Dotierung ergeben. Einen entsprechenden Vergleich zwischen erwarteten und tatsächlich gemessenen Konzentrationen zeigt Tab.3. Daraus geht hervor, dass die Konzentrationen in den Korrosionslösungen tatsächlich annähernd kongruente Auflösung von U und Pu sowie eine Dosisproportionalität der Auflösung zeigen. Die in Experiment 7 (Tab.1) ohne Strahlenquelle gemessene U-Konzentration in der Korrosionslösung von 10^{-8} bis 10^{-9} M zeigt möglicherweise den Übergang zu nicht-oxidativer Auflösung des UO_2 an ((6), (7)), möglicherweise ist es aber auch der Effekt nicht vermeidbarer Luftkontamination in der

PuO_2 - Content (%)	Expected conc. (Mol/L)		Measured conc. (Mol/L)	
	U	Pu	U	Pu
10	10^{-4}	10^{-5}	10^{-4}	$3 \cdot 10^{-6}$
0,1	10^{-6}	10^{-9}	10^{-6}	$5 \cdot 10^{-9}$

Tab. 3: Gemessene und erwartete U- und Pu-Konzentrationen in der Korrosionslösung nach etwa 9 Monaten. Die Erwartungswerte wurden unter der Annahme berechnet, dass die Lösungskonzentrationen für U und Pu proportional der jeweiligen Konzentration im Pellet und der Aktivitätskonzentration ist. Für die Berechnung wurde als Referenz die Urankonzentration (10^{-4} M) aus dem Experiment mit dem 10%igen Pellet benutzt.

Handschuhbox in Höhe einiger ppm Sauerstoff und damit nach wie vor Resultat oxidativer Auflösung.

Betrachtet man die strahlenchemische Ausbeute für die Oxidation und Auflösung von UO_2, so kommt man bei Verwendung der in den angesäuerten Proben gefundenen U- und Pu - Konzentrationen zu Werten unter 1% der insgesamt gebildeten oxidierenden Spezies. Der G-Wert für gelöstes Uran beträgt dementsprechend nur weniger als 0,01 Moleküle U^{6+}/100 eV.

Die mittlere Korrosionsrate der Pellets 1, 2, 4 und 5 (Tab.1) nach rund 7400 h und einer auf die gesamte Lösung bezogenen Dosis von etwa 150 kGy beträgt 1,7 µg/(cm^2*d). Bei Versuchsende enthielt die Korrosionslösung rund 10^{-3} M Hypochlorit, 10^{-3} M Chlorat und 3.10^{-6} M Sauerstoff als potentiell oxidierende, radiolytisch gebildete Substanzen. Die gefundenen Korrosionsraten erscheinen hoch, wenn man sie mit Korrosionsraten von UO_2 in 0,1 M $NaClO_4$ Lösung vergleicht (6). Für eine Korrosionsrate von 1,7 µg/(cm^2*d) ist eine H_2O_2 oder O_2 Konzentration von etwa 0,1 M erforderlich. Etwa derselbe Wert gilt für die Hypochloritkonzenration (15). Ein direkter Vergleich mit α-radiolytisch bedingter Korrosion von UO_2 in 0,1 M $NaClO_4$ Lösung ist schwierig, da Sunder et al. (16) einen direkten Zusammenhang zwischen Dosisleistung und Korrosionsrate herstellen, der aber nur gegeben ist, wenn alle gebildeten oxidierenden Spezies zur Korrosion von UO_2 führen, oder aber die nicht umgesetzten Spezies den Reaktionspool verlassen. Berechnet man für die in (16) angegebene Bestrahlungsgeometrie, einer Dosisleistung von 1000 Gy/h und einer strahlenchemischen Ausbeute für H_2O_2 von G = 1 Molekül/100 eV die mögliche UO_2 Korrosionsrate, so beträgt sie 2 µg/(cm^2*d). Die tatsächlich beobachtete Korrosionsrate (16) liegt aber nur bei maximal 10^{-3} µg/(cm^2*d). Die strahlenchemische Ausbeute für die Korrosion beträgt also weniger als 0,1 %. Dies ist mit den im Chloridsystem gefundenen Ausbeuten für die UO_2 Korrosion vergleichbar.

Für das Experiment ohne α-Strahler (Pellet 7, Tab. 1) wird über einen Zeitraum von 7500 h im Mittel eine Korrosionsrate von $2{,}7 \cdot 10^{-4}$ µg/(cm^2*d) gefunden. Dieser Wert stimmt gut mit dem in (6) angegebenen Mittelwert von $2 \cdot 10^{-4}$ µg/(cm^2*d) für 0,1 M NaClO4 Lösung überein. Zusammenfassend lässt sich sagen, dass die UO_2 Korrosion ohne Strahlung in Salzlauge und wässriger Lösung zu ähnlichen Auflöseraten führt. Die durch α-Strahlung unterhaltene oxidative Auflösung von UO_2 in Salzlauge führt zu einer Rate, die höher ist, als durch wasserlöslichen Radiolyseprodukte zu erwarten. Die strahlenchemische Ausbeute für die UO_2 Korrosion ist in Salzlauge und wässriger Lösung gleichermaßen gering und liegt bei unter 1 % der insgesamt radiolytisch gebildeten oxidierenden Produkte.

Danksagung

Die Autoren danken insbesondere Dr. V. Rondinella (TUI) für die Überlassung der plutoniumdotierten Pellets, Frau A. Görtzen für die LSC-Messungen, Herrn N. Kerner für die Ionenchromatographie, Dr. J. Römer, Dr. D. Schild, Frau E. Soballa und Herrn K. Spieler für die Festkörperanalytik, sowie Frau C. Walschburger für die ICP-MS Messungen.

Literatur

1. Kelm, M. and Bohnert, E.: Radiation chemical effects in the near field of final disposal site. Part 1: Radiolytical products formed in concentrated NaCl solutions, Nucl. Technol., 129, 119-122 (2000)

2. Kelm, M. and Bohnert, E.: Radiation chemical effects in the near field of final disposal site. Part 2: Simulation of the radiolytic processes in concentrated NaCl solutions, Nucl. Technol., 129, 123-130, (2000)
3. Kelm, M., Pashalidis, I. and Kim, J., I.,: Spectroscopic investigation on the formation of hypochlorite by alpha radiolysis in concentrated NaCl solutions. Appl.Radiat.Isot. 51, 637-642 (1999)
4. Kelm, M., Bohnert, E., Pashalidis, I.; Products formed from alpha radiolysis of chloride brines, Res.Chem.Intermed., 27, No 4,5, 503 - 507 (2001)
5. Carver, M.B., Hanly, D.V., Chaplin, K.R.,1986/87. MACKSIMA-CHEMIST, Mass Action Chemical Kinetics Simulation; Automatic Chemical Equation Manipulation and Integration using stiff, sparse Techniques.1978/79. Revised by Paquette, J. .Atomic Energy of Canada Ltd., AECL 6413
6. Shoesmith, D., W., Sunder, S., The prediction of nuclear fuel (UO_2) dissolution rates under waste disposal conditions, J.Nucl.Mater. 190, 20-35 (1992)
7. Sunder, S, Shoesmith, D., W., Chemistry of UO_2 fuel dissolution in relation to the disposal of used nuclear fuel. AECL - 10395 (1991)
8. Shoesmith, D., W., Fuel corrosion processes under waste disposal conditions, J.Nucl.Mater. 282 (2000) 1-31
9. Rondinella, V.,V., Matzke, Hj., Cobos, J., Wiss, T., α-Radiolysis and α-radiation damage essects on UO2 dissolution under spent fuel storage conditions, Mat.Res.Soc.Symp.Proc. 556 (1999) 447-454
10. Rondinella, V.,V., Matzke, Hj., Cobos, J., Wiss, T., Leaching behaviour of UO_2 containing α-emitting actinides, Radiochim.Acta, 88, 527-531 (2000)
11. Gray, W., J., Comparison of Uranium release from spent fuel and unirradiated UO_2 in salt brine, Mat. Res.Soc.Symp.Proc. 84 (1987) 141-152
12. Garisto, F., The energy spectrum of α-particles emitted from used CANDU^{TM} fuel, Ann.Nucl.Energy 16 No1, 33-38 (1989)
13. Diaz Arocas, P., Grambow, B., Solid-liquid phase equilibria of U(VI) in NaCl solutions, Geochim.Cosmochim.Acta, 62, No2, 245-263 (1998)
14. Pashalidis, I., Kim, J., I.,Untersuchung der Übertragbarkeit von Labordaten auf natürliche Verhältnisse. Chemisches Verhalten des sechswertigen Plutoniums in konzentrierten NaCl- Lösungen unter dem Einfluß der eigenen Alpha-Strahlung. RCM 01092 (1992)
15. Grambow, B., Loida, A., Dressler, P., Geckeis, H., Gago, J., Casas, I., de Pablo, J., Giminez, J., Torrero, M.E., Chemical Reaction of Fabricated and High Burnup Spent UO_2 Fuel with Saline Brines, FZKA 5702 (1996)
16. Sunder, S:, Shoesmith, D., W., Miller, N., H., Oxidation and dissolution of nuclear fuel (UO2) by the products of the alpha radiolysis of water, J.Nucl.Mater. 244(1997) 66-74

Assessment of the Technical Barrier Disposal Container

E. Smailos, B. Fiehn, R. Weiler

1. Introduction

The aim of the project is the determination of materials for long-lived HLW/Spent Fuel disposal containers, and the quantification of the effectiveness of such containers (overpacks) as a barrier against a mobilization of radionuclides from the waste forms by attack of brines. This requires detailed knowledges of the long-term corrosion behaviour of the container materials under realistic disposal conditions and of the retention of leached radionuclides on container corrosion products.

An important aspect of the corrosion studies is the investigation of the long-term corrosion behaviour of preselected container materials under conditions prevailing in the normal operating phase of a rock-salt repository. For this, in-situ corrosion experiments (field experiments) are performed in the Asse salt mine. In the present work, results are reported which have been obtained from a more than ten years in-situ corrosion experiment on preselected metallic materials for containers (overpacks) and canisters (for accomodation of vitrified HLW). The experiment was performed in the framework of the EU-Project BAMBUS II (Backfill and Material Behaviour in Underground Salt Repositories) [1].

2. Investigation of the in-situ corrosion behaviour of preselected container and canister materials for HLW/Spent fuel

Experimental and results

The materials investigated were:

- Container materials: Ti99.8-Pd, Hastelloy C4 and Hastelloy C22 (Ni-base alloys), TStE355 carbon steel and 15MnNi6.3 low-alloyed steel.
- Shielding container materials: TStE460 low-alloyed steel and cast iron.
- Canister materials: Cr-Ni steels 1.4306 and 1.4833.

In addition pure Nickel (99.99 wt.%) was examined for comparison reasons.

All materials were examined in the hot-rolled condition. Besides unwelded specimens, TIG-welded (Tungsten Inert Gas welded), EB-welded (Electron Beam welded) and SAW-welded (Submerged Arc welded) specimens simulating potential container closure techniques were investigated. The corrosion testing of the materials was performed in the Underground Research Laboratory of the Asse salt mine in a backfilled drift of the test field of the TSDE experiment (Thermal Simulation of Drift Emplacement) [1]. In this experimental Drift, three electrically heated casks simulating the POLLUX spent fuel disposal containers [2] were installed. Figure 1 shows a general view of the TSDE test field. The specimens (40 mm × 20 mm × 3 mm) were located on the central heater cask and in the backfill (crushed rock salt) at the drift floor near the drift wall. The average temperature on the central heater cask was 180°C, whereby for short-time the maximum temperature reached 210°C. The average temperature at the drift wall was 90°C. The heating phase lasted about 8.2 years and the cooling phase 1.2 years. The whole storage time of the specimens (from start of heating up to the recovery of the specimens) was about 10.2 years.

The chemical conditions near the corrosion specimens are described in detail in [3]. According to this, during the experiment the specimens were in contact with compacted backfill and were exposed to gases such as H_2, CH_4 and CO_2. H_2 was generated by corrosion of the steel heater casks, CH_4 and CO_2 were released from the backfill due to thermal desorption and thermal decomposition of salt minerals. The gas generation in the test field was moderate. Furthermore, according to measurements of [3] water was released from crystal surfaces and from hydrated minor minerals of rock salt. After the start of heating, the humidity of the air increased considerably due to dehydradation of backfill and rock salt. A total water content of 0.0003-0.0004% was estimated for the heated backfill after eight years of heating. The average water content in rock salt is 0.1%. This water evaporated at the high temperature of 180-210°C and condensed again in the cooler regions (T<110°C). Therefore, the speciments located on the central heater cask were subject to vapour corrosion, while the specimens located near the drill wall were subject to liquid corrosion. Totally 280 corrosion specimens (140 at 90°C and 140 at 180-210°C) were exposed to the in situ conditions. The specimens were removed from the drift and are subject to examination for general and local corrosion by gravimetry, measurements of pit depths, surface profilometry and metallography.

So far, the specimens which were located at the drift floor at 90°C (vapour corrosion) have been evaluated for general and local corrosion.

The results of the 90°C-specimens are summarized in Tables 1-3. The general corrosion of all materials is extremely low (0.01-1.5 µm/a) and the welding does not increase significantly the corrosion rate. Furthermore, all materials are resistant to local corrosion, except the two Cr-Ni steels 1.4306 and 1.4833, which suffer from pitting corrosion. However, the maximum pit depth after more than 10 years testing is only 50-100 µm. Figures 2 and 3 show by way of an example micrographs of Ti99.8-Pd (uniform corrosion) and Cr-Ni steel 1.4833 (pitting corrosion). In general it can be stated that corrosion of the materials under the in-situ conditions is lower than in the previous laboratory immersion experiments with excess in brine [4,5]. This regards above all the iron-base materials. The lower corrosion rates of the materials under in-situ conditions is attributed mainly to the very small amounts of water/brine present in the in-situ experiment. The investigation of the in-situ stored material specimens will be continued with the evaluation of the 180°C-specimens.

3. References

[1] W. Bechthold et al., „Backfilling and Sealing of Underground Repositories for Radioactive Waste in Salt (BAMBUS Project)," EUR 19124 EN (1999).

[2] K. Janberg, H.Spilker, „Status of the Development of Final Disposal Casks and Prospects in Germany," Nuclear Technology, Vol. 121, No. 2, pp. 136-147 (1998).

[3] J. Droste, H.K. Fedderson, T. Rothfuchs, „Experimental Investigations on the Backfill Behaviour in Disposal Drifts in Rock Salt, „GRS-Report 173 (2001).

[4] E.Smailos, W.Schwarzkopf, B.Kienzler, R.Köster, "Corrosion of Carbon-Steel Containers for Heat Generating Nuclear Waste in Brine Environments Relevant for a Rock-Salt Repository," Scientific Basis for Nuclear Waste Management XV, Mat. Res. Soc. Symp. Proc., **Vol. 257,** pp. 399-406 (1992), edited by C.G. Sombret.

[5] E.Smailos, W.Schwarzkopf, R.Storch, "Corrosion Studies on Packaging Materials for High-Level Waste Disposal in a Rock-Salt Repository," Proc. of the 12th Scandinavian Corrosion Congress and Eurocorr '92, Espoo, Finland, June 1992, edited by P.J.Tunturi (Corrosion Society of Finland, 1992), **Vol. II**, pp. 327-338 (1992).

Table 1: Corrosion of Ti- and Ni-base materials under in-situ conditions in rock salt (BAMBUS II: 90°C/3740 days)

Material	Material condition	Average corrosion rate (µm/a)	Pitting corrosion (µm)
Ti99.8-Pd	A TIG EB	0.01 ± 0.01 0.02 ± 0.01 0.02 ± 0.01	none
Hastelloy C4	A TIG EB SAW	0.02 ± 0.01 0.02 ± 0.01 0.03 ± 0.01 0.02 ± 0.01	none
Hastelloy C22	A TIG EB	0.02 ± 0.01 0.02 ± 0.01 0.02 ± 0.01	none
Nickel	A	0.01 ± 0.01	none

A = as-delivered; TIG = Tungsten Inert Gas welded; EB = Electron Beam welded
SAW = Submerged Arc welded

Table 2: Corrosion of iron-base materials under in-situ conditions in rock salt (BAMBUS II: 90°C/3740 days)

Material	Material condition	Average corrosion rate (µm/a)	Pitting corrosion (µm)
TStE355	A TIG EB	0.07 ± 0.01 0.11 ± 0.02 0.02 ± 0.01	none
15MnNi6.3	A SAW	0.05 ± 0.01 0.06 ± 0.03	none
TStE460	A SAW EB	0.04 ± 0.01 0.07 ± 0.01 0.16 ± 0.05	none
Cast iron	A	0.09 ± 0.04	none

A = as-delivered; TIG = Tungsten Inert Gas welded; EB = Electron Beam welded
SAW = Submerged Arc welded

Table 3: Corrosion of Cr-Ni-steels under in-situ conditions in rock salt (BAMBUS II: 90°C/3740 days)

Material	Material condition	Average corrosion rate (µm/a)	Pitting corrosion (µm)
SS 1.4306	A TIG	0.98 ± 0.90 0.90 ± 0.80	100 100
SS 1.4833	A TIG	0.30 ± 0.20 1.50 ± 1.40	50 60

A = as-delivered; TIG = Tungsten Inert Gas welded

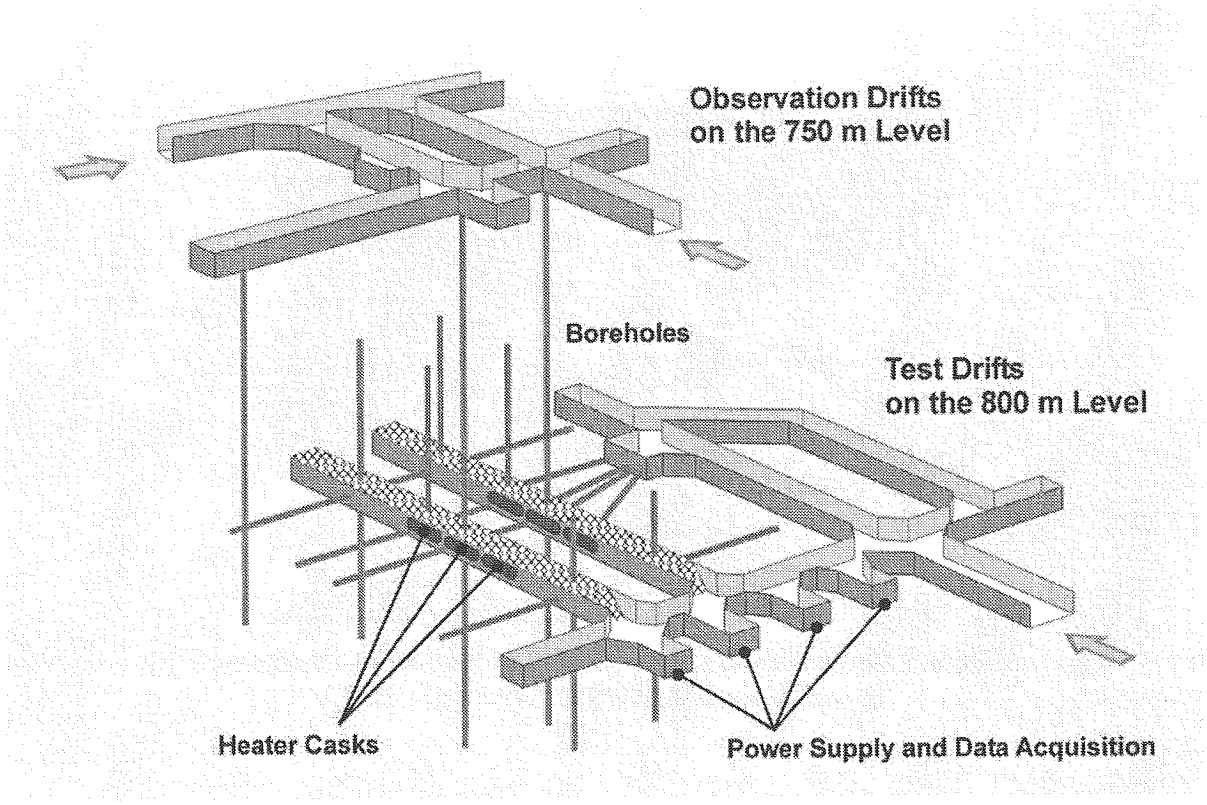

Figure 1: General view of the TSDE test field

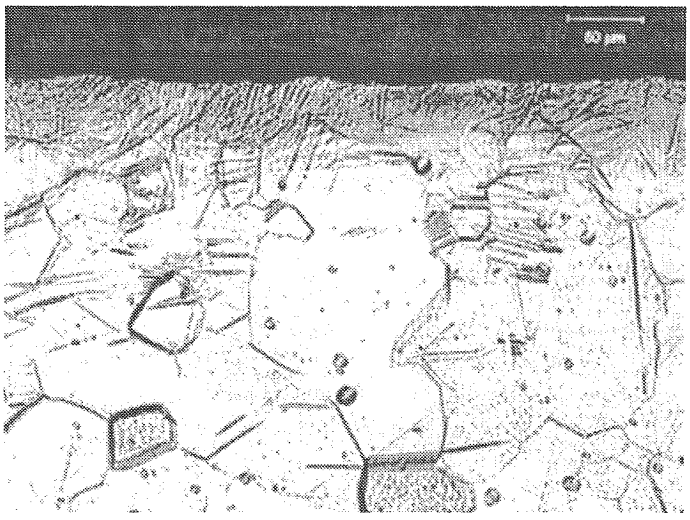

Figure 2: Optical micrograph of Ti99.8-Pd after in-situ storage in rock salt (BAMBUS II: 3740 days, 90°C)

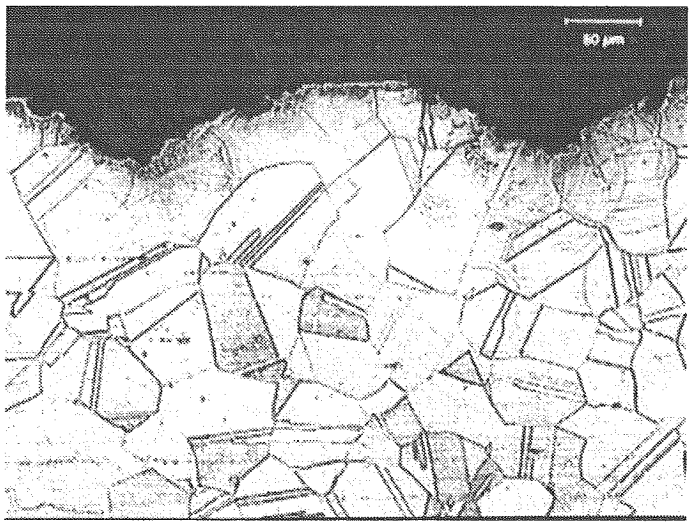

Figure 3: Optical micrograph of 1.4833 SS after in-situ storage in rock salt (BAMBUS II: 3740 days, 90°C)

Application of LIBD to determine the solubility product of $Th(OH)_4(am)$

V. Neck, R. Müller, M. Bouby, M. Altmaier and J.I. Kim

Abstract

The solubility of amorphous Th(IV) hydroxide is investigated in acidic 0.5 M NaCl solutions at 25°C. The laser-induced breakdown detection (LIBD) is used to monitor the initial formation of $Th(OH)_4(am)$ colloids during the coulometric titration of $1.2 \cdot 10^{-2}$ - $1.0 \cdot 10^{-5}$ M thorium solutions in the pH range of 2.7 - 4.5. The accurate solubility limit determined by this method is comparable with data measured from undersaturation with an x-ray amorphous solid precipitated at higher pH and dried at room temperature. Based on the hydrolysis constants selected in our recent review, the solubility product of $Th(OH)_4(am)$ in 0.5 M NaCl is calculated to be $\log K'_{sp} = -44.48 \pm 0.24$ and $\log K°_{sp} = -47.8 \pm 0.3$ (converted to I = 0 with the SIT coefficients of the NEA-TDB).

1. Introduction

The solubility of amorphous Th(IV) precipitates, called either amorphous hydroxides $Th(OH)_4(am)$ or hydrous oxides $ThO_2 \cdot xH_2O(am)$, has been investigated by Nabivanets and Kudritskaya [64NAB/KUD] at 17°C in 0.1 M $NaClO_4$, by Moon [89MOO] at 18°C in 0.5 M $NaClO_4$, and by Rai et al. at 22 - 25°C in 0.1 M $NaClO_4$ [87RYA/RAI], 0.6 M NaCl and KCl [91FEL/RAI, 97RAI/FEL] concentrated NaCl and $MgCl_2$ solutions [97RAI/FEL], and in 0.1 M NaCl [2000RAI/MOO]. In these studies, the amorphous precipitates were not dried or treated at higher temperature but only washed with water. Although relatively widely scatted, the solubilities determined in these studies at pH 3.5 - 5 are reasonably consistent. Using a precipitate dried at room temperature for one week in a vacuum desiccator, Östhols et al. [94ÖST/BRU] measured the solubility at 25°C in 0.5 M $NaClO_4$. Their results are 3 - 4 orders of magnitude lower than those in [64NAB/KUD, 89MOO, 91FEL/RAI, 97RAI/FEL, 2000RAI/MOO] but still about 6 orders of magnitude higher than for crystalline $ThO_2(cr)$.

Recently, Bundschuh et al. [2000BUN/KNO] developed a alternative (non-equilibrium) method to investigate the solubility of oxides or hydroxides. Coulometric pH titration was combined with the LIBD to detect initial colloid formation as a function the H^+ and Th(IV) concentration in 0.5 M HCl/NaCl. Considering colloids as small solid particles, their formation indicates that the solubility is just exceeded during the titration. As an unexpected result, the titrations in the pH range 1.5 - 2.5 led to the formation of small $ThO_2(s)$ colloids with a mean diameter of 16 - 23 nm [2000BUN/KNO], which subsequently agglomerate to a

microcrystalline precipitate [2001ROT/DEN]. The same titration-LIBD method is applied in the present study, however at pH 3 - 5. In this higher pH range, hydrolysis and polynucleation lead to the formation of amorphous thorium hydroxide colloids [2001?ROT/DEN]. The H^+ and Th(IV) concentrations at the onset of colloid formation define the solubility of $Th(OH)_4(am)$ excluding colloidal thorium species.

The hitherto available data on the solubility and hydrolysis of tetravalent actinides have been critically discussed in our recent review [2001NEC/KIM]. They are summarized in Table 1. Activity coefficients are calculated using the specific ion interaction theory (SIT) [92GRE/FUG]. The total Th(IV) equilibrium concentration is given by

$$[Th]_{tot} = [Th^{4+}] + \Sigma\, x\, [Th_x(OH)_y^{4x-y}] \qquad (1)$$
$$= K'_{sp}\,[OH^-]^{-4} + \Sigma\, x\, (K'_{sp}\,[OH^-]^{-4})^x\, \beta'_{xy}\,[OH^-]^y)$$

The calculated solubility product is directly correlated with the hydrolysis constants used in Eq.(1). The solubility products reported in the literature for $Th(OH)_4(am)$ or $ThO_2 \cdot xH_2O(am)$ differ by orders of magnitude, even if the experimental solubilities are in reasonable agreement: e.g. Rai et al. calculated log $K°_{sp}$ = - 45.5 [91FEL/RAI, 97RAI/FEL]) and - 44.9 [2000RAI/FEL], whereas Nabivanets and Kudritskaya calculated log K'_{sp} = - 41.1 (corresponding to - 43.2 at I = 0) and Moon calculated log K'_{sp} = -50.52 in 0.5 M $NaClO_4$ [89MOO] (corresponding to - 53.6 at I = 0). The main reason for these discrepant numbers are the different hydrolysis constants applied by the authors. Rai et al. [91FEL/RAI, 97RAI/FEL, 2000RAI/MOO] even neglect hydrolysis. If the solubility products are re-calculated from the experimental data at pH < 5 with the hydrolysis constants and SIT coefficients in Table 1, the log $K°_{sp}$ values lie within the range of - 46.2 to - 47.3. The considerably lower solubility product given in [94ÖST/BRU], log $K°_{sp}$ = - 48.7 (based on the hydrolysis constants in [91GRE/LAG]), becomes - 48.2 if recalculated with the hydrolysis constants in [2001NEC/KIM]. In the present study an attempt is made to elucidate by LIBD, whether the higher solubilities measured in other studies are due to chemical differences in the solids or to the inclusion of colloids.

2. Experimental

$Th(NO_3)_4 \cdot 5H_2O$ (p.a.), NaCl (p.a.) and HCl (ultrapure) are purchased from Merck. For further purification, NaCl is recristallized twice. Alkaline solutions are prepared with carbonate-free NaOH (Baker) and stored in an argon glove box. Colloid-free thorium stock solutions for the titration-LIBD experiments are obtained by double filtrations through Amicon 10 kD ultrafilters. All solutions are prepared with ultrapure water from a water purification apparatus (Milli-Q-academic, Millipore).

Table 1. Thermodynamic constants at I = 0 and ion interaction (SIT) coefficients for Th(IV) species at 25°C (from [2001NEC/KIM])

Solubility product of $Th(OH)_4(am)$: $\log K°_{sp} = -47.0 \pm 0.8$

Formation constants $\log \beta°_{xy}$ and hydrolysis constants $\log K°_{xy}$ for the complexes $Th_x(OH)_y^{4x-y}$ a)

$\log \beta°_{1,1} = 11.8 \pm 0.2$	$\log K°_{1,1} = -2.2 \pm 0.2$
$\log \beta°_{1,2} = 22.0 \pm 0.6$	$\log K°_{1,2} = -6.0 \pm 0.6$
$\log \beta°_{1,3} = 31.0 \pm 1.0$	$\log K°_{1,3} = -11.0 \pm 1.0$
$\log \beta°_{1,4} = 38.5 \pm 1.0$	$\log K°_{1,4} = -17.5 \pm 1.0$
$\log \beta°_{2,2} = 22.3$	$\log K°_{2,2} = -5.7$
$\log \beta°_{4,8} = 91.6$	$\log K°_{4,8} = -20.4$
$\log \beta°_{4,12} = 141.3$	$\log K°_{4,12} = -26.7$
$\log \beta°_{6,15} = 176.0$	$\log K°_{6,15} = -34.0$

Ion interaction (SIT) coefficients:

i	j	ε_{ij}	j	ε_{ij}
H^+	ClO_4^-	0.14 ± 0.02 b)	Cl^-	0.12 ± 0.01 b)
OH^-	Na^+	0.04 ± 0.01 b)		
Th^{4+}	ClO_4^-	0.67 ± 0.1 c)	Cl^-	0.25 ± 0.03 b)
$Th(OH)^{3+}$	ClO_4^-	0.45 ± 0.1 c)	Cl^-	0.2 ± 0.1 c)
$Th(OH)_2^{2+}$	ClO_4^-	0.3 ± 0.1 c)	Cl^-	0.1 ± 0.1 c)
$Th(OH)_3^+$	ClO_4^-	0.15 ± 0.1 c)	Cl^-	0.05 ± 0.1 c)
$Th(OH)_4°$	ClO_4^-	0 b)	Cl^-	0 b)
$Th(OH)_4°$	Na^+	0 b)		
$Th_2(OH)_2^{6+}$	ClO_4^-	1.3 d)		
$Th_4(OH)_8^{8+}$	ClO_4^-	1.7 d)		
$Th_4(OH)_{12}^{4+}$	ClO_4^-	0.4 d)		
$Th_6(OH)_{15}^{9+}$	ClO_4^-	5.6 ± 1.9 d)		

a) $\log \beta°_{xy}$ refers to the reaction: $x\ Th^{4+} + y\ OH^- <=> Th_x(OH)_y^{4x-y}$
$\log K°_{xy}$ refers to the reaction: $x\ Th^{4+} + y\ H_2O <=> Th_x(OH)_y^{4x-y} + y\ H^+$

b) from the NEA-TDB [92GRE/FUG]

c) Estimated in [2001NEC/KIM] according to the analogies and systematics pointed out in the NEA-TDB [92GRE/FUG]

d) Calculated from the $\Delta\varepsilon$ values derived in [2001NEC/KIM].

Thorium concentrations > $3 \cdot 10^{-7}$ mol/l are determined photometrically by the arsenazo-method [94ÖST/BRU]. Lower thorium concentrations are determined by ICP-MS (ELAN 6100, Perkin Elmer). Combination pH electrodes (type ROSS, Orion Co.) are used to determine the H^+ concentration in 0.5 M NaCl solution. They are calibrated against standard pH buffers (pH 1 - 10, Merck) and standard solutions x M HCl / (0.5 - x) M NaCl with x in the range 0.001 - 0.1.

The coulometric titration of $1.2 \cdot 10^{-2}$ to $1.0 \cdot 10^{-6}$ M thorium nitrate solutions (60 ml) at I = 0.5 M (NaCl) and initial H^+ concentrations in the range -log $[H^+]$ = 2.7 - 4.1 is performed in a double-walled titration vessel, thermostated at 25°C, with the equipment described in [2000BUN/KNO]. A peristaltic pump is used to pump the titration solution through a flow-through cuvette for simultaneous colloid detection by LIBD. Since titrations performed with a current of 0.3 - 1 mA lead to local oversaturation, provoking the formation of unstable colloids, the titration velocity is decreased, i.e., the current is reduced to 0.05 mA (corresponding to the addition of $4.48 \cdot 10^{-2}$ mmol OH^- per day to 60 ml solution). As a consequence, the titration of Th(IV) solutions above 10^{-3} M requires titration times up to several weeks. The pH electrode is freshly calibrated before and re-calibrated at the end of each experiment. In the case of titrations lasting more than 2 days, the electrode is re-calibrated after 2 - 3 days. The measured values of log $[H^+]$ are corrected for the electrode potential shift (usually below 0.03 pH-units per day). In each experiment, the thorium concentration is determined in unfiltered aliquots taken at the beginning and at the end, in some experiments also during the titration, to elucidate sorption effects. In addition, 1 kD filtration (Filtron, pore size ca. 1.2 nm) is applied to quantify the fraction of Th(IV) colloids.

The experimental setup of the LIBD apparatus used in the present study and its calibration with reference colloids have been described previously [96SCH/KNO, 2000BUN/KNO 2001BUN/KNO]. The laser pulse energy of the Nd-YAG laser (Continuum; Surelite, λ_{em} = 532 nm, repetition rate 20 Hz) is adjusted to a constant value of 0.35 mJ and a CCD camera is used to record the plasma light emission, magnified by a macro-microscope. The breakdown probability is derived from 3000 laser shots.

3. Results and discussion

The onset of colloid formation is determined by coulometric pH titration of colloid-free $Th(NO_3)_4$ solutions (0.5 M NaCl, pH $\geq$ 2.7) as a function of the H^+ and Th concentration. The initial formation of colloids during the titration is recognized by the increase of the breakdown probability (number of breakdown events per laser pulse). Considering colloids as small solid particles, the H^+ and thorium concentrations at the onset of colloid formation define the solubility of thorium hydroxide excluding colloidal thorium species. The

experimental data of the present study, thorium and H^+ concentrations at different stages of the titration experiments, are summarized in Table 2. The formation of appreciable amounts of colloids above the onset of colloid formation determined by LIBD is corroborated by the decrease of the thorium concentration after 1 kD filtration at the end of the titration experiments.

It must be emphasized that the present titration-LIBD experiment, although performed with the same equipment, is not comparable with the previous study of Bundschuh et al. [2000BUN/KNO]. In that previous paper [2000BUN/KNO], the titration in the range pH = 1.5 - 2.5 led to the formation of thorium oxide colloids, which subsequently agglomerate and form precipitates after some weeks [2001ROT/DEN]. At these low pH values, the solid particles are formed in solutions where $Th^{4+}(aq)$ is the predominant aqueous species. The present titrations at pH > 3 lead to hydrolysis of the $Th^{4+}(aq)$ ion and polynucleation up to the formation of amorphous hydroxide colloids. The chemical and structural differences between the microcrystalline ThO_2 particles formed at pH 1.5 - 2.5 and the amorphous hydroxide colloids formed at pH 3 - 4 are explicitly demonstrated and discussed in the EXAFS study of Rothe et al. [2001ROT/DEN].

Fig. 1a shows the breakdown probability measured as a function of the H^+ concentration in a series of $5.0 \cdot 10^{-3}$ - $1.0 \cdot 10^{-5}$ M thorium nitrate solutions. These titrations are performed within 1 - 2 days. In the experiment at $[Th]^\circ = -5.0 \cdot 10^{-3}$ mol/l (LIBD-1), a small increase of the breakdown probability occurs already at $-\log [H^+] = 3.15$, i.e., considerably before the formation of a large amount of colloids in the range of $-\log [H^+] = 3.35$ - 3.40 leads to a breakdown probability of 100%. In this experiment the coulometric titration is performed with a current of 1 mA (corresponding to the addition of $3.73 \cdot 10^{-2}$ mmol OH^- per hour to 60 ml solution). In several further titration experiments performed with a current of 0.3 - 1 mA, the breakdown probability of $1.0 \cdot 10^{-4}$ M thorium solutions at $\log [H^+] = 2.8$ to 3.2 increases continuously, starting from the beginning of the titration. As Th(IV) has an extremely high tendency toward polynucleation in this pH range, even a small local oversaturation provokes the formation of unstable colloids already below the solubility limit. However, these colloids re-dissolve within a few days. In the other experiments shown in Fig.1a, this effect is avoided by decreasing the titration velocity, i.e., by performing the titration with a current of 0.05 mA.

As a consequence of the low titration velocity necessary to avoid colloid formation caused by local pH gradients, the titration of solutions with high thorium concentrations of $[Th]^\circ = 1.2 \cdot 10^{-2}$ mol/l (LIBD-10) and $3.0 \cdot 10^{-3}$ mol/l (LIBD-11) requires long times of 35 and 11 days, respectively (Fig. 1b). The largest part of the OH^- ions is consumed by the hydrolysis reactions of thorium and only a small part remains for increasing the pH.

Table 2 Th(IV) and H^+ concentrations at the beginning, at the onset of colloid formation (printed bold) and at the end of the present titration experiments at I = 0.5 M (NaCl) and 25°C.

Experiment	log [Th] **bold: initial colloid formation**	-log [H^+]	[Th] (mol/l) unfiltered	1 kD filtration
LIBD-10		2.70	$1.21 \cdot 10^{-2}$	
		3.15	$1.18 \cdot 10^{-2}$	
	- 1.93 ± 0.01 [a]	**3.18 ± 0.04**		
		3.26	$1.15 \cdot 10^{-2}$	$1.04 \cdot 10^{-2}$
LIBD-1		3.02	$5.0 \cdot 10^{-3}$	
	- 2.33 ± 0.04 [a]	**3.37 ± 0.03**		
		3.50	$4.3 \cdot 10^{-3}$	$2.7 \cdot 10^{-3}$
LIBD-11		3.01	$3.0 \cdot 10^{-3}$	
	- 2.53 ± 0.02 [a]	**3.32 ± 0.03**		
		3.70	$2.9 \cdot 10^{-3}$	$8.9 \cdot 10^{-4}$
LIBD-5		2.94	$4.9 \cdot 10^{-4}$	
	- 3.32 ± 0.02 [a]	**3.61 ± 0.02**		
		3.69	$4.7 \cdot 10^{-4}$	
LIBD-6		3.23	$9.4 \cdot 10^{-5}$	
	- 4.10 ± 0.08 [a]	**3.86 ± 0.03**		
		4.03	$6.8 \cdot 10^{-5}$	
LIBD-7		3.53	$9.3 \cdot 10^{-6}$	
	- 5.10 ± 0.10 [a]	**4.19 ± 0.03**		
		5.49	$1.3 \cdot 10^{-7}$	
LIBD-8		3.83	$1.04 \cdot 10^{-5}$	
	- 5.07 ± 0.10 [a]	**4.22 ± 0.03**		
		4.29	$6.9 \cdot 10^{-6}$	
		4.87	$3.2 \cdot 10^{-6}$	
		5.27	$1.4 \cdot 10^{-7}$	
LIBD-9 [b]		4.06	$9.7 \cdot 10^{-7}$	
		4.18	$7.4 \cdot 10^{-7}$	
		4.33	$4.5 \cdot 10^{-7}$	
		4.60	$2.9 \cdot 10^{-7}$	
		5.33	$1.7 \cdot 10^{-7}$	

[a] These log [Th] values represent the mean value of the concentrations measured before and after the onset of colloid formation.

[b] No significant increase of the breakdown probability.

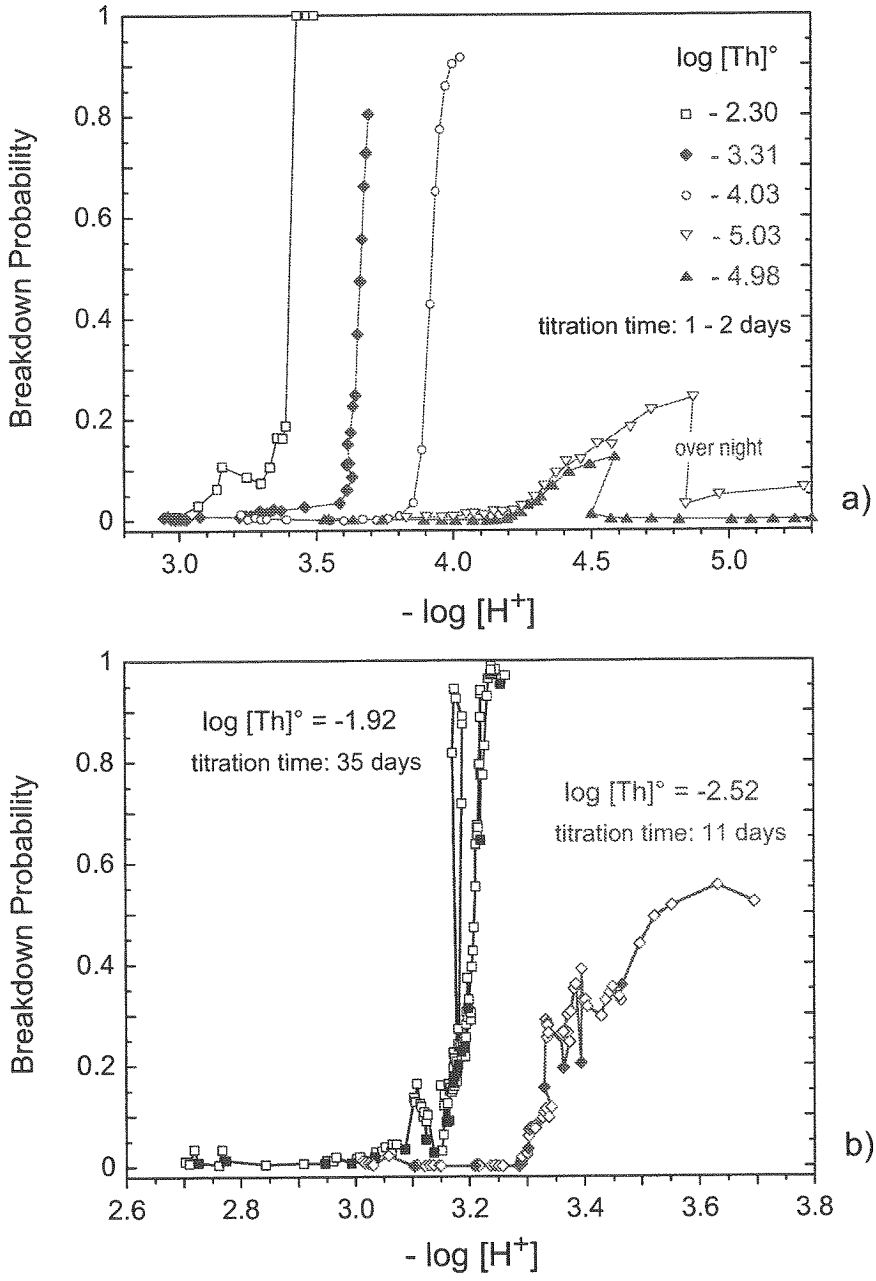

Fig.1. Titration-LIBD experiments at 25°C: breakdown probability as a function of the H^+ concentration during the coulometric titration of $1.2 \cdot 10^{-2}$ - $1.0 \cdot 10^{-5}$ M thorium nitrate solutions in 0.5 M NaCl.

Despite the slow titration, the initiation of colloid formation below the solubility limit is not completely avoided at these high thorium concentrations. However, upon stopping the titration or reducing the current to values < 0.01 mA overnight or over the weekend (filled points in Fig.1b), these unstable colloids re-dissolve. In order to exclude such artefacts, the long-time stability of the thorium colloids present at the end of the titration experiment is

ascertained by measuring the breakdown probablity in aliquots of the final solutions over a period of 1 - 3 months. In experiment LIBD-11, the breakdown probability remains at a value of about 50% even after continuing the titration up to -log $[H^+]$ = 3.70. However, 1 kD filtration of the final thorium solution shows that 70 % of the thorium is present as colloids.

Sorption of thorium onto the glass surface of the reaction vessel is a problem, particularly in the experiments at low thorium concentrations (c.f. thorium concentration measured in unfiltered aliquots at different stages of the titrations, Table 2). In the experiments at $[Th]^\circ > 10^{-4}$ mol/l, the observed decrease of the thorium concentrations is less than 20%. However, during the titration experiments at $[Th]^\circ \leq 10^{-5}$ mol/l and pH > 4, the thorium concentrations decrease to 10^{-7} mol/l. Because of this sorption effect the breakdown probability in the two experiments at $[Th]^\circ = 1 \cdot 10^{-5}$ mol/l (LIBD-7, LIBD-8) do not reach high values and decrease to the background level when the titration is stopped overnight (Fig.1a). In experiment LIBD-9, the initial thorium concentration of $1 \cdot 10^{-6}$ mol/l decreases continuously from the start of the titration (c.f. Table 2) and the breakdown probability does not exceed 7%. Therefore, the applicability of the present method and equipment is restricted to $[Th] \geq 10^{-5}$ mol/l.

The results of the titration-LIBD experiments, i.e. the H^+ and Th(IV) concentrations at the onset of colloid formation, are comparable with the solubility data measured by Östhols et al. [94ÖST/BRU] and in the present study with amorphous precipitates dried at room temperature (Fig.2). This finding gives rise to the conclusion that the high solubilities determined at -log $[H^+]$ = 3.5 - 5 with precipitates not dried but only washed with water include large amounts of small colloids, in spite of the fact that Moon [89MOO] and Rai et al. [87RYA/RAI, 91FEL/RAI, 97RAI/FEL, 2000RAI/MOO] determined the thorium concentration after filtration at a pore size of about 2 nm. Amorphous precipitates only washed with water may include small particles, which easily become suspended in the solubility experiment, whereas dehydration of the solid by drying may lead to larger agglomerates in the solid and, hence, to less colloids in the solubility experiment.

The solubility data defined by the onset of colloid formation are used to calculate the solubility product of $Th(OH)_4(am)$. As the experimental data do not allow to determine the solubility product independently of the hydrolysis constants, the log β°_{xy} values in [2001NEC/KIM] are converted to I = 0.5 M and used as fixed values in Eq.(1). Considering also the uncertainties in the selected hydrolysis constants, the following solubility product is obtained for $Th(OH)_4(am)$:

$$\log K'_{sp} = -44.48 \pm 0.24 \text{ (in 0.5 M NaCl)}$$

and

$$\log K^\circ_{sp} = -47.8 \pm 0.3 \text{ (converted to I = 0 with the SIT)}$$

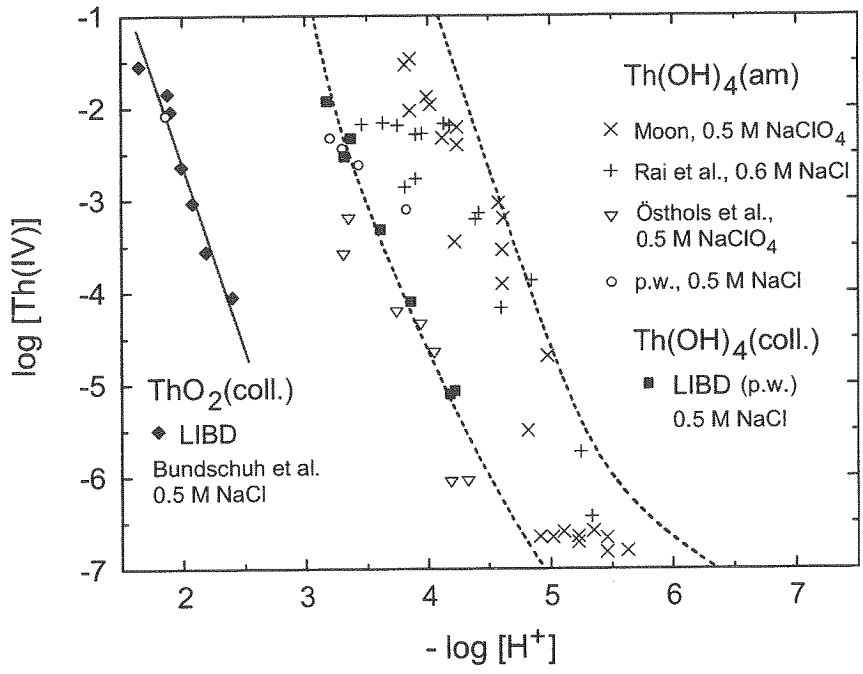

Fig.2. Comparison of the present titration-LIBD data at the onset of $Th(OH)_4(am)$ colloid formation with classical solubility data for amorphous Th(IV) solids at comparable ionic strength of I = 0.5 - 0.6 M). The lower and upper dashed curves are calculated with log $K°_{sp}$ = - 47.8 and - 46.2, respectively, and the hydrolysis constants in Table 1.
The considerably lower titration-LIBD data of Bundschuh et al. [2000BUN/KNO], for the initial formation of ThO_2(colloids) in the pH range 1.5 - 2.5, are also shown for comparison.

The calculated solubility curve is shown as a solid line in Fig. 3a. The calculated speciation along this solubility curve predicts $Th(OH)^{3+}$ as the predominant complex in the range -log $[H^+]$ = 3.6 - 4.3 (Fig.3b). This is consistent with the experimental data, which decrease with a slope of about -3. At -log $[H^+]$ < 3.5 and [Th] $>10^{-3}$ mol/l, polynuclear species become predominant. For the titrations at [Th] $>10^{-3}$ mol/l, this is confirmed by the bilance between the total OH^- added coulometrically and the fraction of OH^- consumed for increasing the pH. Appreciable amounts of small polynuclear species are formed already prior to the onset of colloid formation. For instance, in experiment LIBD-10 at [Th°] = $1.2 \cdot 10^{-2}$ mol/l, an avarage number of $n'_{OH/Th}$ = 0.9 ± 0.1 mmol OH^- ions per mmol thorium are consumed by hydrolysis reactions during the titration from -log $[H^+]$ = 2.70 to the onset of colloid formation at -log $[H^+]$ = 3.18 ± 0.04. This is consistent with the calculated speciation including oligomers. If only mononuclear species are taken into account, the calculated value of $n_{OH/Th}$ = 0.47 is significantly too small.

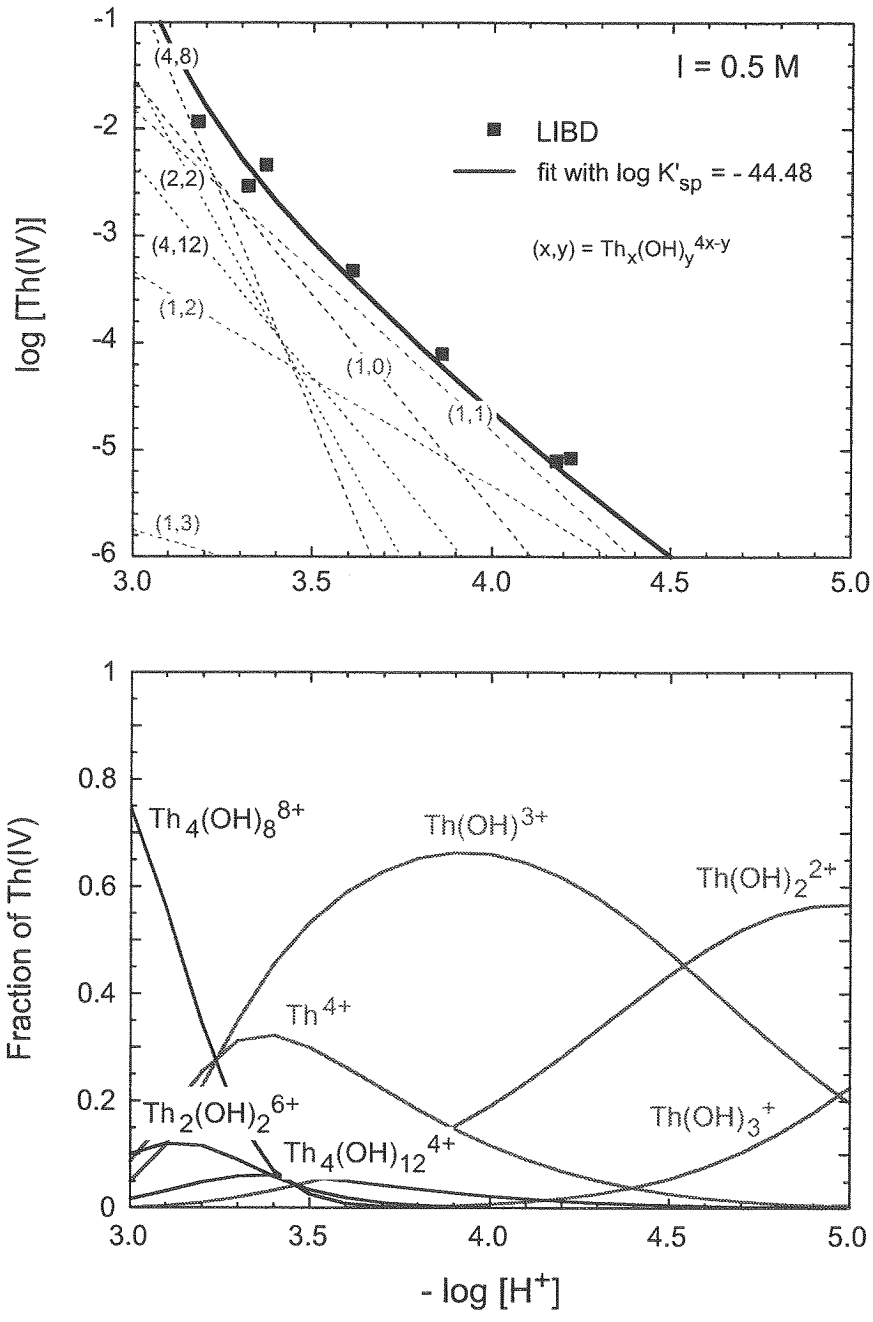

Fig. 3. Solubility data determined in the present titration-LIBD study. The solid curve is calculated with log K'_{sp} = - 44.48 (fit) and the hydrolysis constants in Table 1. The Th(IV) species distribution along the calculated solubility curve is shown below.

Acknowledgements

The authors wish to thank F. Scherbaum, W. Hauser and C. Walther (FZK-INE) for maintaining the LIBD equipment and F. Geyer (FZK-INE) for the ICP-MS analysis.
The present work was partially supported by ANDRA (contract No. 008790) and by the European commission, in the frame of the ACTAF program within the 5th R&D framework program (contract No. FIKW-CT-2000-00035).

References

[64NAB/KUD] Nabivanets, B.I., Kudritskaya, L.N., Ukr. Khim. Zh. **30**, 891 (1964).

[87RYA/RAI] Ryan, J.L., Rai, D.; Inorg. Chem. **26**, 4140 (1987).

[89MOO] Moon, H.C.; Bull. Korean Chem. Soc. **10**, 270 (1989).

[91FEL/RAI] Felmy, A.R., Rai, D., Mason, M.J.; Radiochim. Acta **55**, 177 (1991).

[91GRE/LAG] Grenthe, I., Lagermann, B.; Acta Chem. Scand. **45**, 231 (1991).

[92GRE/FUG] Grenthe, I., Fuger, J., Konings, R.J.M., Lemire, R.J., Muller, A.B., Nguyen-Trung, C., Wanner, H. (OECD, NEA-TDB): Chemical Thermodynamics of Uranium, Elsevier, North-Holland, Amsterdam, 1992

[94ÖST/BRU] Östhols, E., Bruno, J., Grenthe, I., Geochim. Cosmochim. Acta **58**, 613 (1994).

[96SCH/KNO] Scherbaum, F., Knopp, R., Kim, J.I, Appl. Physics, **B63**, 299 (1996).

[97RAI/FEL] Rai, D., Felmy, A.R., Sterner, S.M., Moore, D.A., Mason, M.J., Novak, C.F, Radiochim. Acta **79**, 239 (1997).

[2000BUN/KNO] Bundschuh, T., Knopp, R., Müller, R., Kim, J.I., Neck, V., Fanghänel, Th., Radiochim. Acta **88**, 625 (2000).

[2000RAI/MOO] Rai, D., Moore, D.A., Oakes, C.S., Yui, M., Radiochim. Acta **88**, 297 (2000).

[2001BUN/KNO] Bundschuh, T., Knopp, R., Kim, J.I., Colloids Surf. A **177**, 47 (2001).

[2001NEC/KIM] Neck, V., Kim, J.I., Radiochim. Acta, **89**, 1 (2001).

[2001ROT/DEN] Rothe J., Denecke, M.A., Neck, V., Müller, R., Kim, J.I.: XAFS investigation of the Structure of Aqueous Th(IV) Species, Colloids, and Solid Th(IV) Oxide/Hydroxide; submitted to Inorganic Chemistry

On the Way to Element-Selective Colloid-Detection
-Time-Evolution of Plasma Parameters -

C. Walther, C. Bitea, G. Geipel, F.J. Scherbaum

Colloid mediated transport of actinides [1] in the aquifer represents a basic topic in the safety assessment of nuclear waste disposal sites. Despite of their small size colloids below 50nm provide a huge chemical interaction surface due to their large number (Paretos law) and surface to volume ratio (several $10m^2/g$). Hence methods are needed, tailored to the speciation of nm-size colloids in their natural (aqueous) surrounding.

PCS can be applied for high concentrations and large sizes of particles. However, colloids smaller than 50nm in size are detected with very low efficiency. The laser induced breakdown detection (LIBD) can fill this gap. Particles as small as 5nm are detected down to low ppt concentrations [2], but the method does not provide information on the chemical composition of the colloids. Here, we present basic investigations on the plasma ignition and propagation processes aimed at the element selective detection of colloids.

Experimental Setup

The plasma is ignited by a diode pumped pulsed Nd:YAG laser, focused into a quartz cell containing the colloid suspension. The ignition-laser setup closely resembles a setup described before [3] and is only revisited briefly (Fig.1). The frequency doubled light (532nm) of the Nd:YAG laser (Soliton, DIVA II, 22ns $1/e^2$) with a repetition rate of 20Hz and a maximum pulse energy of 10mJ is guided into the cell via two mirrors and a telescope ($f_1 = -50, f_2 = +50$) resulting in a focal diameter of ~ 8µm. Its pulse energy is adjusted by use of two glan polarizers (P1,P2) and monitored on a shot to shot basis by measuring 2% of the beam with a pyroelectric detector (Pyro1). Two fast photodiodes (PD1,PD2) record the temporal profiles of the laser beam in front of and behind the quartz cell (and hence the plasma) which are displayed by a digital storage oscilloscope (LeCroy , 4GS, 1GHz analogue bandwidth). After passing a dicroic mirror (PR2) the beam is stopped in a beam dump.

The plasma opacity is probed by a second, counterpropagating, beam delivered by an amplified fs-laser system (Spectra Physics, Tsunami) capable of 3mJ pulses at 800nm with a repetition rate of 1kHz. For the present experiments the pulses were stretched to 1.7ps and by use of a pulse selector the rate was decreased to 20Hz. In order to avoid problems of external attenuators, the pulse energy is varied by selecting different pulses of the amplified train

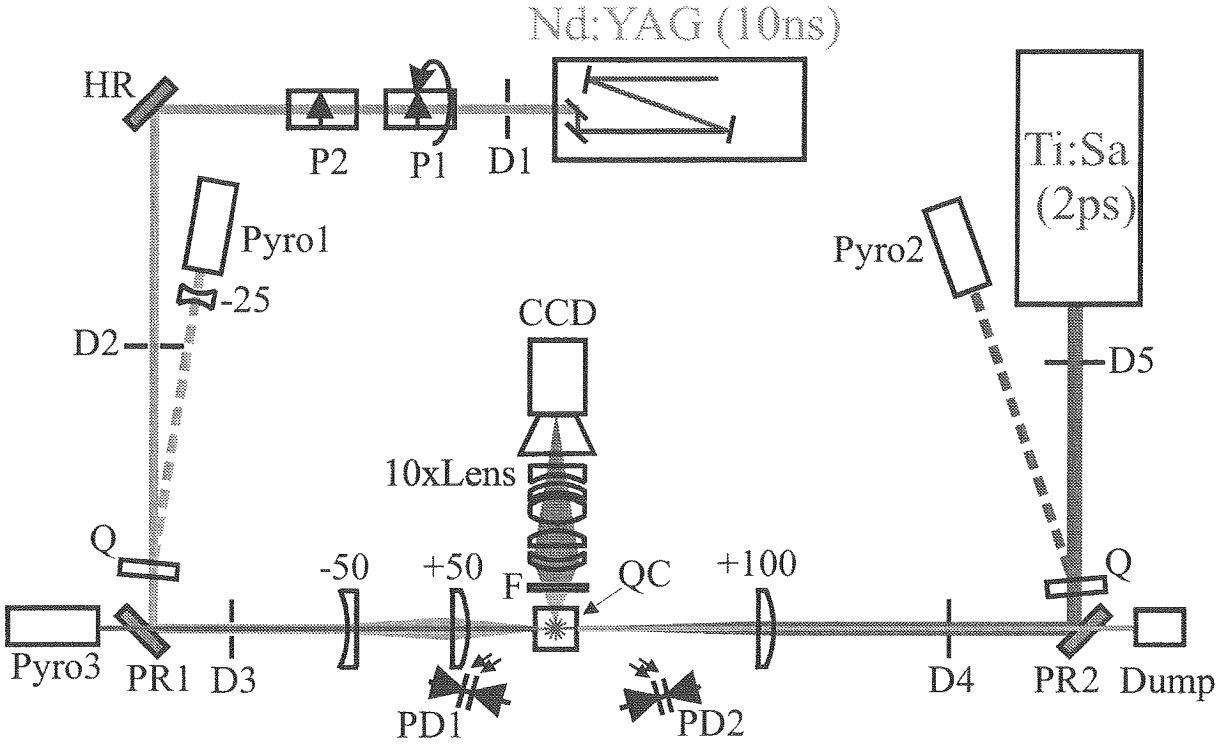

Fig.1: The plasma is ignited by a focused ns laser pulse (Nd:YAG) and probed by a counterpropagating ps-pulse (Ti:Sa). In addition the plasma is observed by a fast CCD camera via a microscope lens (CCD).

covering the range from 1μJ to 3mJ. The energy before entering the cell is measured as described for the YAG laser by a pyroelectric detector (Pyro2). Then the beam is focussed by a f= 100mm planoconvex lens. Due to the longer focal length and a larger divergence the beam waist amounts to ~15μm in the interaction region. After passing the cell the beam is separated from the YAG beam by a dichroic mirror (PR1) and its remaining energy measured by a third pyroelectric detector (Pyro3).

Plasma formation is detected in a twofold manner. First, a piezo-crystal is attached to the cell and detects the shock wave of the expanding plasma. In addition the glowing plasma plume is observed by use of a microscope lens (10 x magnification) and an intensified ultrafast high dynamic range CCD camera (1Hz max. repetition rate, gate times down to 250ps, 14bit resolution).

The ps-laser can only be operated in free running mode and provides the basis for all additional timing performed by high precision delay gate generators (EG&G, SI DG535). While this represents no general problem, it limits the pretrigger time to < 105ns. For the pump probe experiments the YAG laser pulse has to precede the ps-pulse, but no longer

delays than 105ns are possible. Due to the large temporal pulse to pulse jitter of the ps-laser, triggering with regard to the preceding pulse (50ms in advance) fails.

A transient recorder PC card (Spectrum TRP 25, 12bit, 10MHz) acquires the signals of the three energy detectors and the piezo crystal. The data of every single pulse is stored (no online averaging was performed). Later on, background is subtracted from the recorded transients and the integral of a constant number of channels serves as a measure of the three pulse energies and the strength of the acoustic signal respectively. In contrast to the camera readout, the TR is capable of 20Hz real time acquisition and typically 500 successive pulses are recorded.

Measurements

The plasma was investigated in different liquids: Suspensions of ZrO_2 and polystyrene (PS) with a mean diameter of 107nm and 102nm respectively and a mass concentration of 10ppb were used. To account for background effects deionized water was measured as well, which was also investigated in detail for different laser pulse lengths before [5]. In addition to the TR data (which was taken in all series) the spatial evolution of the plasma was recorded by the CCD camera solely in a few cases of special interest.

When only the 22ns pulse ($1/e^2$) of a Nd:YAG laser is focused into the sample the plasma is created within the first ns of the pulse by multiphoton ionization of the particle and avalanche like multiplication through inverse bremsstrahlung [6]. In the further course of the pulse, the plasma keeps absorbing photons leading to an increase in temperature T and electron density n_e. At a critical density

$$n_e = \frac{c^2 m_e \varepsilon_O}{e^2}\left(\frac{2\pi}{\lambda}\right)^2 \qquad (1)$$

the plasma becomes opaque for light of wavelength λ due to Thomson scattering [6]. As a first consequence the later part of the Nd:YAG pulse is absorbed strongly, which has been reported previously [7]. This is measured directly by use of two photodiodes in front and behind the plasma (fig.1). The temporal evolution of the photon flux densities in the case of PS-particles is shown in fig.2, '532nm in front of cell' and '532nm behind cell' respectively. The curves overlap during the first few ns, whereas afterwards behind the cell a strong extinction is observed, shortening the visible laser pulse to about half the width of the incoming pulse. The first few ns the extinction is due to absorption of the plasma (heating),

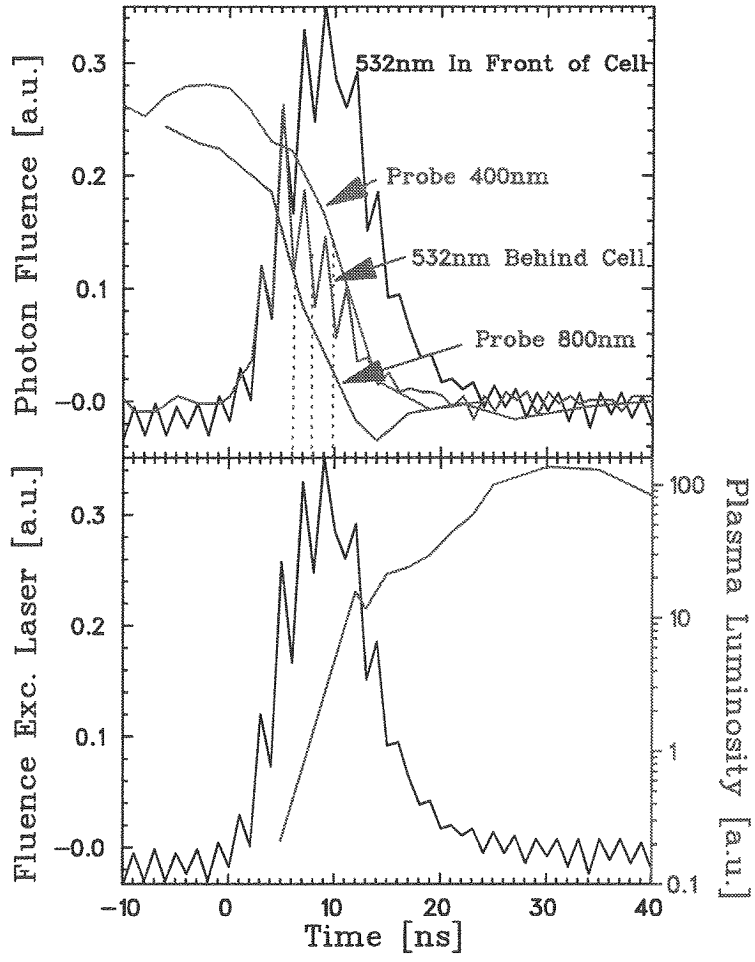

Fig.2: The upper graph shows the temporal evolution of the photon flux density of the plasma creating pulse (532nm) in front of and behind the cell. In addition the transmitted intensity of the two ps-probe pulses is plotted (Probe, 400nm, Probe 800nm). The lower graph shows the buildup of plasma glow (integrated from 1000nm to 380nm) as function of time after ignition by the Nd:YAG laser pulse.

later on Thomson scattering by the hot plasma becomes the dominant process. Eq. (1) predicts a wavelength dependency of the scattering process: Whereas IR light of longer wavelength is scattered already at low electron densities, visible or UV light still is transmitted and not absorbed until the electron density further increases. Experimentally, the opacity is probed by ps- light pulses of 800nm and 400nm respectively at different times Δt after the Nd:YAG pulse. Fig.2 shows averaged values of 500 laser shots for each time Δt . The IR beam (Probe 800nm) is attenuated by 50% at Δt=6ns, whereas the visible pulse (Probe 400nm) is transmitted for the first 10ns. The ignition beam (532 Behind Cell) fits in very well at Δt=8ns. As further evidence that the attenuation is due to plasma formation, serves the integrated luminosity (1000nm-380nm) of the glowing plasma plotted in the lower part of

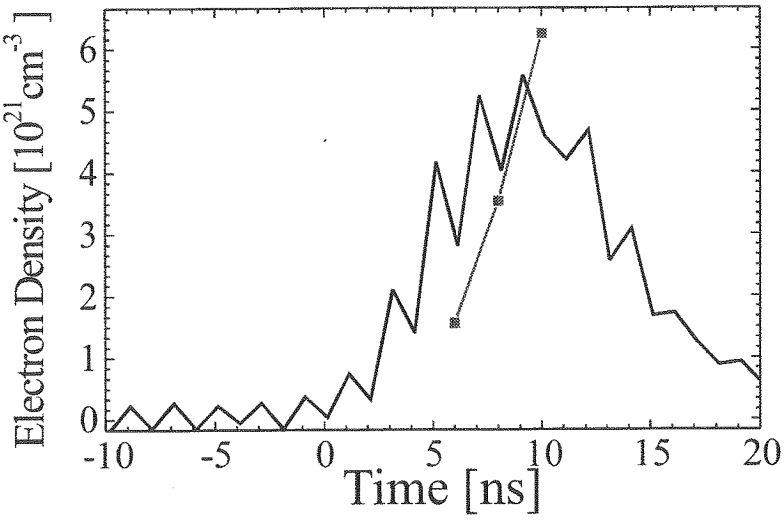

Fig.3: Temporal evolution of electron density of the plasma as probed by light of different wavelengths (details see text).

Fig.2 (note the log scale) as recorded by the CCD camera (averaged over 50 events each). During the laser pulse the detected intensity increases rapidly by three orders of magnitude starting at about Δt=5ns. Eq.(1) allows to draw conclusions from the 50%-attenuation-times on the temporal evolution of the electron density as plotted in fig.3. From ~$1.5 \cdot 10^{21}$cm^{-3} at Δt=6ns the electron density increases to about the four fold value at Δt=10ns. For investigation of earlier processes Thomson Scattering experiments with FIR light would have to be performed.

In a second set of experiments the breakdown probability (i.e. the relative number of breakdown events for a given number of laser shots) is measured as a function of the delay time between both laser pulses (Δt). The pulse energy of the ps laser is chosen below breakdown threshold, so that no plasma is ignited by the ps-laser alone. In contrast, the Nd:YAG laser is operated above threshold at some 25% breakdown probability. In the case of ZrO_2 particles (Fig4.bottom) no effect of the ps-pulse on the breakdown probability is observed (neither at 800nm nor at 400nm). For PS particles, a strong enhancement is measured when the 400nm pulse is fired shortly before or during the ns pulse (-3ns < Δt < 14ns) as can be seen from the upper part of figure 4. However, this effect is not observed for the 800nm pulse.

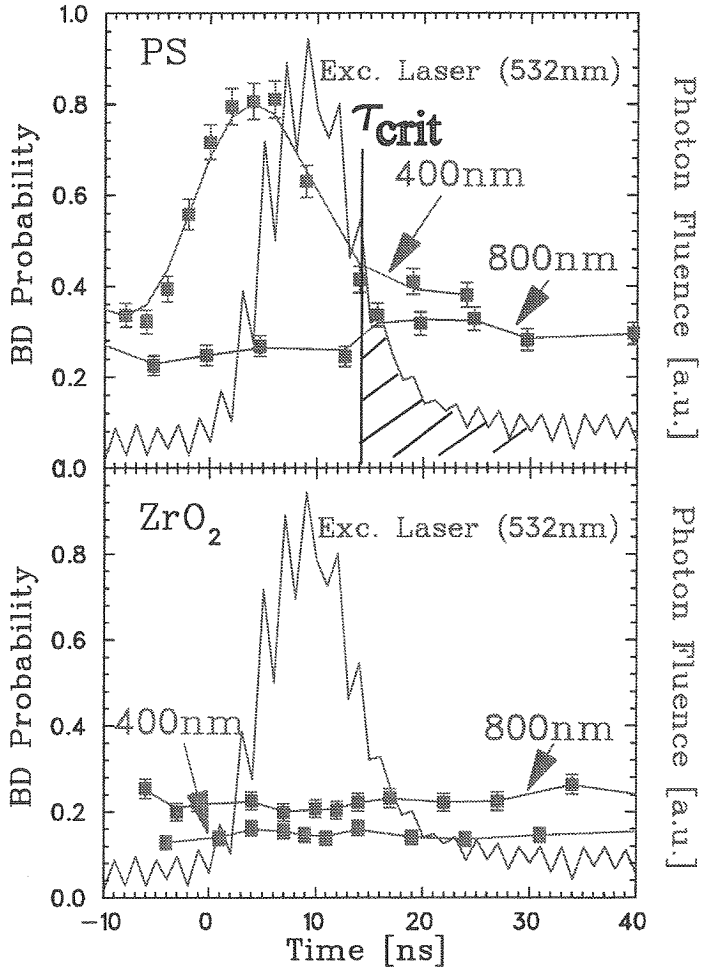

Fig.4: Enhancement of the breakdown probability for PS (top) when the ns is preceded by a weak ps pulse of 400nm. No effect is observed for 800nm. In the case of ZrO_2 for neither wavelength an enhancement was measured.

Conclusions

Plasma ignition starts with the ionization of matter in the laser focus [6]. However, the underlying ionization mechanisms strongly depend on the laser pulse duration as discussed in detail in [7]. Multiphoton ionization (MPI) plays the dominant role for short pulse lasers (ps and below), i.e. most electrons are produced by direct, non-resonant ionization of matter. In contrast, the much smaller field strength of a ns-laser decreases the probability of high order processes as MPI (reviewed for the case of toluene in the gas phase in [8]) and only very few direct electrons are produced. These few 'seed electrons' interact with the laser field by inverse bremsstrahlung which is a linear process and gain kinetic energy of several 10eV, sufficient for impact ionization when they collide with a molecule. The enhancement observed for PS particles is explained as follows: The weak ps-pulse generates free electrons by MPI. However, the pulse energy does not suffice for producing a dense, hot plasma. If the

(high energy) ns-pulse follows within the life time of the free electrons inside the particle or the surrounding water, electron multiplication and plasma heating occurs, resulting in an observable breakdown event. Because the seed electrons have not to be generated by the ns-pulse, but rather are available for multiplication from the very beginning, the breakdown probability is strongly enhanced. The fact that the enhancement only is observed for 400nm is most likely due to the increasing cross section for 3-photon ionization of aromatic groups for λ<440nm as reported for liquid benzene in [9]. In the case of 800nm and also for ZrO_2, which does not exhibit a spectral pattern in this region, the amount of electrons created by the weak ps pulse is not sufficient to appreciably enhance the breakdown probability. This hypotheses is further supported by very recent measurements with a tunable ns laser, where PS particles exhibit increasing non linear absorption in the blue and near UV [10].

A second conclusion can be drawn from the above data. Obviously there is an upper limit for the time, the ps-laser has to provide the seed electrons in order to facilitate plasma formation. For $\Delta t > 14$ns, no enhancement is found. According to [6] at that late stage, the energy that is absorbed from the remaining part of the laser pulse does not generate a plasma strong enough to be observed. This so called 'critical time τ' is an important parameter in modeling breakdown detection [2,3], which had to be assumed or fitted to data so far, but now is a physical value accessible by experiment.

In continuation of this work material dependencies of the enhancement processes will be investigated by performing short-pulse pump-probe experiments with a tunable ps-OPO system to be purchased in 2002.

References

[1] Honeyman (1999). "Colloidal culprits in contamination." Nature 397: 23-24.

[2] F.J. Scherbaum, R. Knopp and J.I. Kim (1996). "Counting of particlesin aqueous solutions by laser-induced photoacoustic beakdown detection." Appl. Phys. B 63: 299-306.

[3] C. Walther, C.Bitea, J.I. Kim and F.J. Scherbaum, "Laser Induced Breakdown Detection for theSpeciation of Aquatic Colloids in Trace Concentrations", submitted for publication

[4] C. Walther and G. Geipel in FZKA Bericht 6629

[5] Noack, J. and A. Vogel (1999). "Laser-Induced Plasma Formation in Water at nanosecond to femtosecond time scales: calculation of thresholds, absorption coefficients and energy density." IEEE J. Quant. Elec. 35(8): 1156-1167.

[6] Radziemski, L. J. and D. A. Cremers (1989). Laser induced Plasmas and Applications. Rochester,Marcel Dekker.

[7] L. Berthe, R. Fabbro, P. Peyre and E. Bartnicki, (1998) "Experimental study of the transmission of breakdown plasma generated during laser shock processing." Eur. Phys. J AP 3: 215-218

[8] C. Walther, A. Herlert, J.I. Kim, F.J. Scherbaum, L. Schweikhard and M. Vogel "Absolute cross- sections for the nonresonant multi-photon ionization of toluene and xylene in the gas phase" Chem. Phys. 265: 243-250

[9] T.W. Scott, C.L. Braun and A.C. Albrecht (1982) "Multiphoton ionisation in the organic condensed phase: A three-photon study of liquid benzene"
J. Chem. Phys. 76(11): 5195-5202

[10] C. Walther et al. to be published

SWEDISH-GERMAN ACTINIDE MIGRATION EXPERIMENT AT ÄSPÖ HRL

P. Vejmelka, B. Kienzler, J. Römer, E. Soballa, T. Kisely, F. Geyer

Objectives and Experiments

Within the scope of a bilateral cooperation between SKB and FZK-INE, *Actinide Migration Experiments* are continuously conducted at the Äspö Hard Rock Laboratory. To guarantee most realistic conditions, the experiments are designed to fit into the in-situ CHEMLAB 2 probe (Jansson, 1997). The objectives of the Actinide Migration Experiments are investigations on the applicability of radionuclide retention coefficients, validation of the radionuclide retardation processes measured in laboratory batch experiments for in-situ conditions, and demonstration of the reliability of laboratory data as well as the reduction of uncertainty in the retardation properties of americium, neptunium, and plutonium.. At first, migration experiments were performed in laboratory, afterwards, the same experiments should be repeated at Äspö HRL.

Actinide tracer cocktails of the long-lived isotopes ^{244}Pu(IV), ^{243}Am(III), and ^{237}Np(V) were prepared according to the maximum solubilities of these actinides in groundwater from Äspö HRL. The concentrations were as follows: ^{244}Pu approx. $1x10^{-8}$ mol/l, ^{243}Am approx. $1x10^{-6}$ mol/l in laboratory, and $1x10^{-8}$ mol/l at Äspö, and ^{237}Np approx. $1x10^{-5}$ mol/l. Total α-activity of the cocktail amounts to $1.8x10^{5}$ Bq/l. Using a calibrated sample loop at the laboratory, the actinide cocktail (pH 7) was injected. Different migration tests were performed using pulse injections and continuous injections. The flow rates were chosen to be 0.3 ml/h (7.2 ml/day). Eluted groundwater was collected in samples. These samples were filtrated (450 nm) and analyzed for total α-activity by liquid scintillation counting (LSC).

The solution sampled at the peak of the breakthrough of the CHEMLAB 2 experiment was tightly closed and transferred to FZK-INE. UV-VIS-NIR spectroscopy was performed with a Cary 5 spectrophotometer (VARIAN) in a 1 cm quartz cuvette. The solution eluted in the Äspö experiment was poured into a cuvette in glove boxes under an argon / 1 % CO_2 atmosphere. Absorption spectra were taken in the wavelength range of 920 to 1040 nm.

Hydraulic properties

To interpret the breakthrough of the actinides, the hydraulic properties of the fractured cores are required. Hydraulic properties, such as effective porosity, dispersion coefficient or breakthrough time can be determined by evaluating the breakthrough curves measured for a non-sorbing tracer like HTO. Breakthrough curves for HTO are shown in Vejmelka (2000).

The zeroth, first, and second-order momentums of the time-dependent breakthrough curves are computed (Appelo, 1994).

The effective porosity of the core was obtained by dividing the Darcy velocity by the pore water velocity. However, this assumption was ambiguous, since effective porosity is generally defined for porous media. This approach is reasonable, because the flow path analyses presented below, did not reveal a well-defined fracture in core #2.

Breakthrough of ^{237}Np

An autoclave with an embedded drill core (#3) was used for the laboratory actinide migration tests with the experimental conditions being the same as in the CHEMLAB 2 experiment. The effective pore volume of both fractures (#2 and #3) was determined to be about 2 ml. The results of the two experiments are shown in Fig. 1. Continuous injections of 14 ml actinide cocktail were applied.

By means of α-spectroscopy, ^{237}Np and ^{243}Am were distinguished in the effluent. In the laboratory experiment, the total ^{243}Am concentration in eluted water was found to be $1x10^{-11}$ mol/l. The recovery of Np was determined to be 26% of the injected quantity. The eluted groundwater volume in the laboratory experiment amounted to 80 ml. The eluted water had the same pH as the injected water. The Eh was measured to be +20 mV. However, in a second and third laboratory experiment with the same core (#3), Eh was measured to be in the range of -200 mV. These later experiments showed a significantly lower Np concentration in the eluted water (by a factor of 10).

Fig. 1 shows breakthrough as a function of the eluted volumes. These volumes are corrected with respect to evaporation of water during the sampling period[a]. In the first in-situ actinide migration experiment at Äspö HRL in October 2000, the cocktail was spiked by HTO additionally to the actinides in order to have an online test method for controlling the experiment. CHEMLAB 2 was equipped with the drill core in the autoclave and a test run was performed for 5 days. After successful operation, a volume of 14 ml of actinide cocktail from the reservoir was injected into the fractured rock sample at a flow rate of 0.3 ml/h. Injection of this volume required 50 hours. Afterwards, natural groundwater was injected for another 5 days at a constant flow rate. pH 7 was measured in the eluted samples, Eh ranged from +30 to -60 mV. The eluted groundwater samples were transferred to FZK-INE. ICP-MS measurements resulted in ^{243}Am and ^{244}Pu the concentrations below the detection limit of $1x10^{-12}$ mol/l. From these findings, it may be concluded that only ^{237}Np contributes to the measured α-concentration. This result is equivalent to the results obtained by the migration experiment at the laboratory. The recovery of ^{237}Np was computed to be 40% of the injected quantity.

[a]At the applied flow rate (0.001 ml/min), a loss of water of 30% per sample was measured in the Äspö glove box and 15% at the laboratory.

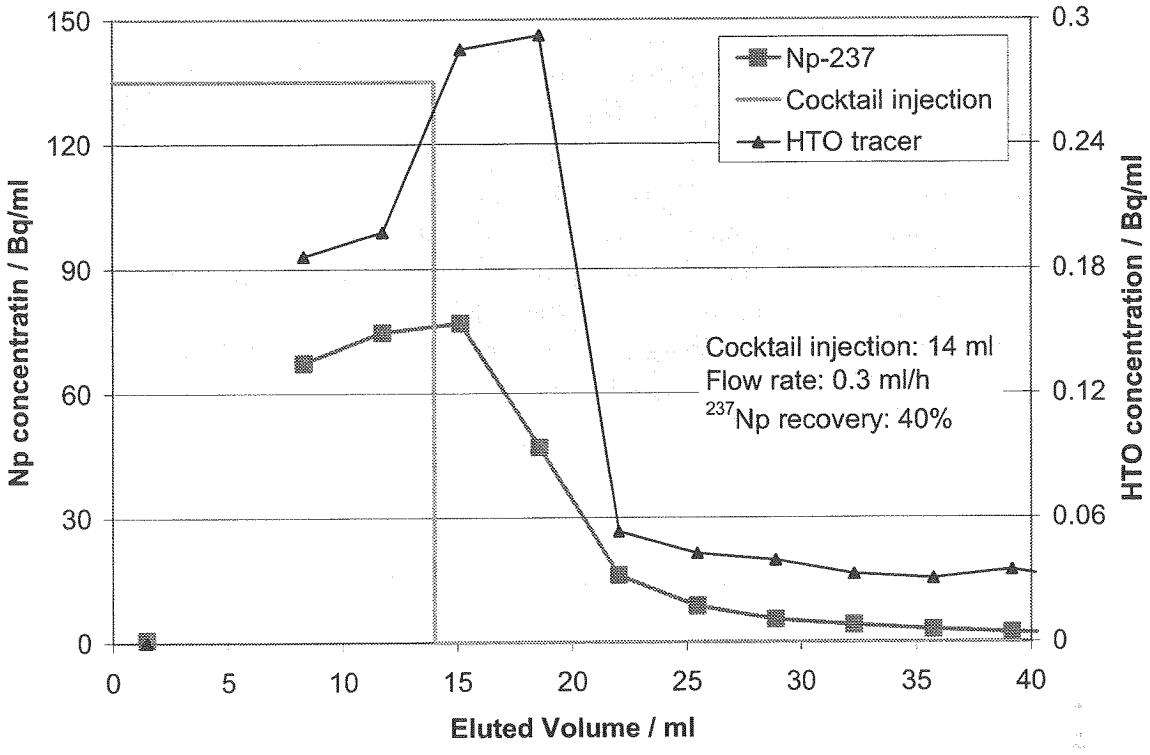

Fig. 1 Breakthrough curves for ^{237}Np determined for core #4 at the laboratory and core #2 in the CHEMLAB 2 experiment as well as HTO breakthrough as obtained by the CHEMLAB 2 experiment.

Flow path analyses

The cores used in the experiments were analyzed with respect to the flow path and interactions between dissolved actinides and the solid phases. Analysis of the flow path was performed by non-destructive methods, such as X-ray computer tomography, and destructive methods.

Destructive investigations were performed as follows: A fluorescent epoxy resin was pumped into the fractures after drying the system by injection of isopropanol. The epoxy resin itself had a viscosity that significantly exceeded the value of groundwater [b]. For this reason, a pressure of up to 100 bar was required. After injection of the fluorescent epoxy resin, the cores were cut perpendicular to the cylinder axis. The resulting slices had a thickness of 3 mm, the thickness of the diamond cutting blade was 0.7 mm. Scanning of the resulting slices shows the geometry, orientation, and properties of the fractures.

[b] 4 ml of epoxy resin was mixed with 2 ml of hardener and diluted by 0.5 ml of acetone yielding a viscosity of 30 mPa·s (water at 20°C: 1 mPa·s).

No continuous flow path could be detected in the CHEMLAB core (#2) by means of scanning for the fluorescent resin. The structures which can be seen in the scans are attributed to a healed fracture system. Volumes or the fluorescent resin are too small to be found by these techniques. In contrast to this finding, core #1 used at the laboratory showed a well developed fracture. Volumes and the inner surfaces of the fracture could be determined from the scans by means of pixel counting. For this kind of evaluation, the errors in estimating the volume and surface area resulted from rather subtle differences in colors of the resin and granite materials. The threshold of discrimination was found to be a sensitive parameter. Total error of volumes and surfaces was estimated to amount to 10-15%. Additional information on the flow path can be obtained by 3D visualization of the fracture. For visualization the scans of the slices are used and the fracture (core #1) is discriminated by the selection of the color of the fluorescent resin. The slices were oriented numerically and by means of a visualization software, the fracture could be visualized.

Quantification of actinides sorbed onto the inner surfaces

The distribution of actinides and the sorption behavior along the flow path can be studied by different methods. The abraded material gained by cutting the slices was solubilized chemically and the actinide concentration was measured by ICP-MS. Only in a few slices ^{244}Pu could be detected. The Pu concentration was found to be in the range of the detection limit. The actinide concentration on the surface of the slices was analyzed by means of α-counting and by coupled laser ablation ICP-MS techniques. Laser ablation technique data will be presented elsewhere. In addition, preliminary measurements of the actinide concentrations were conducted by micro α-radiography [c]. First results show a great potential of this method. For this reason, this technique will be applied extensively. For core #1, the correlation between the actinide concentration determined on the inner surfaces of the fracture and the geometry of the fracture was investigated. It was assumed that the total amount of actinides were sorbed onto the inner surfaces of the fracture of the core.

Neptunium

The Np distribution shows a continuous decrease of the surface loading from the injection to a depth of 23 mm. Measurement at zero depth (injection plane) was not possible at that moment. At a distance of 4.35 mm (slice thickness of 4 mm and half of the diamond blade thickness of 0.7 mm) from the point of injection, Np surface loading was about 0.1 ng/mm^2. Between 23 mm and 56 mm, Np surface loading was found to scatter between about 0.06 and 0.04 ng/mm^2. Integration of the locally sorbed surface loading of Np between 4.35 and 23.15 mm resulted in a total amount of 117 ng Np equivalent to 0.5×10^{-9} mol. 250 ng were computed between 4.35 and 56.0 mm. This amount was compared to the totally injected ^{237}Np. Nine consecutive actinide migration experiments were performed with core #1. About 50 µl of actinide cocktail were injected during each experiment with a Np concentration of

[c] Alpha radiography was performed by a micro imager M40 (Zinsser Analytic, Frankfurt, Germany) having a spatial resolution of 10-15 µm.

$1x10^{-5}$ mol/l. Arithmetic led to the result that more than one tenth of the totally injected ^{237}Np remained in a depth between 4.35 and 23.15 mm away from the point of injection. More than 20% were found to remain at distance ranging from 4.35 to 56.0 mm. This finding corroborates the findings of batch sorption experiments, where it was shown that Np(V) was reduced and precipitated to Np(IV) in the presence of granite material. It does not contradict the measured recovery data, as recoveries between 10 and 40 % were found.

Americium

A similar analysis can be carried out for ^{243}Am. Am recovery was below the detection limit. This means that almost the total amount of Am injected remained sorbed within the core. In a previous batch sorption study, retardation coefficients R_s were determined. R_s is defined in units of volume per mass (e.g. $ml \cdot g^{-1}$).

$$R_s = \frac{(A_0 - A) \cdot V}{A \cdot m}$$

A_0: radioactivity/concentration in the stock solution (time dependent);
A: measured radioactivity/concentration in the sorption sample
V: volume of solution m: mass of sorption sample

R_s values varied between 70 and 850 ml/g for material of < 1 mm grain size and between 10 and 433 ml/g for larger grain sizes. By assuming a certain specific surface area of the material under investigation, the R_s values can be recomputed to a surface-related quantity (unit: e.g. $ml \cdot mm^{-2}$). Specific surface areas of the material of < 1 mm were measured to be about 1.1 m^2/g using BET N_2 adsorption analysis. However, this value cannot be compared to the geometric surface determined by the scans of the different slices. The surface areas of the fracture represent a gross geometric feature and not the microscopic surface properties determined by BET. For this reason, the mean surface area of the batch sorption material was computed by a simple geometric approach, assuming a mean diameter of 0.7 mm of each grain and a density of 2.6 g/cm^3 of the material. Correlating the surface of the fracture with its volume, a mean surface to volume ratio of 1.7 mm^2/mm^3 was computed. Multiplication of the surface-related Rs value by the mean surface to fracture volume ratio results in values between 34 and 442 for the fine-grained material and between 5.1 and 221 for the gross material. These ratios are dimensionless, representing the retardation of the actinide (Am) versus an inert tracer. The range of retardation coefficients determined by batch experiments can be compared with findings of the migration experiments. The Am peak determined at a distance of 18.45 mm from the point of injection was correlated to the last experiment performed on this core. By application of surface-related retardation coefficients, travel times of the consecutive injected pulses can be computed. In the two last experiments low flow rates (0.001 ml/min) were applied. In the proceeding experiments, flow rates of 0.05 ml/min were applied. Total duration of last experiment was 40000 minutes and with a total eluted volume of 40 ml groundwater and a mean velocity of the groundwater of 0.02 mm/min. As obvious from Fig. 2, migration of Am reached only 18.45 mm within 40000 min. The ratio of the travel times of water to Am gives the retardation of Am and amounts to 43. This value is in the range of the Rs values reported above.

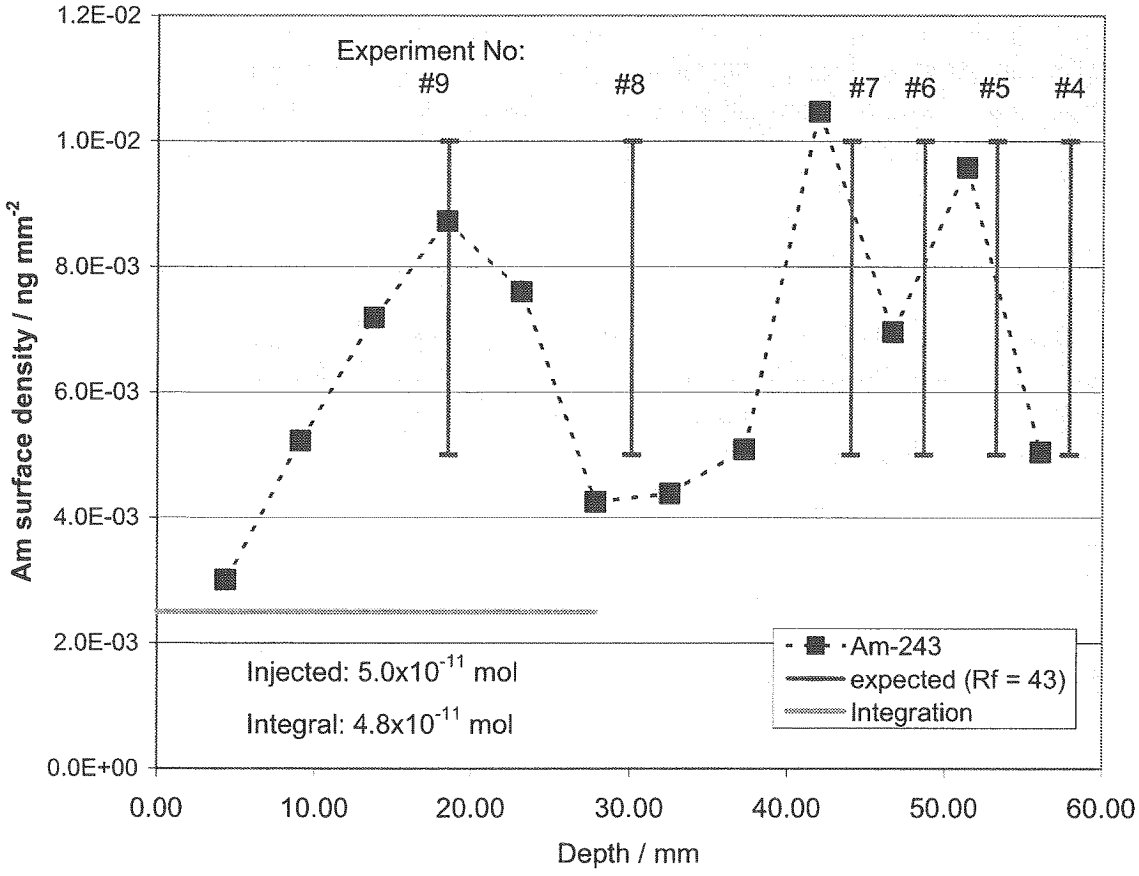

Fig. 2 Assignment of sorbed ^{243}Am distribution in core #1 to consecutive experiments.

Recursively, the expected Am peaks can be computed for the preceding experiments with core #1. The vertical lines shown in Fig. 2 represent the expected maximum concentrations for the previous experiments. These experiments, however, were not performed in a strictly consecutive manner. Moreover, a certain time dependence of sorption was observed for Am. Therefore, the interpretation of the fluctuations of the sorbed ^{243}Am concentration distribution is speculative to some extent.

Discussion and Conclusions

The results obtained for different cores showed individual behavior of these samples. As examples, findings obtained for core #1 and #2 are presented in this paper. Core #1 was used for a total of 9 actinide migration experiments. Breakthrough and recovery of HTO and the actinides were measured in core #2 in a single experiment at Äspö. Breakthrough of Np

followed the tendency of the measured HTO curve. Np which was detected in the effluent migrated with hardly any retardation. Integration of the Np breakthrough results in a recovery which was about 40% of the injected amount. This type of breakthrough cannot be described by a simple sorption model. Precipitation processes have to be taken into account, which were shown in batch sorption experiments. However, the flow path and the corresponding surface characteristics and specific surface sizes are not known. Presently, modeling was performed by means of the one-dimensional TRANS_EQL code (Kienzler, 1995). Flow path analysis by cutting the cores show that an open fracture similar to core #1 did not exist in core #2. Consequently, a simplified porous medium model can be applied to core #2 as a first approach.

The following conclusions can be drawn from the results of the first actinide migration experiments at Äspö HRL:

- The design of the drill cores enclosed in stainless steel autoclaves, tubings, and connectors as well as the sampling procedure fit excellently with the demands for laboratory and in-situ experiments.

- The migration experiments performed at the laboratory and in the CHEMLAB 2 probe complemented each other. The CO_2 partial pressure adjusted in the laboratory resulted in the same actinide speciation as expected under in-situ conditions.

- Determination of hydraulic properties by means of the inert HTO tracer and application of different flow rates is an effective procedure that yields the data required for modeling.

- Destructive and non-destructive analyses of flow paths have to be applied in order to obtain most complete information. In the case of open fractures (core #1), application of fluorescent epoxy resin, cutting, and scanning of slices quantify the volumes and the surfaces of the fractures

- Abraded material gained by cutting the cores can be dissolved. Then, the actinide concentrations can be measured by ICP-MS. Even in the case of injection of pulses of actinides, it was possible to determine the sorbed actinides in the abraded material.

- The cores investigated show different specific patterns of the flow path.

- Experiments resulted in a breakthrough of Np(V) only. In any case, the recovery was $\leq 40\%$. Recovery of Am(III) and Pu(IV) as well as of Np(IV) was not detected.

- Improved analytical methods, such as laser ablation techniques and micro α-radiography have to be applied in order to obtain more complete information about the longitudinal and transversal distribution of sorbed actinides.

- Flow rates used in the experiments were high in comparison to natural groundwater velocity. Therefore, further experiments will be performed at lower flow rates, however, the rates were constrained by the experimental requirements.

Acknowledgement

The present work was performed within the Project Agreement for collaboration on certain experiments related to the disposal of radioactive waste in the Äspö Hard Rock Laboratory (HRL) between the Bundesministerium für Wirtschaft (BMWi) and Swedish Nuclear Fuel and Waste Management Co (SKB). The authors thank the staff of HRL for preparation of rock and water samples, for the excellent cooperation and maintenance of our glovebox.

References

Appelo, C.A.J., Postma, D., 1994. Geochemistry, groundwater and pollution, A.A. Balkema, Rotterdam, ISBN 905410106.

Jansson, Mats, Erikson, Trygve E. 1997. CHEMLAB-In-Situ Diffusion Experiments Using Radioactive Tracers, Migration 97.

Kienzler, B. ,1995. A coupled migration/speciation code - demonstrated by modeling the migration of americium in a column. Proc. of the Internat. Conf. on Mathematics and Computations, Reactor Physics, and Environmental Analyses, Portland, Oreg., April 30 - May 4, 1995, LaGrange Park, Ill.: ANS, 421-30

Untersuchung der Oberfläche von Chlorit mit ADXPS

D. Schild, F. Brandt

Einleitung

Für ein Endlager radioaktiver Abfälle in Hartgestein stellen die Klüfte mögliche Wegsamkeiten für die Migration freigesetzter Radionuklide (RN) dar. RN Migration und chemische Eigenschaften des Grundwassers werden durch die Wechselwirkung mit den Oberflächen der in den Klüften enthaltenen Minerale und Verwitterungsprodukten des Wirtsgesteins bestimmt (Arnold 01, Ticknor 93). Eines der Verwitterungsprodukte des Granits ist Chlorit mit der Summenformel $(Mg,Al,Fe)_{12}(Si,Al)_8O_{20}(OH)_{16}$. Das Schichtsilikat Chlorit besteht aus vier sich wiederholender Schichten: $(Si,Al)_4O_{10}$ (Tetraeder) | $(Mg,Fe)_6(OH)_4$ (Oktaeder) | $(Si,Al)_4O_{10}$ (Tetraeder) | $(Mg,Fe,Al)_6(OH)_{12}$ (Brucit-ähnliche Schicht) mit unterschiedlicher Koordination der Kationen (Abb. 1). Bei Alteration des Chlorits kann Eisen freigesetzt und Ferrihydrit gebildet werden. Einbau von RN in Ferrihydrit kann diese immobilisieren, falls Ferrihydrit auf Gesteinsoberflächen sorbiert ist, oder mobilisieren, falls Ferrihydritkolloide vorliegen. Zusätzlich kann sich die RN-Migration durch die pH-Wert Änderung bei Auflösung des Chlorits ändern. Als Beitrag zur Beschreibung der RN-Migration in Granitklüften werden die Prozesse bei Auflösung des Chlorits mit verschiedenen analytischen Methoden untersucht.

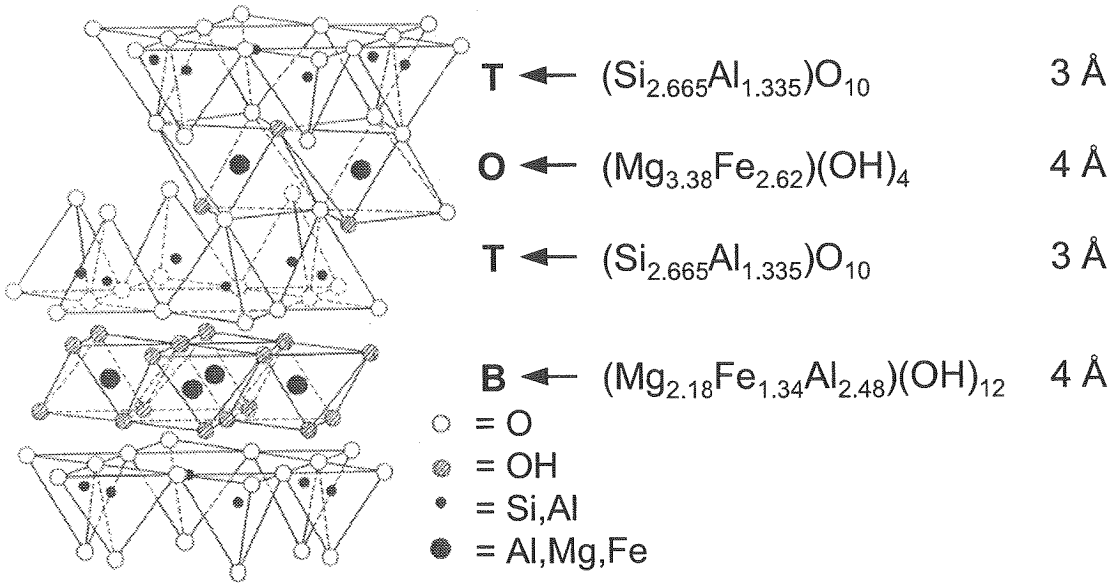

Abb. 1: Die periodische Schichtstruktur von Chlorit mit TOT und Brucit Schicht (B). Schichtdicken und -Zusammensetzungen der untersuchten Probe sind angegeben.

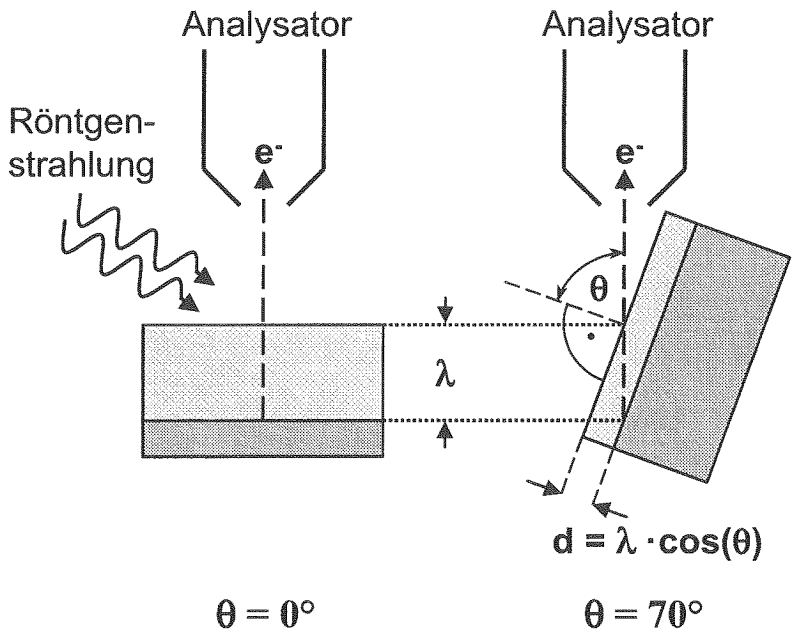

Abb. 2: Prinzip der winkelabhängigen XPS (ADXPS). Durch Kippung der Probe relativ zum Analysator ändert sich die Austrittstiefe d der gemessenen Elektronen.

Winkelabhängige XPS und Modellsystem

Mit winkelabhängiger XPS (ADXPS, Angle-Dependent X-ray Photoelectron Spectroscopy) können Element- und Speziationsprofile der Oberfläche innerhalb der Informationstiefe der XPS (wenige nm) gemessen werden. Durch Variation des Winkels θ zwischen Probennormalen und Analysatorachse werden Photoelektronen mit unterschiedlicher Austrittstiefe detektiert (Abb. 2). Beim Durchgang von Elektronen mit bestimmter Intensität und Energie durch Materie mit der Dicke z kommt es zur Intensitätsabschwächung, die näherungsweise mit dem Gesetz von Lambert-Beer-Bouguer der linearen Absorption beschrieben werden kann: $I = I_0 \cdot \exp(-z / \lambda)$, mit Absorptionskoeffizient $1/\lambda$, Primärintensität I_0 und Intensität I nach Durchlauf der Schichtdicke z. Beim Durchgang von Elektronen unter einem Winkel θ zur Oberflächennormalen durch Materie mit der Dicke z ist

$$I = I_0 \exp\left(\frac{-z}{\lambda \cos\Theta}\right). \qquad (1)$$

Integration liefert für eine Schicht mit Dicke z und relativer Dichte d_i emittierender Atome eine relative Intensität

$$I_z \propto d_i \lambda \cos\Theta \cdot \left[1 - \exp\left(\frac{-z}{\lambda \cos\Theta}\right)\right]. \qquad (2)$$

Aus der Austrittstiefe $d_a := \lambda \cos\theta$ stammt 63 % des gemessenen Photoelektronensignals, aus der Informationstiefe $d_{inf} := 3\ d_a$ entsprechend 95 % des Signals. Für $z \rightarrow \infty$ ist $I \propto d_i \lambda \cos\theta$.

Die Abschwächungslänge λ ist für Elektronen energie- und matrixabhängig und kann aus Dichte und Stöchiometrie mit folgender Beziehung, die auch elastische Streuung berücksichtigt, berechnet werden (Cumpson 97):

$$\lambda = 0{,}316\, a^{3/2} \left\{ \frac{E_{kin}}{Z^{0,45}\left[\ln(E_{kin}/27)+3\right]} + 4 \right\} \quad [nm] \qquad (3)$$

mit $a = 10^7 \left(\frac{A}{\rho\, n\, N_L} \right)^{1/3}$ [nm]

a [nm]: mittlere Atomgröße (Monolagendicke), A [g Mol^{-1}]: mittleres Atomgewicht,

ρ [g cm^{-3}]: Dichte, n: Anzahl der Atome im Molekül, N_L: Avogadro-Konstante

Z: Kernladung, E_{kin}: Kinetische Energie der Photoelektronen einer Elementlinie.

Die so erhaltene Abschwächungslänge λ ist kleiner als die mittlere inelastische freie Weglänge (IMFP) der Elektronen (Seah 79). Für einen homogenen Festkörper mit der Zusammensetzung von Chlorit ergeben sich die in Tab. 1 zusammengestellten Werte für Austrittstiefen bei verschiedenen Winkeln θ und die maximale Austrittstiefe $d_a(\theta = 0°) = \lambda$ der Elektronen von Elementlinien.

Die Modellierung eines Schichtmodells allein aus Messergebnissen durch Entfaltung führt mathematisch zu keiner eindeutigen Lösung (Cumpson 99). Umgekehrt können ADXPS Profile aus Schichtstrukturen berechnet und mit gemessenen Profilen verglichen werden. Bei Chlorit ist z.B. eine Frage, ob die TOT Schicht oder die Brucit Schicht die Oberfläche bildet. Um die Messergebnisse für Chlorit zu interpretieren wurden ADXPS Profile für verschiedene Schichtfolgen an der Oberfläche berechnet. Um die Beiträge zu den Intensitäten der Elementlinien bis zur maximalen Informationstiefe ($\theta = 0°$) zu erfassen, wurden 8 TOTB Schichten entsprechend n = 32 Einzelschichten mit den jeweiligen Elementkonzentrationen berechnet.

Element-linie	**E_{kin} [eV]**	**λ [nm]**	**d_a (40°) [nm]**	**d_a (70°) [nm]**	**d_a (80°) [nm]**
Fe $2p_{3/2}$	776	1,55	1,19	0,53	0,27
O 1s	956	1,83	1,40	0,63	0,32
C 1s	1202	2,20	1,68	0,75	0,38
Si 2p	1385	2,47	1,89	0,84	0,43
Mg 2s	1399	2,49	1,90	0,85	0,43
Al 2p	1413	2,51	1,92	0,86	0,44

Tab. 1: Kinetische Energien E_{kin} der Elektronen von Elementlinien bei Anregung mit Al K_α ($h\nu$ = 1486,6 eV), Austrittstiefen $d_a(\theta)$ bei verschiedenen Winkeln, Abschwächungslängen λ der Elementlinien.

Für die Rechnung wird angenommen, dass sich die Elektronen auf geraden Bahnen bewegen (Straight Line Approximation, SLA), elastische Streuung wird durch die Abschwächungslängen aus Gl. (3) berücksichtigt. Für n homogene Schichten mit verschiedenen d_i, λ_i und Dicken z_i folgt aus Gl. (1) und (2) für die unter dem Winkel θ zur Oberflächennormalen detektierten relativen Intensität I_x der Elektronen einer Elementlinie des Elements x:

$$I_x \propto \sum_{i=1}^{n} d_i \, \lambda_{i,x} \cos\Theta \cdot \left\{ 1 - \exp\left(\frac{-z_i}{\lambda_{i,x} \cos\Theta} \right) \right\} \cdot \prod_{j=1}^{n-1} \exp\left(\frac{-z_j}{\lambda_{j,x} \cos\Theta} \right) \qquad (4)$$

mit Indizes der einzelnen Schichten von der Oberfläche her beginnend. Die relative Atomkonzentration in % für Element x ist

$$c_x = \frac{I_x \, \lambda_x^{-1}}{\sum_m I_m \, \lambda_m^{-1}} \cdot 100 \qquad (5)$$

mit λ_x, λ_m eines homogenen Festkörpers mit der Stöchiometrie von Chlorit.

Experimentelles

Eine Suspension aus natürlichen Chloritpartikeln (< 63 µm) und Isopropanol wurde auf Graphitfolie getropft und getrocknet (Abb. 3) um spektrale Überlagerungen der Elementlinien von Probe und Substrat zu minimieren. Ein Teil der Chloritpartikel liegt wie für ADXPS erforderlich mit der Oberfläche parallel zur Substratoberfläche, von den restlichen Partikeln wird angenommen, dass sie statistisch orientiert sind und einen Beitrag entsprechend dem eines homogenen Festkörper zum Messsignal liefern. ADXPS Messungen erfolgten bei Aus-

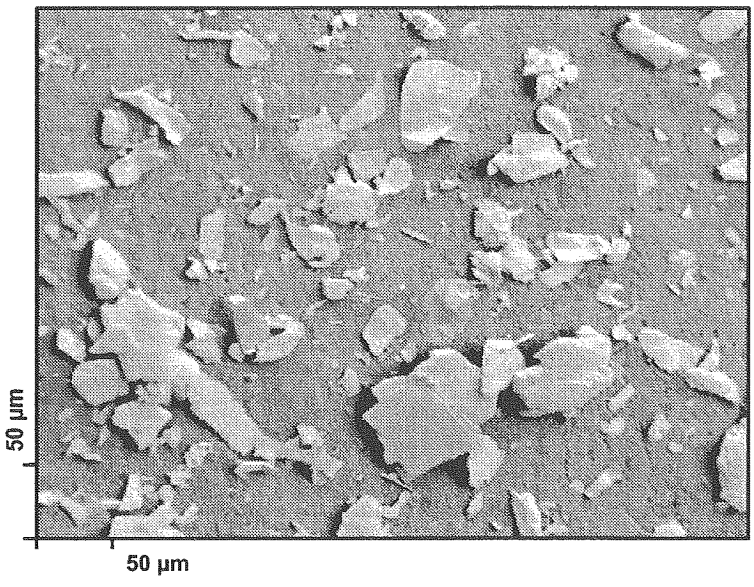

Abb. 3: Präparat der Chloritpartikel mit Isopropanol auf Kohlenstoff aufgetropft.

trittswinkeln (Winkel Oberflächennormale-Analysatorachse) von $\theta = 80°$, 75°, 70°, 60°, 40° und 10°. Für jeden Austrittswinkel werden aus den Intensitäten der Elementlinien relative Atomkonzentrationen berechnet und als ADXPS Profil dargestellt. Der Akzeptanzwinkel des Analysators beträgt $\pm 2°$ und die Analysenfläche 3 x 10 mm^2 bei $\theta = 0°$. Röntgenquelle und Analysatorachse schließen einen Winkel von 54,7° ein, der differentielle Wirkungsquerschnitt der Photoemission bei unpolarisiertem Röntgenlicht ist dann für alle θ unabhängig vom Asymmetrieparameter der Atomorbitale. Messungen der Elementlinienintensitäten erfolgten bei hoher Passenergie der Elektronen im Halbkugelanalysator (187,85 eV). Die Transmission für Elektronen verschiedener Energie (verschiedene Elementlinien) durch die Analysatoroptik ist dann praktisch gleich.

Ergebnisse

Zur Prüfung des Schichtmodells (Gl. 4) wurde das ADXPS Profil für den Fall der homogenen Elementverteilung, entsprechend gleicher Einzelschichten, mit der Stöchiometrie des Chlorits berechnet. Es ergeben sich wie erwartet konstante Atomkonzentrationen (ohne H, in at-%: O (64,3), Mg (9,9), Si (9,5), Al (9,2), Fe (7,1)) entsprechend der vorgegebenen Stöchiometrie für verschiedene Austrittswinkel θ.

Das C 1s Spektrum der Chloritproben wurde nicht ausgewertet, da der Bedeckungsgrad der aufgetropften Chloritpartikel auf dem Kohlenstoffsubstrat nicht überall gleich ist, die Größe der analysierten Fläche sich aber mit dem Winkel θ ändert. Bei berechneten ADXPS Profilen kann eine C_xH_y Kontaminationsschicht auf der Oberfläche des Probenmaterials mit berücksichtigt werden, da diese die Intensitäten der Elementlinien energieabhängig schwächt und die ADXPS Profile ändert.

Mit Gl. (4) wurden für verschiedene Schichtabfolgen auf der Oberfläche des Chlorits ADXPS Profile unter Berücksichtigung einer C_xH_y Kontaminationsschicht berechnet und mit den Messergebnissen verglichen (Abb. 4). Anhand der Verläufe der berechneten Profile können OTB..., TB... und B.... Oberflächen ausgeschlossen werden. Die Messergebnisse entsprechen einer Kombination aus dem berechneten Profil für den homogenen Fall, entsprechend statistisch orientierter Chloritpartikel, und aus dem berechneten Profil für eine TOT... Oberfläche. Das gemessene ADXPS Profil zeigt, dass in den obersten Schichten im Vergleich zu einer ungestörten Schichtung im Mittel die Mg Konzentration die Hälfte, die Al Konzentration ein Drittel und die Fe Konzentration ein Fünftel niedriger sind. Anpassung des berechneten Profils an das gemessene wird durch Variation der Modellschichten erfolgen, um ein genaues Bild der Zusammensetzung der obersten Schichten zu erhalten.

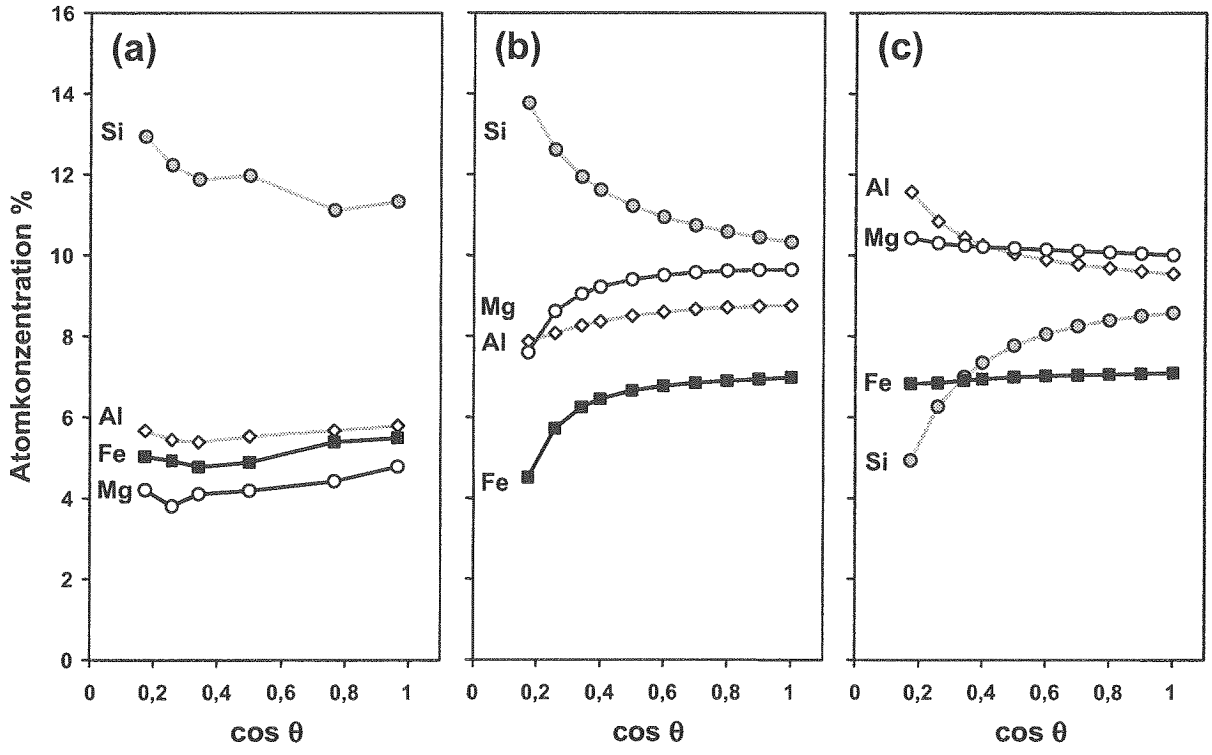

Abb. 4: Gemessenes und berechnete ADXPS Profile: (a) gemessen, (b) TOT Schicht auf der Oberfläche, (c) Brucit Schicht auf der Oberfläche. Berechnung von Profil (b) und (c) ohne zusätzliche Kontaminationsschicht. Gemessen und berechnet wurden die Fe $2p_{3/2}$, O 1s, Si 2p, Mg 2s und Al 2p Linien.

Zusammenfassung und Ausblick

Die untersuchten Chlorit-Partikel sind aufgrund ihrer unregelmäßigen Form nicht ideal für ADXPS Messungen geeignet, dennoch lassen sich ADXPS Profile erhalten. Aus dem Vergleich experimenteller ADXPS Daten mit Rechnungen können Aussagen über die äußeren Schichten des Chlorits oder anderer Schichtsilikate erhalten werden, z.B. über deren Alteration durch Auslaugung bzw. Kationenaustausch in verschiedenen Lösungen.

Referenzen

(Arnold 01) Th. Arnold, T. Zorn, H. Zänker, G. Bernhard, H. Nitsche: Sorption behavior of U(VI) on phyllite: experiments and modeling. J. Contaminant Hydrology **47** (2001) 219-231

(Cumpson 97) P.J. Cumpson, M.P. Seah: Elastic Scattering Corrections in AES and XPS.II.Estimating Attenuation Lengths and Conditions Required for their Valid Use in Overlayer/Substrate Experiments. Surf. Interface Anal. **25** (1997) 430-446

(Cumpson 99) P.J. Cumpson: Angle-resolved XPS depth-profiling strategies. Appl. Surf. Sci. **144-145** (1999) 16-20

(Seah 79) M.P. Seah, W.A. Dench: Quantitative Electron Spectroscopy of Surfaces: A Standard Data Base for Electron Inelastic Mean Free Paths in Solids. Surf. Interface Anal. **1** (1979) 2-11

(Ticknor 93) K.V. Ticknor: Actinide Sorption by Fracture-Infilling Minerals. Radiochim. Acta **60** (1993) 33-42